University of California
Santa Barbara

Development of Microwave Kinetic Inductance Detectors for Applications in Optical to Near-IR Astronomy

A dissertation submitted in partial satisfaction
of the requirements for the degree

Doctor of Philosophy
in
Physics

by

Paul Szypryt

Committee in charge:

Professor Benjamin Mazin, Chair
Professor Lars Bildsten
Professor Dale Andrew Howell

September 2017

The Dissertation of Paul Szypryt is approved.

Professor Lars Bildsten

Professor Dale Andrew Howell

Professor Benjamin Mazin, Committee Chair

August 2017

Development of Microwave Kinetic Inductance Detectors for Applications in Optical to Near-IR Astronomy

by

Paul Szypryt

This thesis is dedicated to my friends, family, and loving girlfriend, Alysha, who have never stopped supporting me throughout my PhD.

Acknowledgements

First of all, I would like to thank my thesis advisor, Ben Mazin, for introducing me to exciting field of low temperature detectors for astronomy. He taught me the laboratory skills necessary for success in the field and helped me to establish interesting research projects that would advance the field. His expertise in optical microwave kinetic inductance detectors has been an invaluable resource and was undoubtedly one of the main reasons the technology has been developed so quickly in the past few years.

Next, I would like to thank the rest of my committee members, Lars Bildsten and Andy Howell. Their teaching and advice over the years have helped me to build a my PhD program. Also, I would like to thank my NASA Space Technology Research Fellowship mentor, Bruce Bumble, at the Jet Propulsion Laboratory. His fabrication experience has helped me to develop my own skills that provided the backbone for some of my later research projects. In addition, I'd like to thank all the members of the Mazin Lab, both current and former, who have put a tremendous amount of their own time into developing this low temperature detector technology.

I would also like to thank all of the friends I have made while in graduate school. Their company has made graduate school much more enjoyable and helped get me through some of the more stressful periods that graduate school entails. Next, I'd like to thank my family who have always encouraged me to continue learning and have shown me unwavering support throughout my life. Last, but certainly not least, I'd like to thank my dearest girlfriend, Alysha, who has always been a source of inspiration and believed in me to follow my dreams.

This work was supported by a NASA Space Technology Research Fellowship. A substantial portion of the device fabrication was done in the UCSB Nanofabrication Facility, a part of the NSF funded National Nanotechnology Infrastructure Network (NNIN). Fab-

rication work was also done at the Microdevices Laboratory (MDL) within NASA's Jet Propulsion Laboratory.

The paper presented in Section 3.5 is adapted with permission from 'P. Szypryt, B.A. Mazin, B. Bumble, H. G. Leduc, and L. Baker. Ultraviolet, Optical, and Near-IR Microwave Kinetic Inductance Detector Materials Developments. *IEEE Transactions on Applied Superconductivity* **25**, pp. 104, 2015'. The paper presented in Section 4.2 is adapted with permission from 'P. Szypryt, B.A. Mazin, G. Ulbricht, B. Bumble, S.R. Meeker, C. Bockstiegel, and A.B. Walter. High Quality Factor Platinum Silicide Microwave Kinetic Inductance Detectors. *Applied Physics Letters* **109**, pp. 151102, 2016'. The paper presented in Section 6.3 is adapted with permission from 'P. Szypryt, G.E. Duggan, B.A. Mazin, S.R. Meeker, M.J. Strader, J.C. van Eyken, D. Marsden, K. O'Brien, A.B. Walter, G. Ulbricht, T.A. Prince, C. Stoughton, and B. Bumble. Direct Detection of SDSS J0926+3624 Orbital Expansion with ARCONS. *Monthly Notices of the Royal Astronomical Society* **439**, pp. 2765-2770, 2014'.

Curriculum Vitæ

Paul Szypryt

Education

2017 (expected)	Ph.D. in Physics, University of California, Santa Barbara.
2014	M.A. in Physics, University of California, Santa Barbara.
2011	B.S. in Applied and Engineering Physics (Magna Cum Laude), Cornell University

Research Experience

June 2012 - Present: Graduate Student Researcher, Mazin Lab, University of California, Santa Barbara, CA

August 2013 - July 2017: NASA Space Technology Research Fellow, Microdevices Laboratory, NASA Jet Propulsion Laboratory, Pasadena, CA

January 2010 - May 2011: Research Assistant, Wilson Synchrotron Laboratory, Cornell University, Ithaca, NY

Teaching Experience

September 2011 - June 2012: Teaching Assistant, Department of Physics, University of California, Santa Barbara, CA

August 2008 - December 2008: Undergraduate Teaching Assistant, Department of Physics, Cornell University, Ithaca, NY

Awards

2013 - 2017: NASA Space Technology Research Fellowship (NSTRF), NASA

2013: Worster Summer Research Fellowship Mentor, UCSB Physics

2013: Physics Circus Award for significant contribution to K-12 outreach program, UCSB Physics

2012: John Cardy Award for strongest academic performance in core first-year graduate courses, UCSB Physics

2007 - 2011: Dean's List, Cornell University

Publications

P. Szypryt, S.R. Meeker, G. Coiffard, N. Fruitwala, B. Bumble, G. Ulbricht, A.B. Walter, M. Daal, C. Bockstiegel, G. Collura, and B.A. Mazin. Large-Format Platinum Silicide Microwave Kinetic Inductance Detectors for Optical to Near-IR Astronomy. In preparation.

P. Szypryt, B.A. Mazin, G. Ulbricht, B. Bumble, S.R. Meeker, C. Bockstiegel, and A.B. Walter. High Quality Factor Platinum Silicide Microwave Kinetic Inductance Detectors. *APL*, 2016.

M.J. Strader, A.M. Archibald, S.R. Meeker, **P. Szypryt**, A.B. Walter, J.C. van Eyken, G. Ulbricht, C. Stoughton, B. Bumble, D.L. Kaplan, and B.A. Mazin. Search for Optical Pulsations in PSR J0337+1715. *MNRAS*, 2016.

S.R. Meeker, B.A. Mazin, R. Jensen-Clem, A.B. Walter, **P. Szypryt**, M.J. Strader, and C. Bockstiegel. Design and Development Status of MKID Integral Field Spectrographs for High Contrast Imaging. *Proc. AO4ELT 4*, 2015.

J.C. van Eyken, M.J. Strader, A.B. Walter, S.R. Meeker, **P. Szypryt**, C. Stoughton, K. O'Brien, D. Marsden, N.K. Rice, Y. Lin, and B.A. Mazin. The ARCONS Pipeline: Data Reduction for MKID Arrays. *ApJ Supplement*, 2015.

G. Ulbricht, B.A. Mazin, **P. Szypryt**, A.B. Walter, C. Bockstiegel, and B. Bumble. Highly multiplexible thermal kinetic inductance detectors for X-ray imaging spectroscopy. *APL*, 2015.

P. Szypryt, B.A. Mazin, B. Bumble, H. G. Leduc, and L. Baker. Ultraviolet, Optical, and Near-IR Microwave Kinetic Inductance Detector Materials Developments. *IEEE Transactions on Applied Superconductivity*, 2015.

P. Szypryt, G.E. Duggan, B.A. Mazin, S.R. Meeker, M.J. Strader, J.C. van Eyken, D. Marsden, K. O'Brien, A.B. Walter, G. Ulbricht, T.A. Prince, C. Stoughton, and B. Bumble. Direct Detection of SDSS J0926+3624 Orbital Expansion with ARCONS. *MNRAS*, 2014.

M.J. Strader, M.D. Johnson, B.A. Mazin, G.V. Spiro Jaeger, C.R. Gwinn, S.R. Meeker, **P. Szypryt**, J.C. van Eyken, D. Marsden, K. O'Brien, A.B. Walter, G. Ulbricht, C. Stoughton, and B. Bumble. Excess Optical Enhancement Observed with ARCONS for Early Crab Giant Pulses. *ApJ Letters*, 2013.

B.A. Mazin, S.R. Meeker, M.J. Strader, B. Bumble, K. O'Brien, **P. Szypryt**, D. Marsden, J.C. van Eyken, G.E. Duggan, G. Ulbricht, C. Stoughton, and M. Johnson. ARCONS: A 2024 Pixel Optical through Near-IR Cryogenic Imaging Spectrophotometer. *PASP*, 2013.

Presentations

P. Szypryt, S.R. Meeker, B. Bumble, G. Coiffard, G. Ulbricht, N. Fruitwala, A.B. Walter, M. Daal, C. Bockstiegel, G. Collura, and B.A. Mazin. The DARKNESS Array: A 10,000 Pixel PtSi MKID Array. *Low Temperature Detectors 17*, Kurume, Fukuoka, JA, 2017.

P. Szypryt, B.A. Mazin, G. Ulbricht, B. Bumble, and C. Bockstiegal. [Poster] Improving Large Format Microwave Kinetic Inductance Detectors through Superconducting Material System Examinations. *Applied Superconductivity Conference*, Denver, CO, 2016.

P. Szypryt, B.A. Mazin, B. Bumble, G. Ulbricht, M. Strader, S.R. Meeker, A.B.Walter, C. Bockstiegel, and G. Collura. A Study of novel superconducting material systems for use in microwave kinetic inductance detectors. *SPIE Astronomical Telescopes + Instrumentation*, Edinburgh, UK, 2016.

P. Szypryt, B.A. Mazin, B. Bumble, G. Ulbricht, M.J. Strader, S.R. Meeker, A.B. Walter, C. Bockstiegal, G. Collura, and N. Fruitwala. UVOIR MKID Design and Material Developments. *5th Workshop on the Physics and Applications of Superconducting Microresonators*, Milan, IT, 2016.

P. Szypryt, B.A. Mazin, B. Bumble, G. Ulbricht, and H.G. Leduc. [Poster] Platinum Silicide MKIDs for UVOIR Astronomy. *Low Temperature Detectors 16*, Grenoble, FR, 2015.

P. Szypryt, B.A. Mazin, and B. Bumble, [Invited] Ultraviolet, Optical, and Near-IR Microwave Kinetic Inductance Detectors, *Applied Superconductivity Conference*, Charlotte, NC, 2014.

P. Szypryt, Status of R&D at UCSB, *Microwave Kinetic Inductance Detectors and Cosmology: Scientific Motivation, Recent Achievements and Planned Experiments*, Fermilab, 2013.

Abstract

Development of Microwave Kinetic Inductance Detectors for Applications in Optical to Near-IR Astronomy

by

Paul Szypryt

Microwave Kinetic Inductance Detectors (MKIDs) are a superconducting detector technology capable of measuring photon arrival times to the microsecond level with moderate energy resolution. MKIDs are essentially superconducting microresonators, and when a photon is incident on the inductor portion of the microresonator, the inductance temporarily increases and the resonant frequency decreases. An array of MKIDs can be naturally multiplexed and read out by assigning each detector a unique resonant frequency during fabrication and coupling the detectors to a single transmission line. A frequency domain multiplexing scheme can then be used to pass a microwave frequency comb through the transmission line to probe the microresonators and listen for photon events. In order to meet the demands of the next generation of astronomical instrumentation, MKIDs need improvements in three main areas: pixel yield, energy resolution, and quantum efficiency. I have investigated new fabrication techniques and materials systems to address these issues. Most notably, I have fabricated MKIDs with platinum silicide as the superconducting layer and have measured especially high resonator internal quality factors ($>10^6$). Platinum silicide films can also be made much more uniformly than the traditional sub-stoichiometric titanium nitride films used in the field, increasing pixel yield. In addition, platinum silicide intrinsically has a higher absorption rate for optical photons than titanium nitride. These platinum silicide detectors are used in two new MKID planet imaging instruments, the Dark-speckle Near-IR Energy-resolved

Superconducting Spectrophotometer (DARKNESS) and the MKID Exoplanet Camera (MEC). Optical MKIDs have already been demonstrated on sky with the first generation MKID instrument, the Array Camera for Optical to Near-IR Spectrophotometry (ARCONS). I have used ARCONS to primarily observe compact objects, such as AM CVn systems and detached white dwarfs. In particular, I used ARCONS to observe orbital expansion in the eclipsing binary system SDSS J0926+3624, with a period rate of change of 9.68 μs/year.

I open my thesis with an general introduction to the field of low temperature detectors and describe the role that MKIDs have within the field. In Chapter 2, I provide a detailed description of the detection principles behind MKIDs and define important superconducting resonator parameters.

In Chapter 3, I move on to describe some of the issues that were limiting the performance of MKIDs. I examine some of the early fabrication techniques and material systems utilized to try to mitigate these issues. In Chapter 4, I describe the platinum silicide material system, which proved to be the most important recent development for advancing the detectors described in this work. The early PtSi work was done using simple one-layer test masks, but the material system was later adapted to the full-multilayer fabrication process. The fabrication of large-format MKID arrays using PtSi for the DARKNESS and MEC arrays is described in detail in Chapter 5.

I conclude my thesis with an overview of some of the astronomical applications of MKIDs. More specifically, I describe my work with compact binary systems that was done with ARCONS. Finally, I explain exciting new MKID applications that are only recently becoming possible as the technology continues to advance.

Contents

Chapter 1

Introduction

1.1 Low Temperature Detectors

Low temperature detectors have recently gained widespread popularity in fields such as astronomy and X-ray beamline science. These technologies exploit a variety of low temperature phenomena to enable highly sensitive photon detection across a broad range of energies. Because these detectors need to be cooled to extremely low, often sub-Kelvin, temperatures for operation, they also have greatly reduced thermal noise. Low temperature detectors can be separated into two main categories: thermal and athermal detectors.

1.1.1 Thermal Detectors

In thermal detectors, a photon strikes an absorbing island, depositing energy onto the island and raising its temperature. By accurately measuring the temperature change associated with the event, one can extract the energy of the incident photon. Typically, thermal detectors are either operated as calorimeters and bolometers. Calorimeters measure the energy of single photons, which is often done for highly energetic photons that

produce large temperature changes, such as X-rays. Bolometers, on the other hand, operate in the low photon energy regime, such as in submillimeter astronomy. Here, incident power is measured instead of single photon energy and the temperature drift is constantly monitored to measure changing power levels. At these wavelengths, single photon detection is usually not feasible due to the low signal response.

There are multiple superconducting detectors that fall under the thermal detector category, but the most prominent is the transition-edge sensor (TES [1]). The basic operation of a TES involves biasing a superconducting film in its superconducting-to-normal transition. In this narrow region, the resistance of the film is highly sensitive to temperature changes caused by photon absorption. By measuring the resistance changes at the transition, a TES can be used as a bolometer to measure power levels from infrared radiation [2] or as a calorimeter to measure single photon energies, as is done in the X-rays regime [3]. Some examples of long wavelength TES projects include the Background Imaging of Cosmic Extragalactic Polarization 2 (BICEP2 [4]), the Submillimetre Common-User Bolometer Array 2 (SCUBA-2 [5]), and the KECK Polarimeter Array [6]. At higher energies, there is the X-ray Integral Field Unit (X-IFU) being designed for Athena [7].

A TES is typically read out by using a Superconducting Quantum Interference Device (SQUID [8]) as a current amplifier, which can easily be impedance-matched to the TES resistance. In cryogenic detectors, thermal loads and limited space are problematic. This makes multiplexing the TESs, or reading out multiple TESs by combining their signals into a smaller number of channels, extremely important. A number of SQUID-based multiplexing techniques exist, such as time-division multiplexing (TDM), code-division multiplexing (CDM), and frequency-division multiplexing (FDM), the main difference between schemes being the basis set used to distinguish the signals coming from different TESs [9]. Of these, TDM is the simplest and most developed of the multiplexing schemes.

Here, rows of SQUIDS coupled to TESs are switched on and sampled sequentially. The various columns of SQUIDS, however, are read out simultaneously. With this method in place, it becomes feasible to create large arrays of TESs, and multiplexing of 256 high energy TESs has been demonstrated [10].

A more exotic thermal low temperature detector is the metallic magnetic calorimeter (MMC [11, 12]). Instead of measuring changes in resistance, as is done with a TES, MMCs use a paramagnetic material. When a photon hits the detector, it raises its temperature, which in turn changes its magnetization. A SQUID is then used to measure magnetic flux changes caused by photon events. The detector is also weakly connected to a heat reservoir and external magnetic field, allowing the detector to thermalize back to its idle state shortly after photon collisions. In terms of readout, a chain of SQUIDs is used in a multiplexing scheme that much resembles the TDM, CDM, and FDM readouts used by the TES community.

1.1.2 Athermal Detectors

The other category of low temperature detectors consists of athermal detectors. Rather than measure temperature changes, these detectors count quasiparticles that are generated by photons incident on a superconductor. In this scenario, a photon breaks a number of Cooper pairs in the superconductor, generating quasiparticles. This is similar to the operation of charged-coupled devices (CCDs), in which a photon strikes the semiconducting detector and promotes an electron to the conduction band. The major difference here, however, is that the superconducting bandgap is approximately 10^4 times smaller than that of the silicon typically used in CCDs, enabling a superconducting detector to measure photons that are about 10^4 times less energetic. When using a superconducting detector to measure photons with energies far above the superconducting

bandgap, a number of quasiparticles proportional to the photon energy are generated. This gives the detector intrinsic energy resolution.

One of the earliest pair-breaking detectors is the superconducting tunnel junction (STJ [13]) This technology is based off of a superconductor-insulator-superconductor (SIS) Josephson junction [14]. For single photon detection, the STJ is typically DC-biased. When a photon strikes the STJ, it breaks up a number of Cooper pairs and generates quasiparticles, which can tunnel through the junction along the direction of the bias voltage. This creates a tunneling current in the junction proportional to the energy of the incident photon. Unfortunately, these detectors often had uniformity issues that came about in the fabrication, causing individual STJs to have varying amounts of Josephson current that needed to be normalized to get an accurate energy measurements across a STJ array. Multiple readout and multiplexing schemes were introduced to address this issue, often involving radio-frequency single-electron transistors (RF-SETs) [15], but these readout systems proved to be difficult to realize.

An emerging detector technology that aimed to resolve some of the issues with the early STJs is the quantum capacitance detector (QCD [16]). The QCD is based off of a quantum circuit called the single Cooper-pair box (SCB [17, 18]). The basic operation of a QCD begins with submillimeter radiation being coupled through an antenna onto a superconducting absorber, breaking a number of Cooper-pairs and generating a population of quasiparticles. The density of quasiparticles within the absorber is measured and read out using a SCB, which includes a superconducting island coupled to the absorber with two Josephson junctions in a SQUID configuration [19]. The island is biased in such a way as to produce a sharp capacitance change when a quasiparticle tunnels from the absorber onto the island. The island is also capacitively coupled to a superconducting resonator, so that when the capacitance of the island changes, the resonator's frequency shifts as well. The resonator is then capacitively coupled to microwave transmission

line, allowing the frequency shifts (or phase shifts) to be measured with digital, room temperature electronics.

1.2 Microwave Kinetic Inductance Detectors (MKIDs)

An entirely different type of pair-breaking detector is the Microwave Kinetic Inductance Detector (MKID [20, 21]). The basic idea of the MKID is that when a photon strikes a superconductor, breaking Cooper pairs and generating quasiparticles, the inductance of the film is temporarily increased due to the reduced charge carrier density [22]. If one patterns the superconductor into an LC resonator, a photon that causes a shift in the film inductance will also lower the resonant frequency of the resonator. By measuring the resonator response, one can extract the energy and arrival time of the incident photon.

The resonator is capacitively coupled to a microwave transmission line and read out using digital microwave electronics [23]. MKIDs are naturally multiplexed by coupling multiple resonators to the same transmission line and varying the geometry of each individual resonator so that it has a unique resonant frequency. The readout passes a comb of probe tones through the transmission line, driving the resonators on resonance, and simultaneously monitors the resonator response for photon events. Thousands of resonators can be multiplexed with a single transmission line with this method in place [24].

In practice, MKID operation is more complex than the simple picture given above. A more detailed description of the theory behind MKIDs and their operation is given in Chapter 2.

1.3 MKID Instruments

MKIDs first started gaining popularity as a potential low temperature detector technology for astronomy in the 2000s. Since then, a number of instruments housing MKID arrays have been developed for both the submillimeter and the optical to near-IR wavelength regimes. In the next few years, there are also plans to build larger and more powerful MKID instruments. A few of the most significant MKID instruments are described below.

1.3.1 Submillimeter MKID Instruments

The first MKID instrument, DemoCam, was commissioned at the 10-meter Caltech Submillimeter Observatory in 2007 [25]. DemoCam was a 16 two-color pixel MKID demonstration camera with 240 and 350 GHZ channels. It contained an early prototype readout system that could only read out 4 of the pixels simultaneously. Although only a demonstration camera, it was able to obtain maps of Jupiter, Saturn, and the interstellar gas cloud G34.3. DemoCam was the predecessor for the more powerful Multicolor Submillimeter Inductance Camera (MUSIC [26]). Music contained 576 spatial pixels, each operating in the 150, 226, 293, and 349 GHz bands. The instrument had a fully working microwave readout system based on the Reconfigurable Open Architecture Computing Hardware (ROACH [27]) architecture developed by Collaboration for Astronomy Signal Processing and Electronics Research (CASPER), which will be discussed more in Chapter 2. Unfortunately, this work was largely put on hold due to the decommissioning CSO telescope.

Submillimeter MKIDs were brought to the IRAM 30-meter telescope through the prototype instrument, the New IRAM KID Array (NIKA [28]). A more permanent MKID camera, NIKA2 [29], was installed in 2015 and is now open to the public as

facility class photometric instrument for the telescope. The NIKA2 camera is made up of 3 separate arrays. The first version installed at IRAM contained a 150 GHz band array with 616 pixels and two 260 GHz band arrays containing 1140 pixels each. This was a substantial upgrade from NIKA1, which only had 132 detectors in the 150 GHz band and 224 detectors in the 260 GHz band. NIKA2 is expected to be a highly productive tool in submillimeter astronomy over the next decade with a wealth of potential applications such as medium to high redshift Sunyaev-Zeldovich (SZ) mapping and galaxy cluster observations.

On the horizon, there are three MKID instruments that will act as on-chip spectrometers. These are named DESHIMA [30], SuperSpec [31], and μ-Spec [32]. All three instruments use MKIDs as the detectors on these chips, but they perform the spectroscopy in two very different ways. DESHIMA and SuperSpec use a filter bank composed of half-wave resonators whereas μ-Spec uses nested transmission lines of various lengths to perform phase delays. Due to their relatively high sensitivities, these sorts of MKID spectrometers may be ideal for the proposed Background-Limited Infrared-Submillimeter Spectrometer (BLISS [33]) aboard the Space Infrared Telescope for Cosmology and Astrophysics (SPICA [34]).

1.3.2 Optical to Near-IR MKID Instruments

Optical to Near-IR MKID instruments were developed years after the first submillimeter instruments. The first optical MKID instrument, the Array Camera for Optical to Near-IR Spectrophotometry (ARCONS [35]), was commissioned at Palomar Observatory in 2011. The ARCONS array was made up of 2024 (44×46) pixels split between two coplanar waveguide (CPW) transmission lines. The pixel pitch was set at 222 μm. A total of 8 ROACH boards were used to read out the entire array. The designed res-

onator spacing was 2 MHz with gaps in frequency space separating out the readout bands of the various ROACH boards. The instrument's wavelength band of observation was 380–1150 nm. An example of an ARCONS array is shown in Figure 1.1.

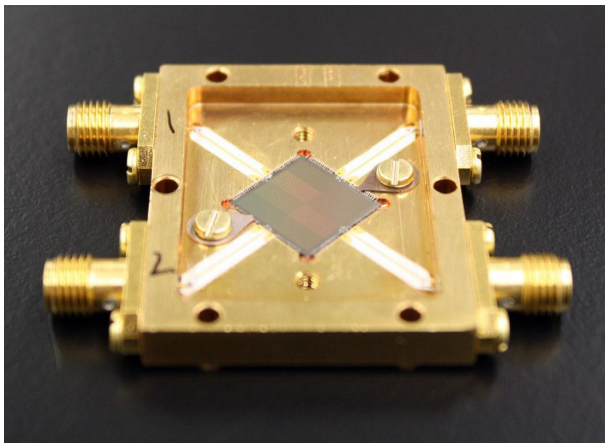

Figure 1.1: An example of a 2,024 pixel ARCONS array. This was a general purpose optical to near-IR MKID instrument commissioned at Palomar Observatory in 2011.

The top performing ARCONS array had superconducting resonators made out of sub-stoichiometric titanium nitride with a superconducting critical temperature, T_C, of $\sim$1 K [36]. Resonators made using this material generally had exceptionally high internal quality factors, often a strong indicator of individual resonator noise performance. On average, ARCONS array resonators had an average energy resolution, $R = E/\Delta E$, of approximately 8 at 400 nm. The detectors had a maximum quantum efficiency of about 17% at the lower wavelength end. The most significant issue with the ARCONS array was non-uniformity in the T_C, causing resonators to shift away from their design frequency and reduce overall pixel yield due to resonator collisions in frequency space. The result of this is that even though the array had >90% yield after fabrication, frequency collisions reduced this yield number to $\sim$70%. Methods for improving the yield issue and other detector performance issues are discussed in Chapters 3 and 4.

ARCONS had multiple successful observing runs at Palomar Observatory and pro-

duced a number of astronomical publications. The main science targets of ARCONS were faint, time-varying objects such as pulsars [37, 38] and compact binaries. As an example, ARCONS was able to measure an increasing orbital period in the ∼30 min eclipsing AM CVn system, SDSS J0926+3624 [39]. Compact binary observations done with ARCONS will be covered in detail in Chapter 6.

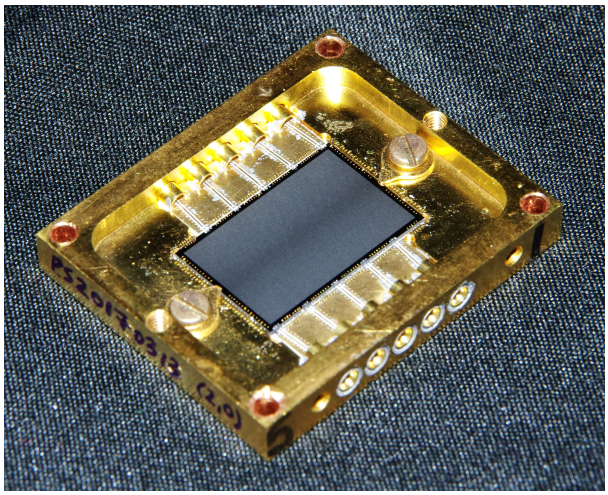

Figure 1.2: A 10,000 pixel PtSi DARKNESS array. This was housed in the first of a series of MKID instruments used for the direct imaging of exoplanets. DARKNESS was originally commissioned at Palomar Observatory in 2016.

The next generation of optical to near-IR MKID instrumentation is focused on an entirely different astronomy goal: the direct imaging of extrasolar planets, or exoplanets. The first of two MKID exoplanet imaging instruments was the Dark-speckle, Near-IR, Energy-resolved, Superconducting Spectrophotometer (DARKNESS [40]). This camera had its first light at Palomar Observatory in 2016. It contained a 10,000 pixel TiN MKID array during its first light observations, but in more recent runs has been upgraded to contain a more uniform platinum silicide array, as will be discussed in Chapter 5. To match specifications of an adaptive optics system, the wavelength band of observation for this camera has been shifted to 700–1400 nm. DARKNESS continues to observe at Palomar Observatory, with the array undergoing numerous improvements between runs,

and astronomy results are expected to be published shortly. One of the more recent PtSi DARKNESS arrays is shown in Figure 1.2.

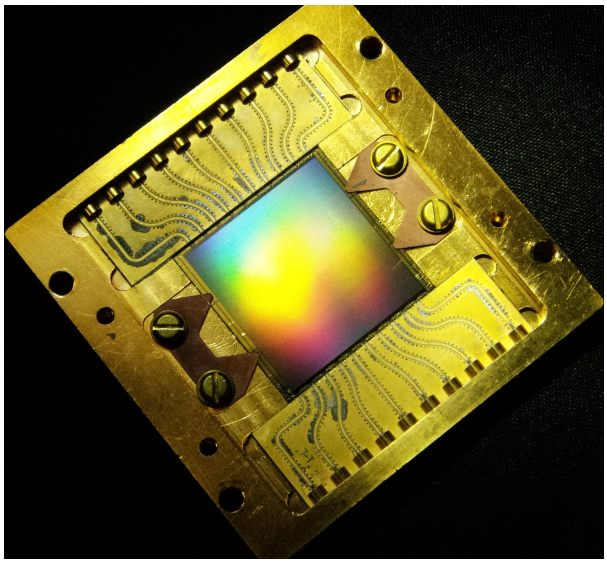

Figure 1.3: A 20,440 pixel MKID array to be used in the MEC instrument. This is a direct exoplanet imaging instrument that will be commissioned at the Subaru Telescope on Mauna Kea in 2017.

The second of these two exoplanet direct imagers is the MKID Exoplanet Camera (MEC). This camera will be commissioned at the Subaru Telescope on Mauna Kea in late 2017. The MEC array is very similar to the one used in DARKNESS, with the largest difference being roughly double the number of detectors (20,440 as opposed to 10,000). In addition, some more minor fabrication changes were made to improve the performance of individual resonators and the microwave transmission as a whole. The MEC array is shown in Figure 1.3.

1.4 Thermal Kinetic Inductance Detectors (TKIDs)

Another detector concept that is a hybrid of a calorimetric thermal detector and a kinetic inductance detector is the so-called thermal kinetic inductance detector (TKID).

Here, instead of photons being directly absorbed by the inductor, an absorber attached to a free-floating membrane is used. The photon deposits energy onto the membrane, heating it up, and the heat is only allowed to leave the membrane through thin channels with a controlled thermal conductance. The inductor portion of a superconducting microresonator sits on these channels, causing Cooper pairs to break in the inductor when heat escapes the absorber. This causes a temporary increase in the sheet inductance of the resonator, much like in MKIDs, and by modeling the pulse shape, the photon energy can be extracted. Theoretically, this sort of design would have a higher maximum energy resolution than the simple MKID design because energy is not lost to phonons diffusing away from the detector; more of the photon energy could be used toward a measurable signal.

Currently, this detector concept is being explored primarily for X-ray detection [41]. X-rays are too energetic to be efficiently absorbed by the superconducting inductor portion of a MKID, which is typically only about 50 nm thick in the standard optical MKID design. This makes a thick absorber a necessary structure in X-ray detectors, which a TKID can more naturally accommodate. In addition, the amount of heat generated in the membrane by a single X-ray is high compared to an optical photon, making the temperature change easier to detect. A scanning electron microscope (SEM) image of a TKID is shown in Figure 1.4. TKIDs for optical photons are certainly not impossible, but a good deal of work would need to be done on carefully engineering the thermal conductance and capacitance of such a detector to be optimized for optical wavelengths.

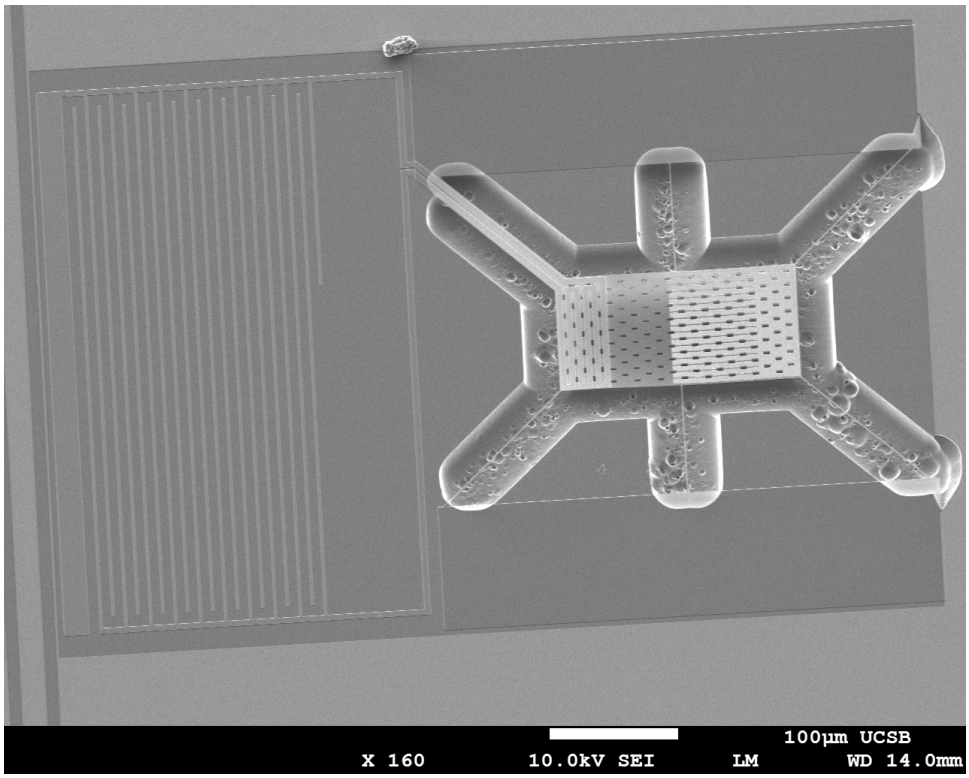

Figure 1.4: A scanning electron microscope (SEM) image of a TKID. The interdigitated capacitor to the left is deposited directly on the Si substrate, whereas the inductor region is sitting on a SiN membrane alongside a thicker absorbing material. The SiN membrane is supported by very thin (on order 1 μm wide and 100 μm long) legs, which control the heat flow off of the membrane.

Chapter 2

MKID Principles of Operation

2.1 Kinetic Inductance

The operational principle behind MKIDs is kinetic inductance. The main idea is charge carriers carry a finite inertia that will act to oppose any changes in electromotive force. The kinetic inductance of a conductor can be derived from the Drude model [42, 43] and is related to the imaginary part of the complex conductivity,

$$\sigma = \frac{\sigma_0}{1+\omega^2\tau^2} - i\omega\tau\frac{\sigma_0}{1+\omega^2\tau^2}, \tag{2.1}$$

where σ_0 is the DC conductivity $ne^2\tau/m$. Here, n is the charge carrier density, e is the electron charge, τ is the collison time, m is the charge carrier mass, and ω is the frequency of the wave in the conductor. From the equation above it can be seen that although the kinetic inductance term is present in normal metals, it is typically small unless the angular frequency of the wave is large. Superconductors, however, are defined by their vanishing resistance, so the collision time $\tau \to \infty$, making the imaginary term in the conductivity much more significant. For a rigorous derivation of the complex

conductivity of a superconductor, the original paper by Mattis and Bardeen is an excellent source [22].

For MKIDs, the quantity of interest is the surface impedance (mostly inductance) in the thin film limit. This is often expressed in terms of the magnetic penetration depth, λ. Following the derivation of Ref. [21], the local penetration depth goes as

$$\lambda_{local} = \sqrt{\frac{\hbar}{\pi \Delta \mu_0 \sigma_n}} \approx 105 \text{ nm } \times \sqrt{\frac{\rho_n}{100\ \mu\Omega \cdot \text{cm}} \frac{1\ K}{T_C}}, \tag{2.2}$$

where Δ is the gap energy, μ_0 is the vacuum permeability, σ_n is the normal state conductivity, ρ_n is the normal state resistivity, and T_C is the superconducting transition temperature. From here, the thin film penetration can be written as

$$\lambda_{thin} = \frac{\lambda_{local}^2}{t}, \tag{2.3}$$

where t is the film thickness, which is valid when $t \ll \lambda_{local}$. The sheet inductance then goes as

$$L_S = \mu_0 \lambda_{thin}. \tag{2.4}$$

Typical inductance values of the materials used in optical MKIDs are in the range of about 5–30 pH/$\square$ and can easily be tuned by varying the film thickness.

Next, it is important to understand how the sheet impedance reacts to photons that are incident on the superconductor. As was mentioned earlier, when a photon with energy $> 2\Delta$ hits a superconductor, it breaks up a number of Cooper pairs and temporarily converts them to quasiparticles. A cartoon schematic of this process is shown in Figure 2.1.A. While the quasiparticles are recombining into Cooper pairs, the sheet impedance will be increased due to the momentary reduction in charge carriers. The quasiparticle recombination time (quasiparticle lifetime) for superconductors used in op-

tical MKIDs is typically $\sim$ 10–100 μs. Following the derivation of Ref. [44], the number of quasiparticles generated is directly proportional to the photon energy and is given by

$$\delta N_{qp} = \eta h\nu/\Delta, \tag{2.5}$$

where η is an efficiency factor of approximately 0.57 [45]. This factor accounts for not all of the photon energy being converting into quasiparticles; some of the energy will instead go into phonons and other sources. When detecting incident photon power rather than energy, as is often necessary in submillimeter astronomy, a similar relation can be written,

$$\delta N_{qp} = \eta P\tau_{qp}/\Delta, \tag{2.6}$$

where P is the absorbed power of the incident light and τ_{qp} is the quasiparticle recombination time. The quasiparticle density can also be calculated this way with some knowledge of the geometry of the absorbing structure.

Although it is useful have an understanding of how the quasiparticle density changes with photon energy, the more directly measurable quantity of interest is the sheet impedance. From Mattis-Bardeen theory [22], the fractional change in the sheet impedance can be related to the change in quasiparticle density by

$$\frac{\delta Z_S}{Z_S} \approx \frac{\delta n_{qp}}{2N_0\Delta}, \tag{2.7}$$

where N_0 is the density of states at the Fermi energy and n_{qp} is the quasiparticle number density. Here, it is important to see that for a given superconductor, the fractional change in sheet impedance is linearly proportional to the energy (or power) of any incident photons. This fractional change in sheet impedance can be precisely measured if the superconductor is patterned into an LC resonator.

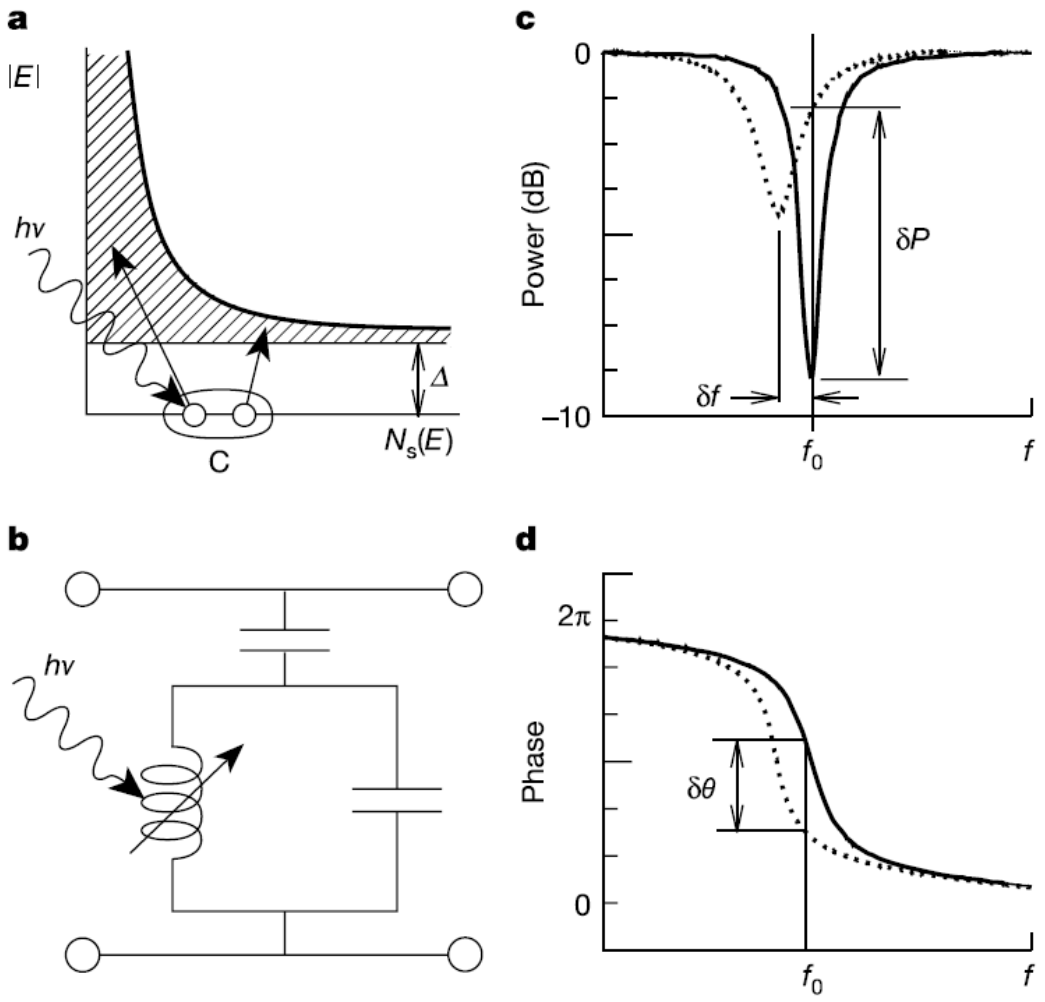

Figure 2.1: A. A photon with energy $h\nu > 2\Delta$ strikes a superconductor, temporarily breaking up a number of Cooper pairs and generating twice that number of quasiparticles. Because this reduces the number of charge carriers (Cooper pairs) within the superconductor, the sheet impedance is also increased. B. The equivalent circuit of a single MKID. Photons incident on the inductor temporarily increase its inductance. C. An increase in inductance leads to a decrease in resonant frequency and amplitude signal. D. This shift can also be viewed as a phase signal, which is often the easier signal to read out with digital room temperature electronics. Reprinted with permission from Day et al. 2003 [20].

2.2 Superconducting Microresonators

MKIDs are essentially superconducting LC resonators that are capacitively (or sometimes inductively) coupled to a microwave transmission line. The equivalent circuit of a MKID is shown in Figure 2.1.B. Notice that in the figure, the inductor is drawn as a variable inductor with a photon of energy $h\nu$ incident on it. This is meant to show that photons absorbed by the superconducting inductor temporarily increase its inductance through the kinetic inductance effect, as described in the previous section. Because the effective inductance of the resonator is now higher, and the frequency goes as $1/\sqrt{LC}$, the resonant frequency of the resonator is decreased. With the addition of thermal quasiparticles, and therefore nonzero dissipation, the amplitude of the resonance is also decreased. This shift in frequency and amplitude is shown in Figure 2.1.C. Because the resonator is coupled to a microwave transmission line, the signals produced from photon hit events can be read out using digital electronics, as will be described in the Section 2.3. For practical purposes, these readout systems measure phase instead of amplitude or frequency, as is shown in Figure 2.1.D.

In order to understand the resonator response to photon events, it is important to have a detailed superconducting resonator model and a straightforward method for extracting resonator parameters from measured data using this model. Luckily, Gao 2008 motivates such a model in his PhD thesis [46]. He provides the following equation for the complex transmission of a superconducting resonator capacitively coupled to a microwave transmission line,

$$S_{21}(f) = ae^{-2\pi i f\tau}\left[1 - \frac{Q/Q_c e^{i\phi_0}}{1 + 2iQ\left(\frac{f-f_0}{f_0}\right)}\right]. \tag{2.8}$$

Here, a is a complex constant that depends on any gain and phase shifts through the transmission line. ϕ_0 is related to the phase angle and f_0 is the resonant frequency of the

resonator. Finally, Q, Q_c, and Q_i are the total resonator, coupling, and internal quality factors, respectively. Due to the number of parameters in this model, it is often difficult to perform a fit directly. Instead, different parts of the model are first fit individually to later provide initial values for the full, multivariate fit. These parameters and experimental methods for extracting them are described in more detail below.

2.2.1 Cable Delay

The first term in the model, the cable delay, is not one that is actually a property of the resonator itself, but rather related to the microwave transmission line. This term accounts for the travel time of the wave through the cable, and will therefore depend on the length of the cable. It will also apply a different phase delay depending on the frequency of the wave through the line. This parameter is quite easily measured with a vector network analyzer (VNA), which typically has a feature built in just for measuring this sort of delay. Typical values for the cable delay seen in the measurement setups in our lab are on order 10 ns.

2.2.2 Resonant Frequency and Phase Angle

The next set of parameters are the resonant frequency and the phase angle. The resonant frequency, in this case, is the central frequency point at which the superconducting microresonator resonates. This can again be measured with a VNA, and is often taken to be the minimum point in the amplitude of the complex transmission, S_{21}. For many applications, however, a more thorough fitting procedure is required. Luckily, this stepped fitting procedure will also be able to provide the phase angle and quality factors.

The fitting procedure is often done in the I-Q, or complex, plane. Here the 'I' represents the 'in-phase' or real component and the 'Q' represents the 'quadrature' or imagi-

nary component. A VNA is again used to sweep the I(f) and Q(f) data points around a resonant frequency of interest. In the I-Q plane, a resonance will appear as an off-center circle as long as the cable delay has been properly removed. This circle's radius and position from the center of the I-Q plane are fitting using a circle fitting algorithm, which is described in considerable detail in Gao 2008 [46]. With the center position fitted, the circle can be translated to the origin of the I-Q plane and rotated to the I axis. From here, the phase angle as a function of frequency can be fit, allowing for a straightforward extraction of f_0 and ϕ_0. Although it may not be apparent now, ϕ_0 will be a useful parameter in the MKID digital readout, which tracks the phase change of a resonator due to the increased impedance from a photon event. An image of a resonator loop in the I-Q plane along with parameters fitted from the loop are shown in Figure 2.2.

2.2.3 Quality Factors

Information about the quality factors of the resonator can also be extracted upon completion of this circle fitting algorithm. The total quality factor, Q, can be extracted directly from the fit alongside f_0 and ϕ_0. The coupling quality factor, Q_c can be calculated from Q through

$$Q_c = \frac{|Z_C| + R}{2R} Q, \tag{2.9}$$

where $|Z_C|$ is the fit center position of the circle and R is its radius. Finally, upon knowing Q and Q_c, the internal quality factor, Q_i can easily be calculated. The inverse of the total quality factor goes as the sum of the inverses of all the composing quality factors,

$$\frac{1}{Q} = \frac{1}{Q_c} + \frac{1}{Q_i}. \tag{2.10}$$

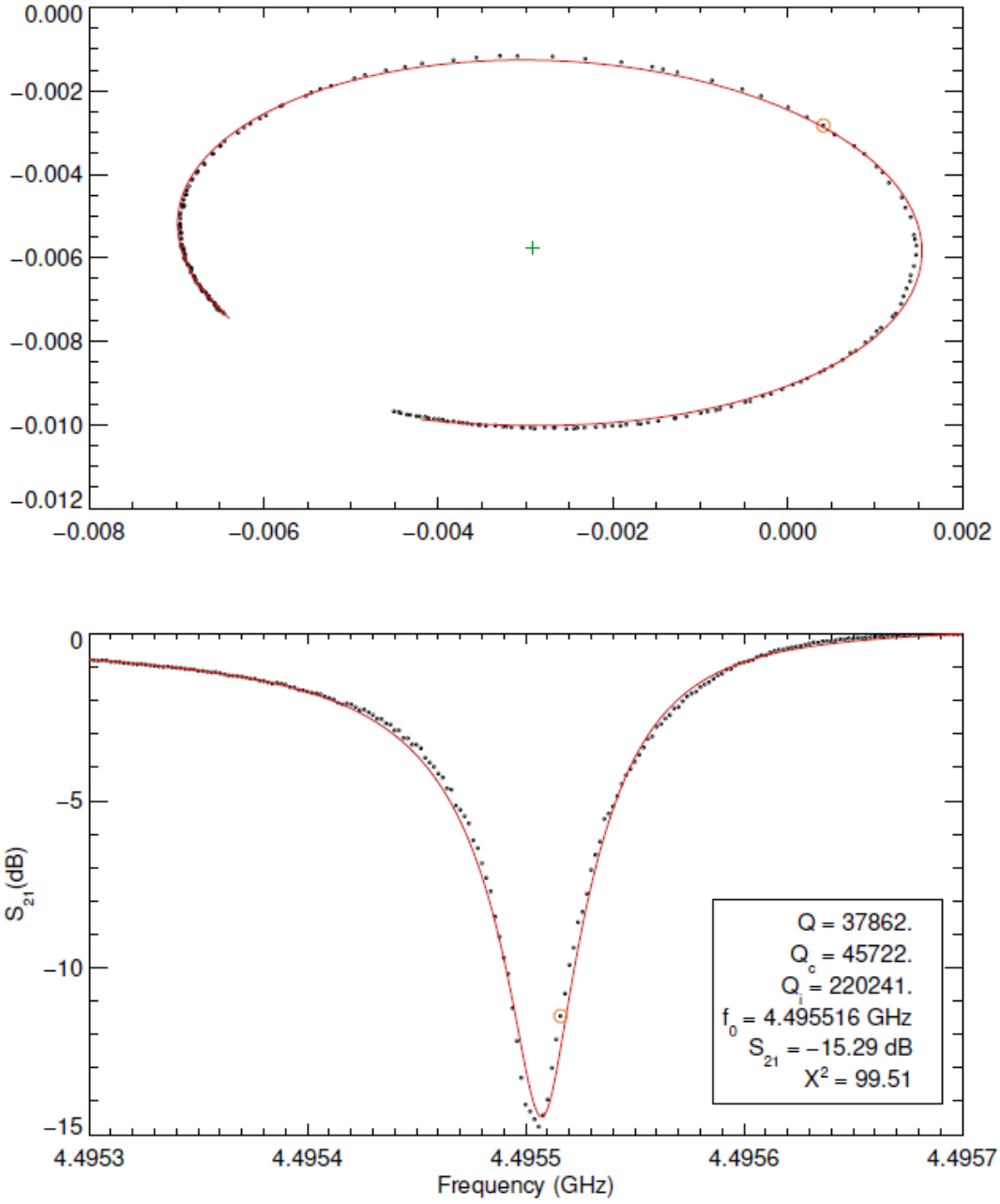

Figure 2.2: (Top) Typical resonator I-Q data being fit with the circle fitting algorithm described in the text. (Bottom) The same I-Q data, but instead plotted as the magnitude of the complex transmission, $|S_{21}|$. This 4.4955 GHz resonator had a Q_c of 46,000 and Q_i of 220,000, resulting in a total Q of about 38,000.

Both individual quality factors, Q_c and Q_i, making up the total quality factor, Q, can now be determined.

Q_c and Q_i are particularly important parameters for microresonator design and performance. Q_c is a measure of the coupling strength between the superconducting resonator and the microwave transmission line. High values of Q_C indicate low levels of power lost from the resonator to the transmission line, so high Q_c actually means low coupling strength. The resonator frequency and Q_c are usually engineered with the help of 2.5D EM field simulation software, such as Sonnet. For optical MKIDs, typical values for the designed Q_c are in the range of 20,000–30,000.

Q_i is an equally important parameter, but unlike Q_c, this parameter cannot simply be designed prior to fabrication. This is a measure of the power losses of the superconducting resonator and can often be used to gauge the quality of the superconducting film. Power can be lost to the substrate, interfaces, dissipative impurities in the superconducting film, and more. Typically, one wants to maximize Q_i in order to push the resonator properties close to those designed with EM simulations. Because high Q_i means low dissipation in the resonator, it is also an indicator of the maximum potential energy resolution one can expect from that resonator. Usually, Q_i values of 100,000 or higher are ideal for getting the energy resolution to a point where other effects become the limiting factors. The Q_i value is often very dependent on careful substrate cleaning techniques and the superconducting material of choice. In TiN on Si [36] and PtSi on sapphire [47] optical MKIDs, for example, Q_i values of over 10^6 have been observed.

2.3 Multiplexing and Digital Readout

Due to MKIDs being LC resonators, they can be naturally multiplexed by using a frequency domain multiplexing (FDM) scheme [23]. To do this, multiple resonators

are coupled to the same microwave transmission line. Each resonator on the line is designed to resonate at a unique frequency. In large arrays, resonators are typically spaced roughly 2 MHz apart with a total microwave line bandwidth of about 3 or 4 GHz. Large interdigitated capacitors (IDCs) are used in the current MKID design, and the frequencies of the resonators are stepped by varying the length of the capacitor legs in a controlled way, thereby changing the capacitance and frequency. A segment of the array which displays this multiplexing strategy is shown in Figure 2.3. With this scheme in place, up to 2,000 optical MKIDs can be read out using a single transmission line [24].

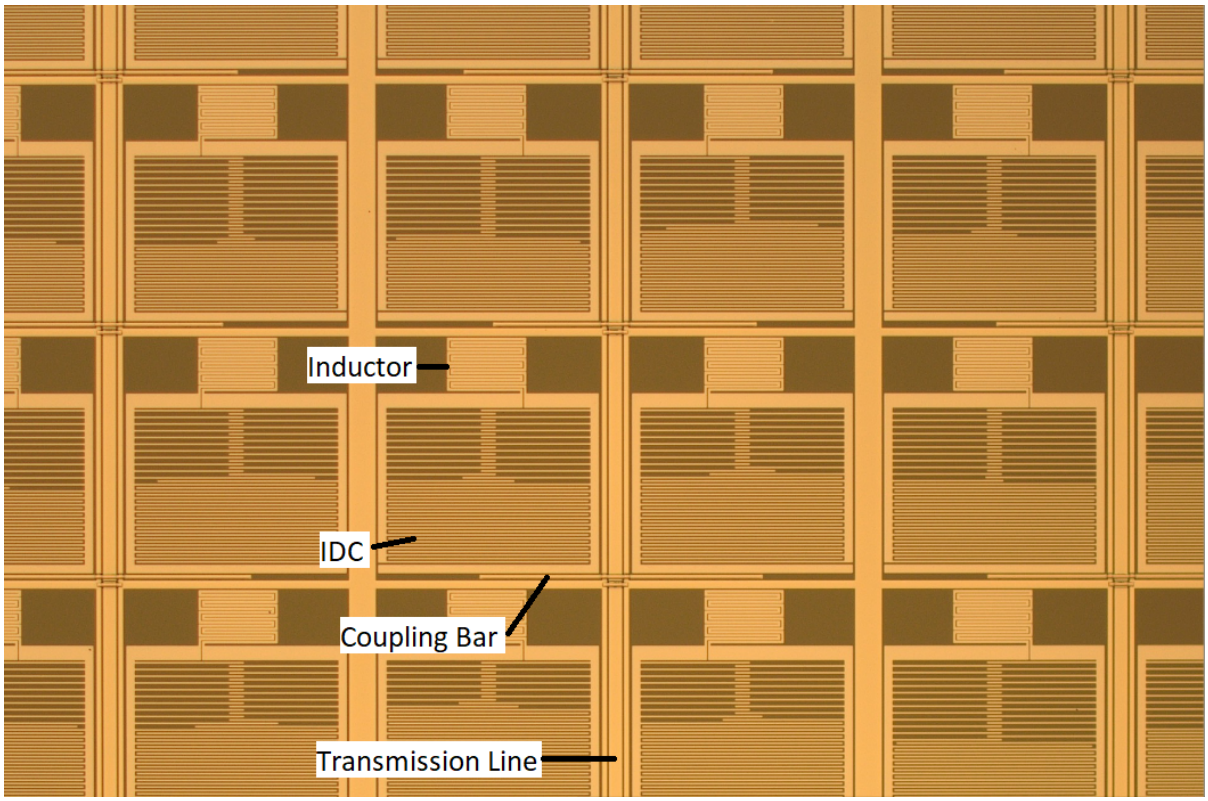

Figure 2.3: Portion of an optical MKID array with a winding transmission line and coupling capacitors going to each individual resonator. Each resonator is given a unique frequency in the readout by varying the lengths of the capacitor legs in the IDC. Note that in the figure above, no two IDCs are exactly the same. The inductor size, however, is kept constant so that the fractional change in inductance for a given incident photon energy is constant across the array.

In terms of reading out photon events in real time, it is often easier for the digital electronics to measure the phase response rather than to track the frequency response. The amplitude response may also be used, but this method typically results in a much lower signal-to-noise ratio (SNR) as compared with the phase response. To measure the phase response of multiple resonators, the digital readout sends a comb of probe tones through the device at all resonant frequencies, driving the resonators. When a photon hits a resonator, the phase at the resonant frequency of that resonator will shift, and the digital electronics will measure this phase shift at the other end of the transmission line.

The actual digital electronics hardware is complex, but the PhD thesis of Matthew Strader is an excellent source of a detailed description for the interested reader [24]. Here, I will provide a basic overview of the required electronics. The readout can be divided into three main components. First, there is the ROACH (or more recently ROACH2) board. The heart of these boards is a field-programmable gate array (FPGA), capable of performing the real-time and multi-channel fast operations necessary for processing phase signal data from an array of detectors. Next, there is the analog-to-digital (ADC)/digital-to-analog (DAC) board. The ADC/DAC board is used to convert between the analog data used in the MKID array and the digital data used in the FPGA. In the newest iteration of the readout system, an additional FPGA was also added to the design to route the high speed signals between ADC/DAC board and the ROACH2 board. Finally, there is the intermediate frequency (IF) board, which is used to convert between the lower $<$1 GHz frequencies used inside the FPGA and the 4–8 GHZ frequencies of the MKIDs. Each of these digital electronics systems can at present read out roughly 1000 resonators. To read out large arrays of 10 kilopixels or more, multiple copies of hte digital electronics setup are required.

Chapter 3

Detector Improvements

3.1 Background

Optical to near-IR MKIDs had a strong initial performance with the ARCONS project, but the detectors required improvements in a few key areas, namely pixel yield, energy resolution, and quantum efficiency. Although ARCONS was designed with a total of 2,024 pixels, inhomogeneities in the superconducting resonator layer reduced the overall pixel yield to ∼70%. In terms of energy resolution, typical ARCONS pixels had $R = E/\Delta E \approx 8$ at 405 nm. The quantum efficiency was a maximum of 17% in the instrument's 380–1150 nm wavelength band [35].

The next generation of MKID planet finding instruments, DARKNESS and MEC, required improved performance in each of the three areas listed above. For optimal performance, these instruments would require pixel yields of ∼90%, energy resolution of ∼20, and quantum efficiency above 20% [40]. To achieve these improvements, new fabrication techniques and superconducting material systems were investigated. In this chapter, I provide more details on these MKID performance limitations and outline some of the initial work towards making improvements in these areas. Other parameters such

as detector sensitivity, dynamic range, and count rate are also important for MKID array performance and will be discussed, but generally these are not limiting factors.

3.2 Important Parameters and Limitations

3.2.1 Pixel Yield

The most important parameter currently limiting optical to near-IR MKID array performance is pixel yield. This is affected by a combination of factors. First of all, the MKID digital readout electronics are limited in bandwidth. For example, the original ROACH1 readout used with ARCONS operated in a 3–6 GHz whereas the ROACH2 system used with DARKNESS and MEC operated between 4–8 GHz, resulting in a bandwidths of 3 and 4 GHz, respectively. In order to maximize the number of pixels that could be multiplexed on a single transmission line, the spacing between resonators was designed at 2 MHz. Slight imperfections in fabrication could shift resonators away from their designed frequency values, and if multiple resonators overlap in frequency space, they are indistinguishable by the readout. Typically, these pixels become unusable when the frequency spacing between them is less than ∼500 kHz. Errors on order one part in a thousand in $\Delta f/f$ are sufficient for this to occur, making fabrication homogeneity crucial for maximizing pixel yield. An image of a typical frequency span is shown in Figure 3.1.

It should be noted that increasing the resonator spacing would be a method for increasing the percent pixel yield, but in order to do this while keeping the same number of total pixels would require additional transmission lines. This is not usually feasible as additional cryogenic lines add to the thermal constraints of the instrument as well as drive up the costs due to the necessity for additional cryogenic amplifiers and room-temperature readout electronics.

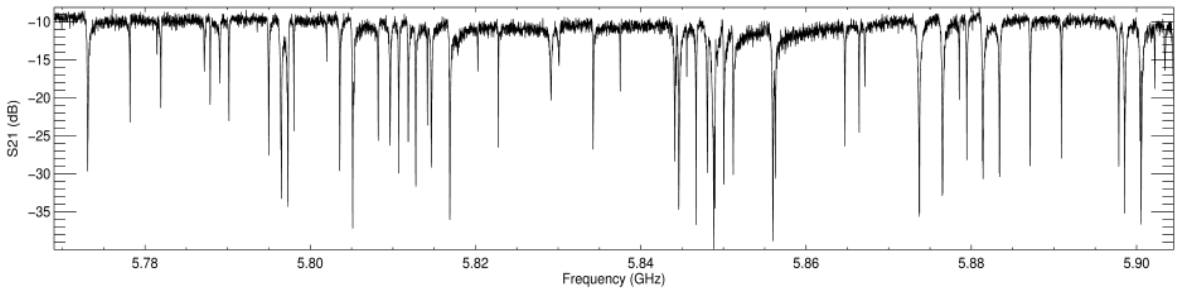

Figure 3.1: A typical frequency span seen in a titanium nitride MKID array. Instead of a uniform 2 MHz spacing, note the significant bunching in multiple areas of this frequency span. When the spacing between two resonators becomes too small ($< 500\ kHz$), these resonators become indistinguishable by the readout, rendering the pixels dead.

With the designed resonator spacing set by hardware and cost limitations, the most promising way to increase pixel yield is to reduce inhomogeneities in the superconducting resonator layer. These non-uniformities were especially noticeable in the sputtered sub-stoichiometric TiN [36] that was used for each of the ARCONS arrays [48] and some of the first DARKNESS arrays [40]. These TiN films were deposited onto silicon wafers by sputtering off of a Ti target while being held in a N_2-rich environment. Stoichiometric TiN films are fairly straightforward to make and have a T_C of around 4 K, but sub-stoichiometric films require a more careful tuning of the N_2 gas flow parameters to get to the desired TiN composition and T_C. Because N_2 deficient films have a lower T_C (down to 400 mK for completely N_2 deficient TiN, i.e. Ti), one can control the gas flow rate to set the film's T_C. In sputtering, argon ions are also typically used to facilitate the sputtering plasma. During the deposition process, the gas pressure in the chamber is usually held at around 5–10 mTorr. The main chamber is kept under ultra-high vacuum (UHV) prior to deposition, with a base pressure on order 10^{-10} Torr, eliminating the likelihood of significant impurities in the sputtered films.

The difficulty with sub-stoichiometric TiN films is controlling the T_C to the same

value across an entire 4" Si wafer. As can be seen from Equation 2.2, altering the T_C in part of the film will change the local penetration depth and therefore L_S in that area, shifting the frequencies of resonators away from their designed values. For applications in optical MKIDs, a T_C of $\sim$1 K is desired when using cryogenic refrigerators with operating temperatures of 100 mK. Unfortunately, the T_C of TiN is extremely sensitive to variations of the N_2 gas flow rate when aiming for a composition with a T_C of $\sim$1 K, as shown in Figure 3.2. This makes variations in frequency even more profound for 1 K T_C TiN, further reducing pixel yield when operating in this regime.

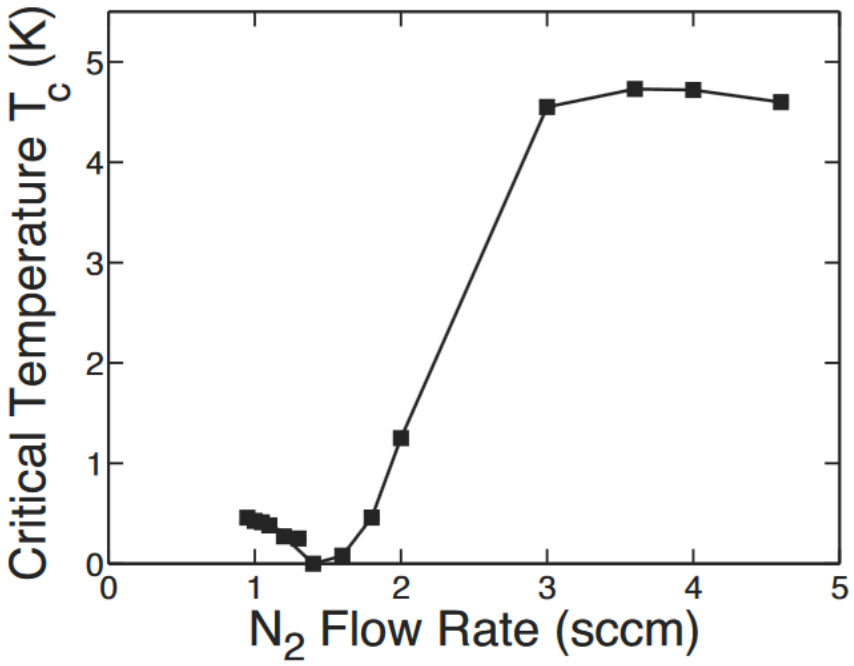

Figure 3.2: T_C versus N_2 flow rate for sputtered TiN films. Notice the small amount of variability for stoichiometric films ($>$ 3 sccm N_2) and the much steeper decline in T_C for sub-stoichiometric films ($<$ 3 sccm N_2). Reprinted with permission from Leduc et al. 2010 [36].

Because TiN has many desirable microresonator properties, it was worthwhile to seek out methods for improving the uniformity of TiN films. The simplest strategy was to increase the size of the Ti sputter target, providing a more uniform beam of Ti atoms

going toward the wafer. In terms of the N_2 uniformity, the gas flow distribution could also be adjusted. Instead of using a single gas port for the N_2, a ring injection system was used. In addition, the wafer would be rotated throughout the deposition, further increasing the spatial uniformity of the TiN film. Finally, more advanced systems contained a second planetary rotation stage. Although these methods did indeed raise the uniformity of the sub-stoichiometric TiN films, it was not enough to overcome the steep gradient in T_C near 1 K.

Other methods for improving TiN uniformity used more drastic changes to the deposition process. For example, one of these methods involved sputtering a layer of stoichiometric TiN, followed by a layer of Ti, and then a second stoichiometric TiN layer [49]. Through the proximity effect [50], this entire film stack will be superconducting with a shared T_C dependent on the ratio of the TiN and Ti film thicknesses. With this method, one can control the T_C of the film fairly well as stoichiometric TiN and Ti films are intrinsically more uniform than sputtered sub-stoichiometric TiN films. Although this method has seen quite good success for submillimeter MKIDs, the quality factor of these films is significantly reduced when the T_C is brought below about 1.5 K, as is the case in optical MKIDs. In addition, the Ti sandwiched between the TiN layers is quite reactive to wet chemistries such as HF, creating new fabrication challenges. Another method for improving the resonator spacing in TiN films is attempting an ex-post facto correction of the resonators. In Section 3.3.1, I will discuss how a focused ion beam (FIB) can be used to make these corrections. Finally, deposition methods other than sputtering may be used to provide more uniform sub-stoichiometric TiN films. In Section 3.3.2 I will explain the atomic layer deposition (ALD) method and in Section 3.5.2 I will describe work done in using this method for TiN films.

Ultimately, these methods for improving sub-stoichiometric TiN uniformity did not do enough to meaningfully increase resonator yield. Instead, entirely new MKID material

systems were developed in hopes that they could retain the desirable properties of TiN while being more uniform across a wafer. The early attempts at developing these new material systems are discussed later in this chapter, but it wasn't until we developed the platinum silicide on sapphire system that we started to see much improved uniformity as well as better per-pixel performance as compared to TiN. The PtSi on sapphire material system will be discussed in in detail in Section 4.2.

3.2.2 Energy Resolution

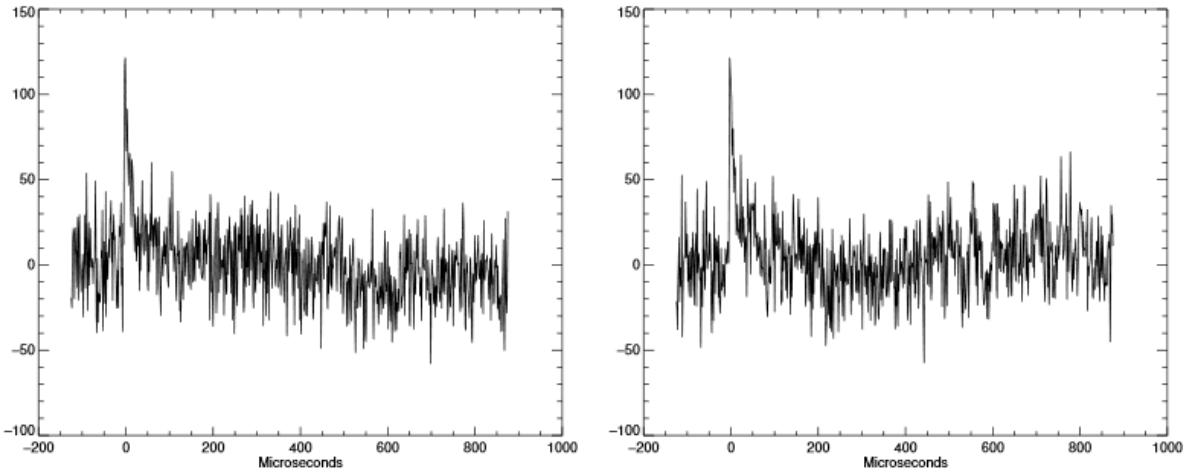

Figure 3.3: A couple of photon events detected by PtSi resonators used in an early version of the DARKNESS array. The array was illuminated with 980 nm light in the lab for testing, resulting in $\sim 110^{\circ}$ phase shift. This early DARKNESS resonator had relatively low Q_i of around 60,000, resulting in a higher noise level as compared to more recent devices.

To understand how energy resolution is calculated in single photon counting MKIDs, one must first know how the energy of a photon is determined. Some examples of what this phase response actually looks like with a PtSi resonator detecting 980 nm photons is shown in Figure 3.3. When a photon is absorbed by the MKID inductor, the rise time in the phase is almost instantaneous (~ 1 μs). Afterward, the photon decays exponentially

to the noise floor with a time constant related to the recombination time of quasiparticles in the superconductor. This time constant is often referred to as the quasiparticle lifetime and its value differs significantly for different superconductors, although there is no clear model for predicting it. Generally speaking, superconductors with higher normal state resistivities tend to have shorter quasiparticle lifetimes.

The energy of the incident photon is proportional to the phase pulse height. Due to the finite sampling rate of the readout ($\sim$1 MHz) and noise in the phase signal, the most accurate determination of the energy will not come from just taking the maximum phase value during a pulse. Instead, the pulse is fit to a model that includes a sharp rise and an exponential decay. The expected maximum phase is extracted from this fit. Generally, longer exponential decays generate better fits when the data is noisy, so superconducting resonators with longer quasiparticle lifetimes will have higher potential resolving power. In order to convert between phase and photon energy, a set of lasers of precisely known wavelength is focused onto the array and the phase response of the resonators is monitored. In standard observation of unknown photon energies, an interpolation between the phase responses to the laser wavelengths is used to determine the energies associated with the measured phases. The MKID data reduction pipeline paper by van Eyken et al. 2015 describes this wavelength calibration system in more detail [51].

For laboratory testing, this method of fitting phase pulses to extract out the photon energy works well. When reading out a large array in real time with the current version of digital electronics, however, there is far too much data to be able to perform a fit of every incident photon. Instead, prior to the regular operation of the array, each resonator takes data from photons of known energy. The pulses from these data are averaged together, and a template is created for that resonator, as shown in Figure 3.4. When using the digital readout with a full array simultaneously, each resonator's template is continuously being cross-correlated with the phase data time stream. When a signal

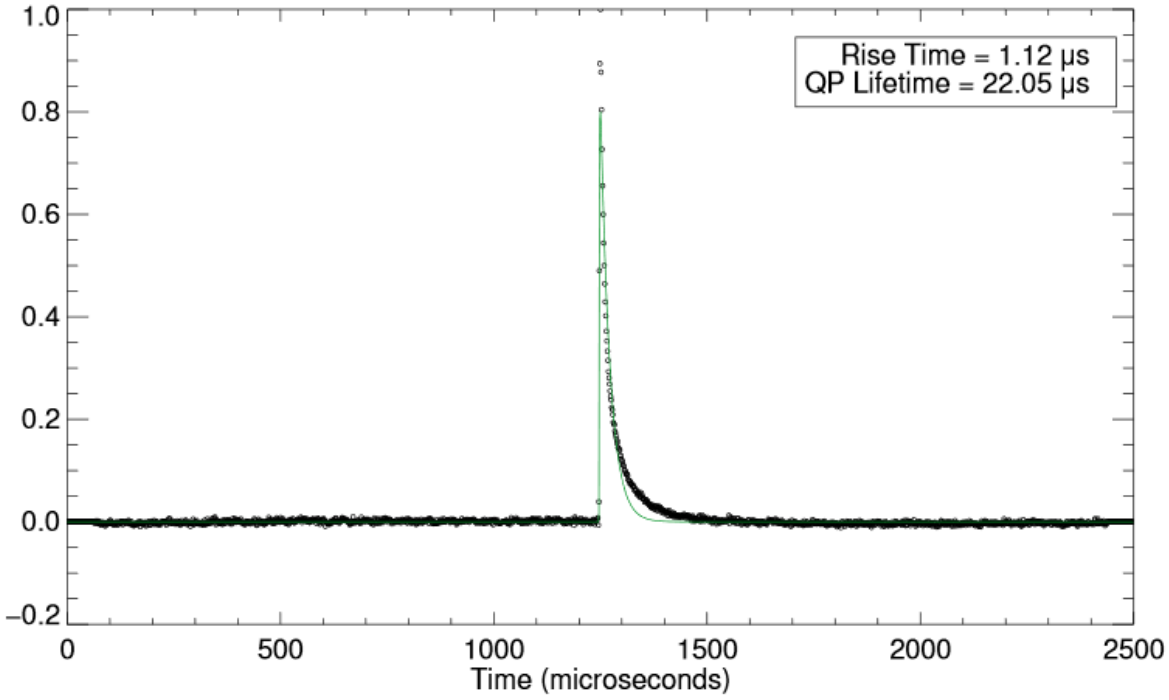

Figure 3.4: (Black) A number of photon events on a single PtSi resonator averaged together and normalized. (Green) A template that has been created from this averaged pulse data and can be used to read out pulse height data in real time via the optimal filtering formalism.

that closely matches the shape of the template is found, only the time stamp and phase height of the event are saved, making the data rate much more manageable. This method closely follows the matched or optimal filtering formalism and has been fairly standard for reading out cryogenic detectors [52].

The wavelength calibration system mentioned above can also be used to estimate the energy resolution, $R = E/\Delta E$, of the array. To do this, photon data of a known wavelength is collected at the MKID and the pulse heights or calibrated energy measurements are aggregated into a histogram, as shown in Figure 3.5. From here, the histogram is fit to a Gaussian distribution and assuming proper normalization, the full width at half maximum (FWHM) is taken to be ΔE. This assumes that the natural FWHM of the

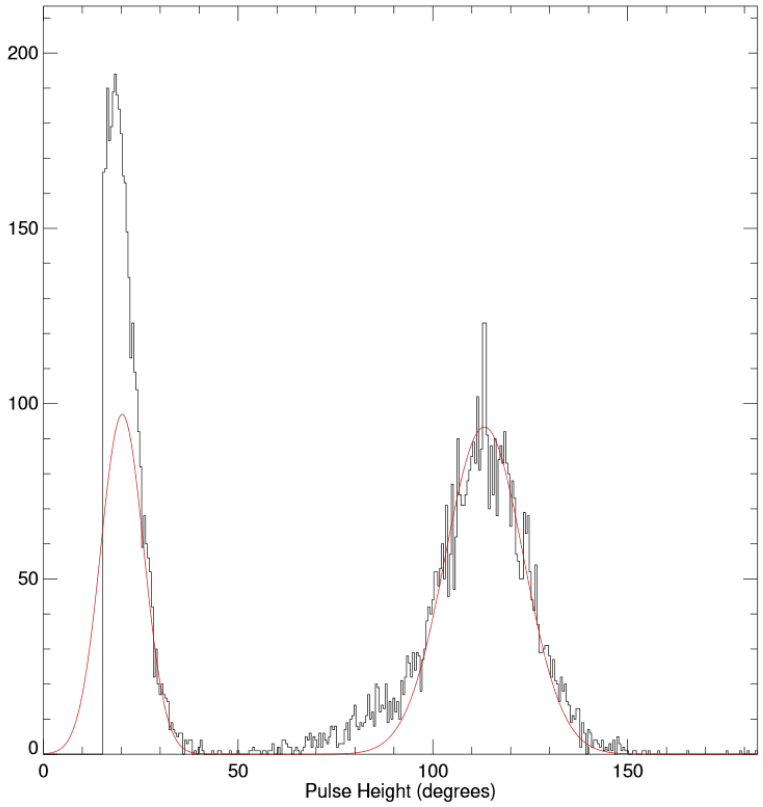

Figure 3.5: A histogram of phase pulse heights measured by a MKID absorbing photons from a 980 nm calibration laser. This particular resonator had lower than average internal quality factor, which limited the energy resolution to around 5 at 980 nm. Here, 980 nm photons show up as 110° phase pulse heights. Also pictured is a tail at low energy which can be attributed to excess thermal radiation and false pulse triggers.

laser line is very small compared to the FWHM detected by the resonator which is very much the case for the moderate energy resolution values ($R \sim 8$) currently observed in optical MKIDs.

There are a number of factors limiting the energy resolution of MKIDs. First, it is important to look at the Q_i of the resonator, which is a measure of the dissipation and random fluctuations in the resonator. When Q_i is low and the EM field fluctuations are high, excess phase noise will drive down the energy resolution of the detector. Generally,

optical MKID energy resolution saturates at $R \sim$8–10 at 1 μm when the Q_i is above about 100,000.

When $Q_i \gtrsim 100,000$ a combination of two-level system (TLS) noise, amplifier noise, and positional dependence of photon hits on the inductor begin to limit the energy resolution. In the TLS model [53], TLSs are free to move between two energy states, causing fluctuations in the field strength of the microwave resonator (mostly near the capacitor) and increasing the phase noise. TLSs are generally believed to exist in the interface between the superconducting layer and the substrate. Advanced substrate cleaning techniques prior to superconductor deposition may lead to reduced TLS density, among other resonator improvements [54].

Currently, the phase noise in MKIDs is at about the same level as the amplifier noise, so in order to get any meaningful improvements in energy resolution, both noise sources must be pushed down. Amplification must be performed close to the detector to maximize the SNR, so cryogenic amplifiers are utilized. The current standard cryogenic amplifiers are high-electron-mobility transistor (HEMT) amplifiers. In the 4–8 GHz regime, these HEMT amplifiers can achieve over 30 dB of gain with a noise temperature of about 2 K [55]. A new type of cryogenic amplifier referred to as a parametric amplifier, or paramp, is being developed [56]. This type of amplifier exploits the nonlinearity in kinetic inductance of a specially designed superconducting transmission line to achieve quantum-limited noise temperatures while maintaining high gain and dynamic range. Paramps are still in early development, but MKIDs could see a dramatic improvement in energy resolution when these devices come to maturity.

Another effect that degrades energy resolution is a positional dependence of photon hits on the MKID inductor. The idea here is that the inductor does not necessarily have a spatially uniform current distribution, and a photon of a given energy that hits one part of the inductor will not produce the same number of quasiparticles as a photon of

the same energy that hits a different part of the inductor. The resulting phase response will depend on the position on the inductor where the photon was absorbed. To reduce degradation of energy resolution from this effect, an inductor geometry with a more uniform current distribution would be required.

3.2.3 Quantum Efficiency

The next important detector parameter is quantum efficiency. This is simply the fraction of light at a given wavelength that makes it through the optical system and is measured by the detector. For ARCONS, the instrument reached a peak system quantum efficiency of about 17% at the lower wavelength end of its operating window. This includes losses due to any filters or windows that the optical beam must pass through before reaching the focal plane array. On top of this, when the instrument is behind an optical telescope, there are often three or more mirrors with imperfect reflectivity between the instrument, further reducing the fraction of light arriving at the detector. Many of these losses cannot be easily reclaimed, so it is extremely important for the detector array to absorb and measure any light that makes its way through the optics. Doing so will often reduce the amount of observation time needed to get up to a desired SNR on an astronomical object of interest.

One method for increasing the quantum efficiency of MKID arrays is adding a microlens array lid directly over the box housing the MKID array. The purpose of the microlens array is to focus light directly onto the photosensitive inductor portion of each resonator, thereby increasing the fill factor to over 90%. These microlens arrays are now commercial products and can be custom designed for the pixel pitch of the detector array. The biggest challenge of using these microlens is properly aligning them so that the optical beams are properly focused to the center of the inductors.

Even when the majority of the light arriving at the detector is focused on the inductors, only a small fraction of that light will actually be absorbed. Although the superconductor is typically thick enough to not pass any light through, there is still a considerable amount of light reflected from its surface. This is more intrinsically a material property, with different materials absorbing more or less light at certain wavelengths than others. As an example, a comparison of the transmission, reflectance, and absorption spectra of TiN and PtSi is shown later in Figure 4.3. To increase this absorption fraction, an anti-reflection coating could be added to the inductor. Another solution would be to switch over to a TKID design, as discussed in Section 1.4, which separates the absorbing structure from the measurement MKID. Work on TKIDs, especially in the optical regime, is still in very early development.

3.2.4 Detector Sensitivity and Dynamic Range

Another detector issues that deserves some discussion is sensitivity, or the measured phase response for a given photon energy. The sensitivity of the detector largely depends on the inductor volume and Q_c. For a material with a given sheet impedance, the number of charge carriers is going to depend on the inductor volume. Therefore, a larger inductor will have a smaller fractional change in quasiparticle density for a given photon energy. This will result in a smaller phase signal. A smaller inductor volume will result in a higher sensitivity. The detector sensitivity can also be engineered by adjusting Q_c, as this dictates the signal strength that will be seen by the microwave transmission line. In order to keep the phase response sensitivity uniform across an array, the inductor volume and Q_c are generally kept constant.

Although the sensitivity can be easily increased, MKIDs only have a limited dynamic range. The phase response begins to become heavily nonlinear for photon energies that

produce phase pulses above about 120°. These large pulses will result in lower energy resolution when compared to phase pulses that remain in the linear regime. In order to avoid going into the nonlinear phase region, MKIDs are designed so that the most energetic photons produce $\sim 120°$ pulses, before the onset of nonlinearity. There is some work being done to handle nonlinear phase shifts, but it is still in its early stages.

3.2.5 Count Rate

Finally, there is the issue of count rate. In early versions of the readout, the count rate was limited by the FPGA resources. A maximum count rate of roughly 2500 cts/s was set in the readout with a 100 μs dead time between photon events. More recent generations of the readout do not have this limitation, and the maximum count rate is set by the quasiparticle lifetime. In order to maximize the resolving power of the array, phase pulses should overlap minimally. Therefore, shorter quasiparticle lifetimes allow for higher count rates, but this comes at the cost of more poorly sampling the pulses, which also degrades energy resolution. Often times, the quasiparticle lifetime can be tuned with the expected count rate of a specific application in mind.

3.3 Improvements from Novel Fabrication Methods

In this section, I will go over new fabrication methods that were used to attempt to improve MKID performance. I will focus on two of these methods that were given considerable attention. The first is focused ion beam milling, which attempts to correct for resonator defects after the standard fabrication process has been completed. Next, I will go over atomic layer deposition as a replacement for sputtering or other deposition techniques. This deposition process involves growing single atomic layers of a material at a time.

3.3.1 Focused Ion Beam Milling

One of the techniques used to try to improve pixel yield was focused ion beam (FIB) milling. The goal here was to test the resonator positions in frequency space after fabrication and then to move any colliding resonators with the FIB. The FIB used was part of the FEI Helios Dualbeam Nanolab 650 system and employed a high power gallium ion beam along with a scanning electron microscope (SEM) for imaging during the FIB process.

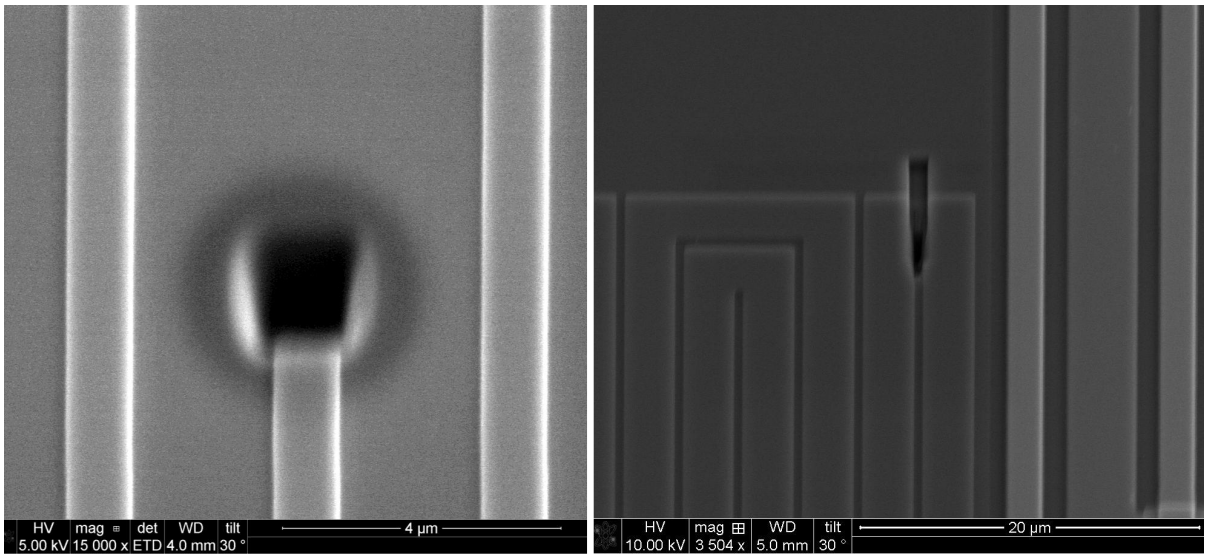

Figure 3.6: (Left) End of a capacitor leg that has undergone FIB milling. The decreased capacitance should increase the frequency of the resonator and move it into an unoccupied area of frequency space. (Right) A FIB cut through the inductor portion of the resonator. This stops current flow in the inductor, effectively eliminating the resonance. This was done in severe cases when the resonator could not be easily moved to an unfilled area of frequency space.

In order to shift a colliding frequency, the ends of that resonator's capacitor legs would be milled in order to decrease the capacitance. This method could only be used to shift resonant frequencies up. A calculated length of the capacitor would be milled carefully to put the resonator into an unoccupied area of frequency space. There were also groups of resonators that were heavily bunched with no free neighboring area of

frequency space. For these, it was often easier to altogether eliminate one out of the two colliding resonators in order to at least be able to regularly read out the other resonator. In order to do this, the inductor was cut with the FIB to eliminate any possible current flow through the inductor. SEM images of these two processes are shown in Figure 3.6.

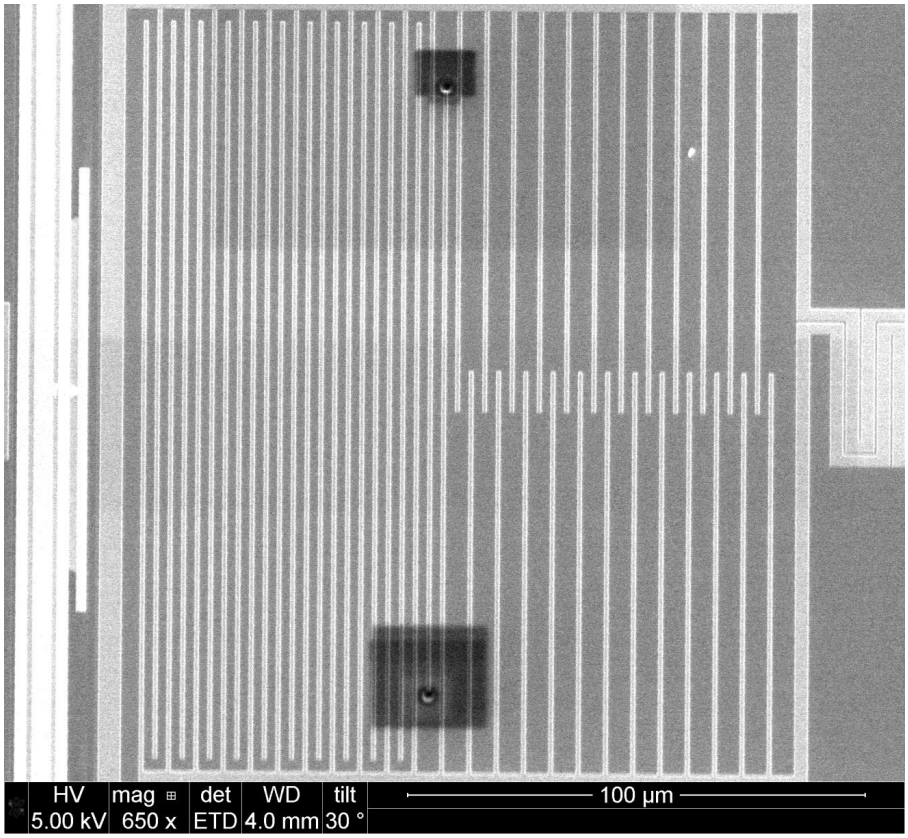

Figure 3.7: A SEM image of a MKID capacitor after its frequency has been shifted with FIB milling. Notice the dark squares in the area of the FIB cuts. This is due to the need to adjust the focus of the ion beam prior to the milling process, effectively leaving carbon burns and excess gallium ion implantation in areas surrounding the cuts. This caused somewhat random shifts of frequency for many resonators across the array, including those that did not undergo any FIB milling procedure.

FIB milling seemed to be a good path forward for adjusted important arrays that would be used inside astronomical instrumentation. Unfortunately, there were unexpected issues that arose from this technique. The main issue came about due to having to focus the ion beam. This would leave what were effectively carbon burns on the surface

of the array. In addition, the FIB would implant gallium ions in unwanted areas of the array, which changes the dielectric constant of the substrate. Both of these effects could cause random deviations in the resonator frequency, and we have seen that even neighboring resonators that were not necessarily processed with the FIB had their resonant frequencies shifted. Finally, the FIB milling process was very long and tool time was extremely expensive. There was also little room to automate and speed up the process with the particular tool that was being used. The FIB milling project was eventually abandoned for these reasons, but other ex-post facto frequency correction techniques are being investigated.

3.3.2 Atomic Layer Deposition

Another attempted fabrication method for improving the homogeneity of superconducting films was atomic layer deposition (ALD). This type of deposition works by successively pulsing a combination of precursor gases into a reaction chamber containing the substrate. Each precursor gas pulse grows an atomic layer of material on top of the substrate or the previously grown layer. The next precursor gas is then pulsed into the chamber, reacting with the layer under it and growing the next atomic layer. The cycle is repeated until a film of the desired thickness is grown. The advantage of using ALD is that each reaction is done to saturation, meaning that the gas quickly reacts with the previous layer and grows an atomic layer, but the reaction is such that it does not grow the film further until the next gas is pulsed. Unlike sputtering, ALD is done in a chamber with relatively poor base pressure, increasing the amount of impurities in the grown film. Attempts at using ALD to produce TiN films specifically are described in Section 3.5.2.

3.4 Improvements from New Superconducting Materials

Another path toward improving detector performance is using entirely different superconducting materials in the MKID resonator layer. The main idea is that other materials are likely to have higher spatial uniformity than sub-stoichiometric TiN while retaining some of TiN's more desirable qualities, such as high Q_i. In order to quickly screen new materials, a fabrication mask with multiple testing structures was designed. This mask included multiple chips, each tuned for a different sheet inductance, allowing the same mask to be used for a multitude of materials. The mask contained a number of resonators with the same geometries as those in the large-format arrays. It also contained a group of resonators spaced 2 MHz apart in order to test the uniformity in frequency placement and multiplexing capabilities. In addition, the test mask had a few $\lambda/4$ CPW resonators which were used in the early days of MKIDs. This allowed us to compare noise of our current resonators with archival data. The mask contained resonators with big capacitors, which are expected to have lower TLS noise due to a smaller fraction of the electric field being located at the superconductor-substrate interface. Although these resonators are too big to fit into large-format arrays, they could be used for testing MKID performance with paramps. Finally, the test mask included resonators with high Q_c. These were useful for testing resonators with very high Q_i as the total Q is dominated by the lowested of Q_c and Q_i, leading to large errors in the Q_i measurement when Q_c is its typical low value of $\sim 30,000$. An image of this test mask is shown in Figure 3.8.

A number of factors go into choosing new MKID material candidates. First of all, the T_C of the superconductor needs to be ~ 1 K in order to maximize performance at a 100 mK operating temperature. This significantly limits the superconductor choices, as there are only a handful of elemental superconductors in this region and few binary

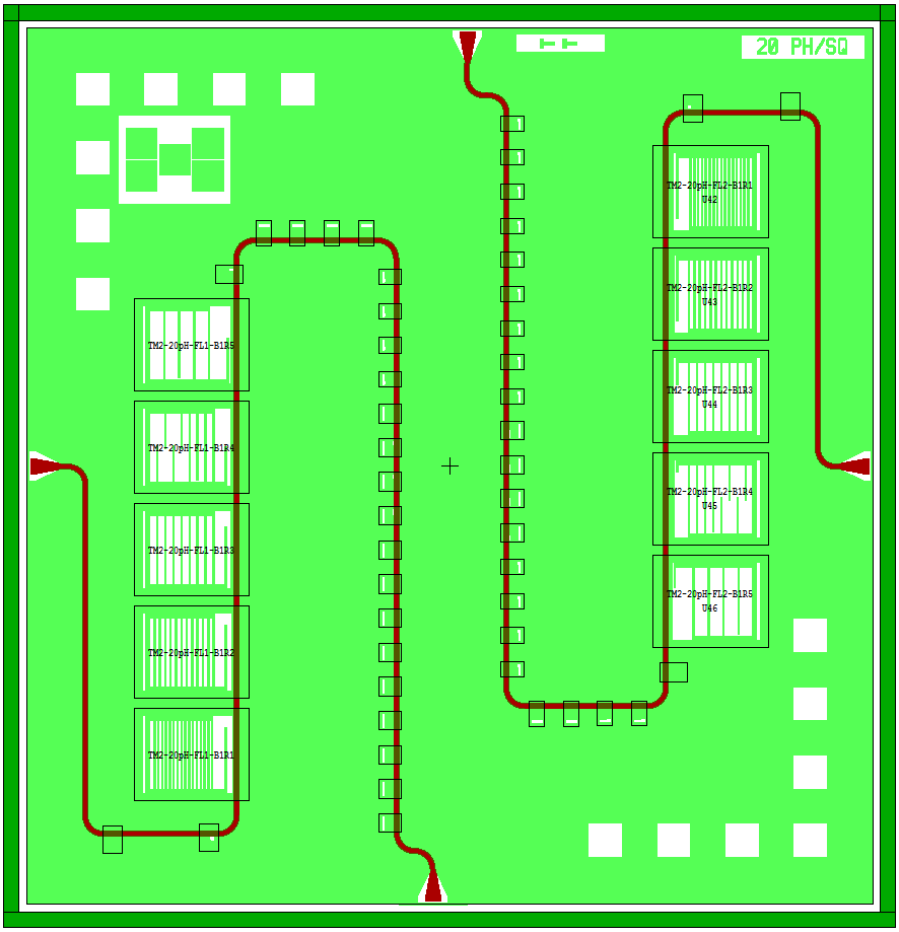

Figure 3.8: 20 pH/□ chip of a MKID fabrication test mask. This mask is used to quickly screen potential MKID material candidates of varying sheet impedance for a number of properties, such as T_C, Q_i, τ_{qp}, and R.

superconductors. Next, ease of fabrication is important. Typically, materials are chosen that could be easily produced in a general-use cleanroom facility. There is often very little data on the microwave properties of most low temperature superconductors, but often these materials are used for other applications and their room temperature properties are well established. The test mask can be used to screen superconducting resonator parameters such as T_C, Q_i, τ_{qp}, and R and quickly predict whether a material could be useful for large-format MKID arrays.

In the following section, I will present a paper detailing some of the early optical MKID development efforts. This paper focuses on the fabrication and performance of MKIDs made with ALD TiN and PtSi on silicon substrates. Although these resonators did not have the best performance, the PtSi on Si work in particular led to the important development of a PtSi growth process on sapphire substrates, as will be described in Chapter 4. Later in this chapter, I will discuss some other superconducting material development projects which have not had the same success as the PtSi on sapphire system for optical MKIDs, but may be useful for future applications.

3.5 Ultraviolet, Optical, and Near-IR Microwave Kinetic Inductance Detector Materials Developments

Abstract

We have fabricated 2024 pixel microwave kinetic inductance detector (MKID) arrays in the ultraviolet/optical/near-IR (UVOIR) regime that are currently in use in astronomical instruments. In order to make MKIDs desirable for novel instruments, larger arrays with nearly perfect yield need to be fabricated. As array size increases, however, the percent yield often decreases due to frequency collisions in the readout. The per-pixel performance must also be improved, namely the energy resolution. We are investigating ways to reduce frequency collisions and to improve the per pixel performance of our devices through new superconducting material systems and fabrication techniques. There are two main routes that we are currently exploring. First, we are attempting to create more uniform titanium nitride films through the use of atomic layer deposition rather than the more traditional sputtering method. In addition, we are experimenting with completely new material systems for MKIDs, such as platinum silicide.

3.5.1 Introduction

Microwave Kinetic Inductance Detectors (MKIDs [20, 48]) are a new type of superconducting technology capable of measuring the arrival times and energies of individual photons. MKIDs work using the principle of the kinetic inductance effect [22]. Energy can be stored in the supercurrent (or flow of Cooper pairs) of a superconductor. In order to reverse the direction of the supercurrent, energy must be removed from the superconductor, resulting in an additional kinetic inductance term. If a superconducting material is patterned into a resonator, light hitting the resonator will momentarily increase the kinetic inductance of the superconductor, thereby decreasing the frequency of resonance. The magnitude of this response is closely related to the energy of the incident photon. An array of these resonators can be read out using a single microwave feedline using a frequency domain multiplexing scheme [23]. As with traditional charge-coupled devices (CCDs), the energy of the incident photon must be above the bandgap energy in order for the photon to be absorbed. Superconductors have bandgap energies roughly 1000 times lower than that of silicon, allowing for the detection of much lower energy photons.

MKIDs are ideal in astronomy for observations of time-varying objects and those in which spectral information is important. Some examples of objects observed with ultraviolet/optical/infrared (UVOIR) MKIDs are ultra-compact binaries, pulsars, and galaxies. UVOIR MKIDs have been proven as successful astronomical detectors through the publication of the first two astronomy papers using MKIDs at any wavelength. These involved observations of the 33 millisecond spin period Crab Pulsar [37] and the 28 minute orbital period AM CVn system, SDSS J0926+3624 [39]. Observations were done using our MKID instrument, the Array Camera for Optical to Near-IR Spectrophotometry (ARCONS [35]). In the future, MKIDs will be used for speckle nulling in two funded exoplanet imagers, the Dark-speckle Near-IR Energy-resolved Superconducting Spectrophotometer

(DARKNESS) at the Palomar observatory and the MKID Exoplanet Camera (MEC) on the Subaru Telescope. Observations using ARCONS are also funded to continue.

Although MKIDs have begun producing results in astronomy, there is much room for improvement. Future instruments require much larger MKID arrays. From a fabrication standpoint, scaling up MKID arrays is straightforward. As the array size goes up, however, the percent pixel yield typically goes down. Non-uniformities in superconducting critical temperature across a device cause resonators to shift away from their intended resonant frequencies, resulting in resonator collisions in frequency space. Colliding resonators cannot be distinguished and therefore cannot be read out properly, reducing the usable pixel count. The per-pixel performance of MKIDs also needs to be improved. Improving the energy resolution is the main priority, followed by quantum efficiency. The energy resolution is mostly limited by two-level system (TLS [53]) and amplifier noise, whereas the quantum efficiency depends mostly on choice of material. There are fabrication processes used in similar low temperature detectors, such as development of optical cavities in transition-edge sensors [57], which have been shown to increase quantum efficiency. These methods, however, typically increase the TLS noise in the detectors resulting in lower energy resolution. We are investigating new material systems and fabrication techniques to address the most pressing issues of energy resolution and critical temperature uniformity. Current work is going into developing MKIDs using thin films of atomic layer deposition (ALD) titanium nitride and platinum silicide.

3.5.2 Atomic Layer Deposition Titanium Nitride

The current standard superconductor used in UVOIR MKID fabrication is sputtered TiN [36]. TiN is an ideal MKID superconductor due to its high kinetic inductance fraction, which leads to a large resonator responsivity due to incident photons. A higher

responsivity leads to a more accurate determination of the photon energy. Sputtered TiN films, however, suffer from non-uniformities in superconducting critical temperature across a wafer, which greatly reduces percent pixel yield. The critical temperature is tuned by controlling the stoichiometry in the TiN films, and deviations in the nitrogen flow rate during sputtering can cause the stoichiometry of the TiN film to vary across a wafer. Due to the high kinetic inductance fraction, slight deviations in critical temperature create fairly large differences in the actual resonator frequencies from their expected design frequencies. There have been multiple schemes developed to suppress these variations, such as stacking multilayers of stoichiometric TiN and pure Ti [49]. Atomic layer deposition of TiN is another proposed method to increase the uniformity of sub-stoichiometric TiN films, but much of this work is still in a very early phase. A previous study of the microwave properties of ALD TiN films was performed in Ref. [58].

We used a Beneq TFS 200 ALD system to grow thin films of TiN. The precursors used were $TiCl_4$ and NH_3. The precursor flow rates were the first two parameters that were varied in attempts to obtain a 1 K T_C film. The ALD process temperature was the third parameter that was varied. No plasma power was used, and the reaction energy was supplied completely by the thermal energy. A list of initial processing parameters and results is shown in Table 3.1.

Our initial tests showed that the critical temperature roughly decreased with processing temperature, when processed between 460–507°C. It should be noted that there was evidence of chemical vapor deposition (CVD) in addition to ALD for the 507°C and 495°C processing temperature samples, indicated by a laterally non-uniform film. This is the likely cause of the broad low temperature superconducting transitions in these two films. Another important result was measuring high quality factors for resonators structured out of these films. These internal quality factors were at the upper limits of our measurement technique, which is limited by our relatively low coupling quality factors.

Future work will involve finding ALD processing conditions that create a 1 K T_C TiN film and characterizing the uniformity in T_C across a device.

Table 3.1: Initial ALD Titanium Nitride Results

Process T (°C)	# Cycles	$TiCl_4$ Dose/Purge Times (ms)	NH_3 Dose/Purge Times (ms)	T_C (K)	Internal Quality Factor
507	2000	100/1500	250/3000	0.250–0.800	—
495	1000	100/1500	200/4000	0.150–0.500	—
490	1000	100/1500	100/3000	1.547–1.558	—
490	1000	50/1000	200/4000	2.121–2.130	—
460	1000	100/1500	200/4000	3.200–3.800	$(2–3)\times10^5$
460	2000	100/1500	100/3000	2.520–3.077	$(1–2)\times10^5$
460	2000	50/800	100/2000	2.922-3.242	$> 5 \times 10^5$

Initial results of thin TiN film depositions using ALD. Critical temperature decreased with increasing process temperature, but was largely uncontrolled. High resonator internal quality factors were measured, and these measurements were limited by the fairly low coupling quality factors of 30,000. Not all samples were patterned. Only patterned samples had measured internal quality factors.

3.5.3 Platinum Silicide

Platinum silicide was also explored as a possible replacement for titanium nitride as a MKID superconductor. Bulk stoichiometric PtSi has a T_C of 1 K, but the T_C is suppressed for films below 50 nm [59]. This results in a T_C in the desired range without having to alter the stoichiometry and risk creating non-uniformities in the array, as in the TiN case. PtSi is a fairly common material in semiconductor processing, and the room temperature properties are quite well characterized [60]. PtSi also has a high room temperature resistivity similar to that of sputtered TiN, indicative of a high kinetic inductance fraction. Most importantly, it is fairly simple to get PtSi into the desired stoichiometric state, as this is also the thermally stable state. A layer of platinum on a

silicon wafer can be easily annealed into a PtSi film.

To begin the deposition of our initial PtSi films, we cleaned a (100) high resistivity silicon wafer. We used nanostrip followed by hydrofluoric (HF) acid to remove the native oxide. The wafer was immediately brought into a CHA Industries SEC600 e-beam evaporator, where a 20 nm film of platinum was grown. The film was then brought into ultra-high vacuum (UHV) and annealed at 500°C for 20 minutes. This acts to create a PtSi layer that is roughly double the thickness of the initial platinum layer. The PtSi layer is then patterned into MKID test devices.

The initial samples showed TC of roughly 800 mK, which is within the optimal range of our cryogenic system. Photon events created quasiparticles with ∼20 μs lifetimes, measured by observing the duration of a phase difference caused by a photon event. The measured energy resolution, E/ΔE, was 8 at 400 nm, which is equal to the energy resolution of our sputtered TiN films [35]. Energy resolution is measured by looking at the phase response of resonators due to photon events from lasers of precisely known wavelengths. In our sputtered TiN films, the measured quantum efficiency is 70% at 400 nm and 25% at 1 μm. Preliminary count rate measurements in PtSi detectors indicate a similar quantum efficiency, and more precise quantum efficiency measurements will be made once the PtSi film thickness has been fully tuned for sensitivity. The quality factors were in the range of 10,000 to 30,000, which is much lower than what is observed in sputtered TiN films (Ref. [36] saw internal quality factors of substoichiometric TiN films of 5×10^6). Increasing this quality factor would make PtSi competitive as a replacement for TiN.

There are various methods that we are employing to try to increase the quality factors of our PtSi films. One method we investigated was attempting to alter the crystal phases of the PtSi films. The hope was that some crystal orientations were better than others for quality factor, an effect exhibited in our TiN films. We found that one way to alter crystal

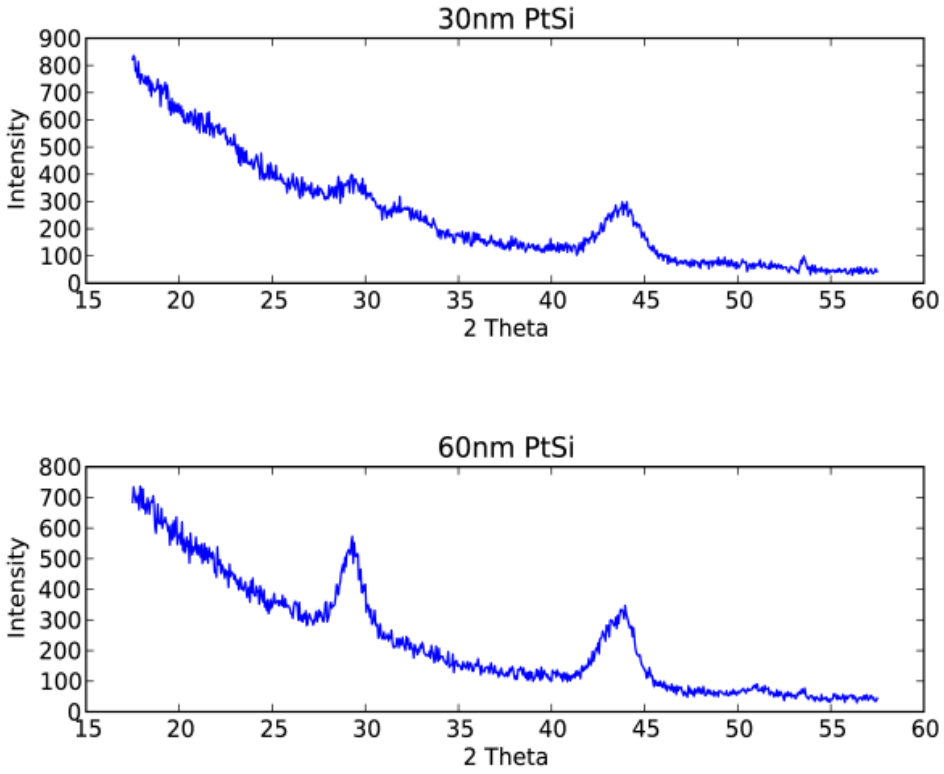

Figure 3.9: X-ray diffraction patterns for PtSi films of 30 and 60 nm film thicknesses. The peak at ∼29 degrees corresponds to the (101) orientation, whereas the peak at ∼43.5 degrees corresponds to the (121) orientation. In our initial depositions, decreasing the film thickness acted to suppress the (101) crystal phase.

structure was vary the PtSi film thickness, as can be seen in the X-ray diffraction pattern in Figure 3.9. Unfortunately we were unable to correlate the crystal phase differences to any significant increases in quality factor. Future work in altering the PtSi crystal structure will likely involve depositing platinum on different crystal orientation silicon substrates.

Another likely source for the low quality factors could be excess platinum diffusing into the silicon. Figure 3.10 shows secondary ion mass spectroscopy measurements of a 40 nm PtSi film grown on a silicon substrate. Instead of a sharp PtSi-Si interface, a gradual

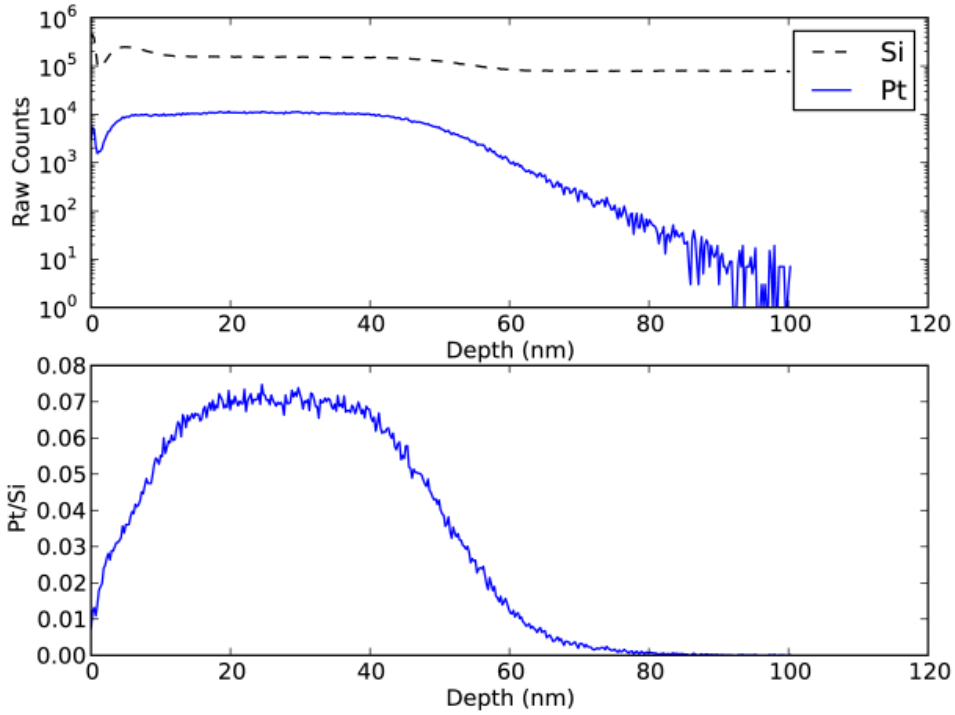

Figure 3.10: Secondary ion mass spectroscopy measurements of 40 nm PtSi film on silicon. Instead of a sharp decrease in the Pt/Si ratio at 40 nm, there is a gradual decline of almost 20 nm. This excess diffusion of platinum into silicon could be the cause of the low quality factors and is the major motivation for using a sapphire substrate.

decrease in the platinum to silicon ratio for ∼20nm is observed. For this reason, we attempted to grow a PtSi film on a sapphire substrate. To do this, we cleaned a sapphire wafer and deposited 25 nm of platinum via e-beam evaporation. Afterwards, the wafer was placed in an ICP PECVD system. The chamber pressure was held at 50 mTorr and temperature at 350°C, which was at the limits of the system. 30 sccm of SiH_4 was flowed through the chamber for upwards of two hours. Unfortunately, no appreciable PtSi layer was grown. It was apparent that a PECVD system with higher maximum gas pressures and temperatures would be required in order to match conditions of previous work with successful PtSi formation [61]. In the future, we will sputter platinum and silicon onto a

sapphire substrate, and continue by annealing the sample as in the PtSi on silicon case.

3.5.4 Conclusions

We investigated ALD TiN and PtSi as possible materials for use as MKID superconductors. Early tests of ALD TiN growth showed promising internal quality factors, but more work needs to be done in tuning the superconducting critical temperature to 1 K. In addition to higher quality factors, this process is expected to produce more uniform films. Once a 1 K T_C film can be repetitively deposited, we will perform extensive uniformity tests. For PtSi, producing films of the desired T_C was a fairly straightforward process. The quality factors of these films, however, were quite low, and future work will go primarily towards addressing this issue. The most promising solution is creating a process for growing a PtSi film on a sapphire substrate. Sputtering platinum and silicon on a sapphire substrate, and then annealing in-situ, will likely be the next step in this work.

Acknowledgements

This work was supported by a NASA Space Technology Research Fellowship (NSTRF). Fabrication work was done in the UCSB Nanofabrication Facility and NASA JPL's Microdevices Laboratory (MDL).

3.6 Other Superconducting Materials

There were a few other superconducting materials that were investigated in depth using the test mask. One of those materials was osmium. This material is interesting as it is one of the few elemental superconductors with a reported T_C near 1 K. We first

attempted ALD Os with the help of our collaborator Jani Hämäläinen from the University of Helsinki. These films had a T_C of 750 mK and a low Q_i of only about 15,000. This low value of Q_i was attributed to excess impurities in the ALD process, so sputtered Os was also attempted. The sputtered films had an unexpectedly higher T_C of 1.25 K and Q_i in the range of 40,000–80,000. The material had reasonable τ_{qp} of around 20 μs, but the energy resolution of these detectors was only about $R \sim 5$ due to the relatively low values of Q_i. Future work in developing Os resonators will go into improving the Q_i through methods such as oxygen treating the substrate prior to deposition and optimizing the sputtering conditions.

Niobium silicide is another material we put considerable amount of time investigating. The NbSi films were co-sputtered by our collaborator Helene le Sueur at CSNSM. These films had a T_C of 980 mK, close to the optimal T_C of ∼800 mK for our operating temperature. The resonators produced from these films also had remarkably high Q_i values of about 300,000–400,000. Unfortunately, NbSi turns out to have a very short τ_{qp} of about 3 μs, which is only slightly higher than the sampling rate of the readout. This puts an upper limit on R for NbSi MKIDs of about 5. This short quasiparticle lifetime, however, is ideal for membrane suspended detector concepts, such as TKIDs, where the timescale of interest is the much longer, thermalization time.

All of the aforementioned materials had T_C targeted at around 1 K so that they would be optimized for an operating temperature of 100 mK, as is used for the ADR systems that are brought to telescopes. Future advances in cryogenic technology could push this operating temperature further down, allowing us to use materials with a lower T_C. The advantage here would be a lower thermal noise floor, raising the theoretical limit on energy resolution by more than a factor of two. Very preliminary work on hafnium resonators with a T_C of ∼500 mK has been done using an advanced dilution refrigerator capable of achieving base temperatures of ∼10 mK. Although this fridge is more difficult

to put behind an optical telescope, the work could provide insights on the performance of low T_C MKIDs.

Chapter 4

Platinum Silicide on Sapphire

4.1 Background

In the previous chapter, I discussed some early work with depositing PtSi films on Si substrates. Resonators made with these films had lower than expected Q_i due to excess diffusion of Pt into the Si substrate, resulting in no clear interface between the superconducting film and the substrate. To remedy this, a process for growing PtSi on sapphire substrates was developed. In the following section, I will present a paper detailing the fabrication and characterization of superconducting PtSi resonators on sapphire substrates. Afterwards, I will go over some properties of the PtSi process that were discovered only after the publication of this paper, such as improved performance due to aggressive substrate cleaning techniques and sputtering parameters. PtSi on sapphire resonators had fairly substantial performance improvements over TiN resonators, and for this reason they were incorporated into the full large-format science array fabrication process. This will be discussed more in Chapter 5.

4.2 High Quality Factor Platinum Silicide MKIDs

Abstract

We report on the development of Microwave Kinetic Inductance Detectors (MKIDs) using platinum silicide as the sensor material. MKIDs are an emerging superconducting detector technology, capable of measuring the arrival times of single photons to better than two microseconds and their energies to around ten percent. Previously, MKIDs have been fabricated using either sub-stoichiometric titanium nitride or aluminum, but TiN suffers from spatial inhomogeneities in the superconducting critical temperature and Al has a low kinetic inductance fraction, causing low detector sensitivity. To address these issues, we have instead fabricated PtSi microresonators with superconducting critical temperatures of 944±12 mK and high internal quality factors ($Q_i \gtrsim 10^6$). These devices show typical quasiparticle lifetimes of $\tau_{qp} \approx 30$–40 μs and spectral resolution, $R = \lambda/\Delta\lambda$, of 8 at 406.6 nm. We compare PtSi MKIDs to those fabricated with TiN and detail the substantial advantages that PtSi MKIDs have to offer.

Introduction

Microwave Kinetic Inductance Detectors (MKIDs [20]) are low-temperature detectors capable of measuring the arrival times of single photons to better than two microseconds and their energies to around ten percent. MKID operation depends on the kinetic inductance effect [22], an additional inductance term which can be exploited for single photon detection. Cooper Pairs are broken when a superconductor below its T_c absorbs a photon, creating a population of unpaired electrons called quasiparticles. The sudden decrease in Cooper Pair density temporarily increases the kinetic inductance of the superconducting film. If a thin film superconductor is lithographically patterned into a microresonator, a photon absorption event will then act to momentarily decrease the resonant frequency of

the microresonator. The energy of the incident photon is proportional to the number of broken Cooper Pairs, and therefore the change in frequency, giving MKIDs spectral resolution. MKIDs are naturally multiplexed by assigning each microresonator in an array a unique frequency during lithography. They can then be read out [23] using a frequency domain multiplexing scheme. With this method employed on the newest generation of digital microwave electronics, thousands detectors can be coupled to and read out using a single microwave transmission line [24].

Because the bandgap Δ of a superconductor is roughly 10^4 times smaller than that of the silicon used in conventional charge-coupled devices (CCDs), MKIDs are capable of detecting the long wavelength photons that would typically pass right through a CCD. MKIDs can be operated over a broad wavelength range and a handful of MKID astronomy instruments in the submillimeter [26, 29] and the ultraviolet, optical, and near-infrared (UVOIR) [35, 40] wavelength bands have been commissioned. Although our work is primarily focused on the UVOIR regime, MKIDs operating at all wavelengths benefit from advances in the superconducting sensor layer.

We have chosen platinum silicide as the superconductor in our devices in order to avoid the problems observed in previously fabricated sub-stoichiometric titanium nitride [36, 49] and aluminum [62] MKIDs. In TiN MKIDs, thin films are deposited by reactively sputtering off of a Ti target in a nitrogen atmosphere, and the N_2 flow rate can be used to control the TiN stoichiometry and T_c. Unfortunately, for a given Ti sputtering power, the T_c is highly sensitive to the N to Ti ratio near the desired T_c of 1 K [36]. This particular method leads to local and long-range variations in T_c (and sheet inductance) across the wafer [49], causing the microresonators to shift away from their design frequencies. Microresonators overlapping in frequency are unable to be read out, lowering the overall detector yield. This issue is only exacerbated in large format arrays where microresonators need to be spaced closely together in frequency space to

stay within the bandwidth of the readout electronics. Attempts have been made to make TiN more uniform through multilayer stacking of TiN/Ti/TiN [49], but this technique is incompatible with several essential UVOIR MKID fabrication steps. Al, on the other hand, can be deposited very uniformly but has a short London penetration depth (50 nm, compared to $\sim$1 μm for TiN), indicating it has a high Cooper pair density, therefore explaining its low kinetic inductance fraction. In order to maintain a high sensitivity (a large phase shift per number of broken Cooper Pairs), the Al film needs to be very thin ($\lesssim$ 5 nm), but this creates severe issues with oxidation and photon absorption. On top of this, Al is very reflective to UVOIR photons, making overall detector quantum efficiency even lower. Al is also known to exhibit long quasiparticle recombination times of $\gtrsim$ 1 ms after photon hits, making the material unsuitable for applications that require single photon detection at high count rates ($\gtrsim$ 100 counts/s).

PtSi was chosen as a candidate material for the MKID superconductor for a number of reasons. Deposition of PtSi is fairly well understood, and its thin film, room temperature electronic and optical properties have been measured [60]. Many of the PtSi superconducting properties have also been studied [59], including a measured T_c value of $\sim$1 K which decreases with thickness for films thinner than 50 nm. Typically, PtSi films are formed by first depositing Pt on a high resistivity Si substrate. The sample is then annealed at temperatures above 300° C, causing the Pt to diffuse into the Si and form a PtSi film of roughly twice the initial Pt thickness. With this method, the thermally stable state consists of one Pt atom for every Si atom, and fortuitously this happens to be a state with a T_c of $\sim$1 K for films thicker than 50 nm [59]. This method was employed to fabricate the initial PtSi MKIDs, but the resulting resonators had low internal quality factors, Q_i due to excess Pt diffusion deep into the Si substrate [63]. A new method was designed to improve Q_i by utilizing a sapphire substrate as a Pt diffusion barrier. The remainder of this discussion will involve PtSi MKIDs grown on sapphire substrates.

4.2.1 Fabrication

To begin, a sputter system with a base pressure of $\sim 10^{-7}$ Torr was used to deposit a 30 nm Pt film on a one-side polished C-plane (0001) sapphire wafer. A 45 nm Si film was then sputter deposited on top of the Pt film and the sample was annealed at 500° C for 25 minutes, resulting in a PtSi film of roughly 60 nm. These steps were all done in situ without breaking vacuum. The resulting PtSi film was then patterned with simple one layer MKID test structures using a deep UV stepper. The film was dry-etched using an inductively coupled plasma etcher with a combination of Ar, Cl_2, and CF_4 gasses. The resonators were designed with 40×40 μm meandered inductors and 200×160 μm interdigitated capacitors with variable leg lengths, putting the resonators into a 4–8 GHz frequency range.

4.2.2 Measurements

Low temperature testing to measure the PtSi superconducting properties was done using a dilution refrigerator capable of cooling devices down to ∼85 mK. A T_c of 944±12 mK was measured using a DC resistance testbed during the cool down. At base temperature, a vector network analyzer was used to find the locations of the resonators in frequency space. By comparing the locations of these resonators to their design frequencies, and noting a design sheet inductance of 10.0 pH/□, we measured the average local PtSi sheet inductance to be 8.2±0.2 pH/□.

Once the exact locations of the resonators were known, an analog microwave readout system was used to send and receive probe tones scanning the frequency space around the device resonant frequencies. The complex transmission was measured near resonance and individual resonators were fit using a capacitively coupled LC resonator model [46]. Of the resonators with a good fit, a mean Q_i value of 1.06×10^6 was calculated. Because the

total quality factor is dominated by the smallest of Q_i and Q_c (coupling quality factor), there is a large inherent spread in the fitted Q_i when it is much larger than Q_c (designed to be between 40,000–50,000). In this case, a standard deviation in Q_i of 5.5×10^5 was measured. The mean measured Q_c for these resonators was 38,000. These values of Q_i are among the highest seen in superconducting microresonators among a wide variety of materials.

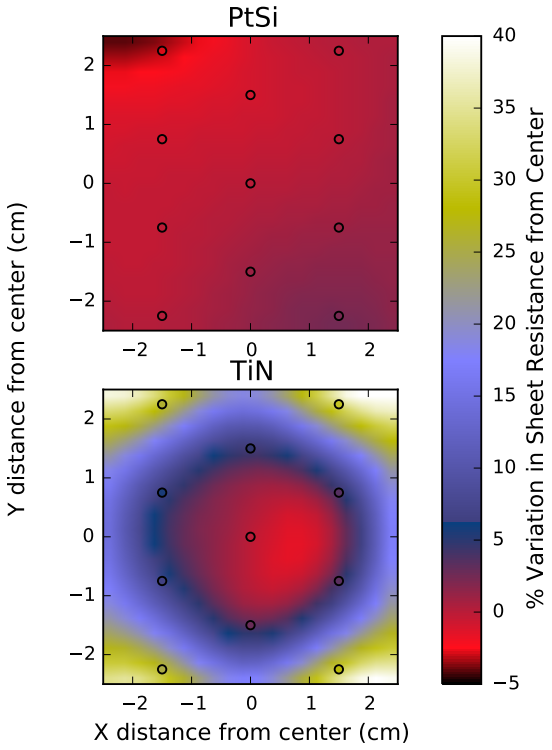

Figure 4.1: Percent variation in sheet resistance of PtSi and TiN thin films from the center of a 4" wafer. Measurements were done at the locations of the circles and the filled contour map was generated using a radial basis function interpolation.

The uniformity of the PtSi devices was also measured and compared to that of devices fabricated using sub-stoichiometric TiN, as non-uniformity in T_c is the most significant problem currently plaguing TiN MKIDs. For these superconducting films, the uniformity in room temperature sheet resistance can often be used as a rough proxy for uniformity

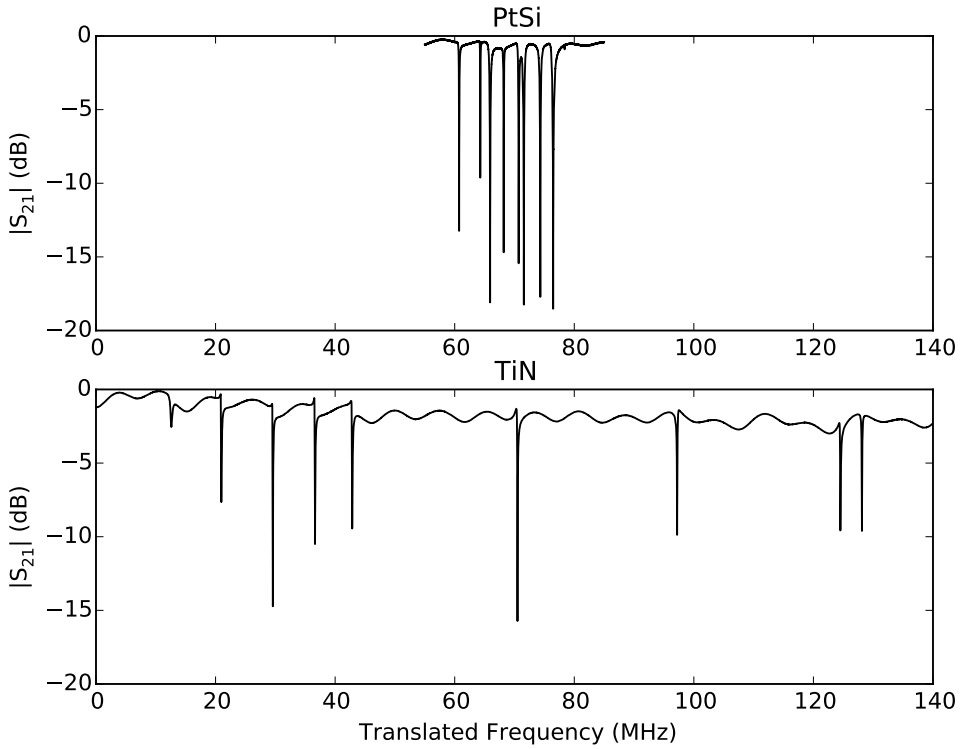

Figure 4.2: Wide frequency sweep of identical resonator structures designed at 2 MHz spacing for PtSi (top) and TiN (bottom). The base line has been translated to 0 dB for clarity. The frequency has also been shifted to 0 MHz for an easier comparison of the TiN and PtSi devices. An offset of 4.845 GHz is present for PtSi and 3.620 GHz for TiN. The seventh PtSi resonator in the sequence is missing due to a photomask error.

in T_c. Figure 4.1 shows the percent variation of film sheet resistance from the center of a 4" wafer for PtSi and TiN. These measurements show almost an order of magnitude better uniformity in PtSi than in TiN. The fabrication mask also contains a group of resonators closely spaced in frequency with a designed spacing of 2 MHz. This is meant to resemble the 2 MHz spacing used between detectors in large format MKID arrays. Complex transmission magnitudes for identical structures made with PtSi and TiN are shown in Figure 4.2. Note that the PtSi resonators spread out to around 20 MHz of bandwidth, whereas the TiN resonators spread to 120 MHz. The total bandwidth of the

9 resonators was designed to be 16 MHz. It can be seen that the frequency variations are less pronounced in PtSi than in TiN, allowing for finer multiplexing and a smaller number of frequency collisions.

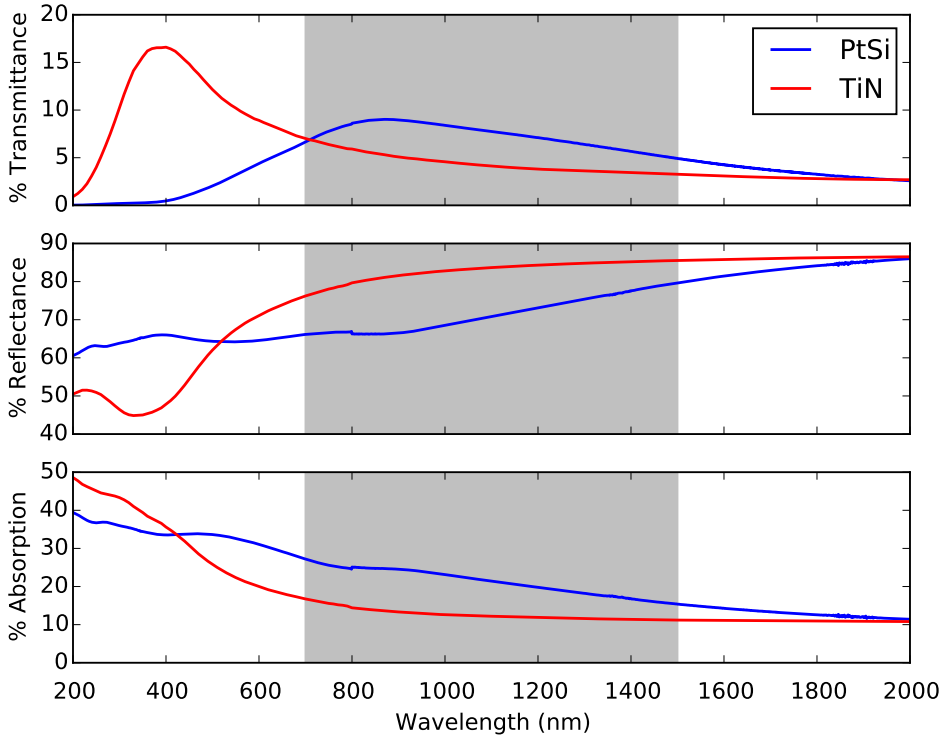

Figure 4.3: Optical transmittance, reflectance, and absorption measurements of unpatterned 60 nm PtSi (blue) and sub-stoichiometric 1 K T_C TiN (red) thin films on a sapphire substrates. The shaded region represents the wavelength band of the upcoming MKID instrument, DARKNESS[40]. The slight discontinuity at 800 nm is the result of the spectrophotometer switching its light source.

Room temperature transmittance, reflectance, and absorption measurements of unpatterned PtSi films were done using an Agilent Cary 5000 wideband spectrophotometer and are shown in Figure 4.3. This data is used to determine an upper limit on quantum efficiency of our detectors over the wide wavelength range in which they operate. The data was compared to that of a sub-stoichiometric TiN film typically used in MKIDs. TiN has better absorption than PtSi at shorter wavelengths, however, at wavelengths

over 425 nm, PtSi starts to outperform the TiN. This will be useful as future UVOIR MKID exoplanet imaging instruments [40] start pushing further into the near-IR regime.

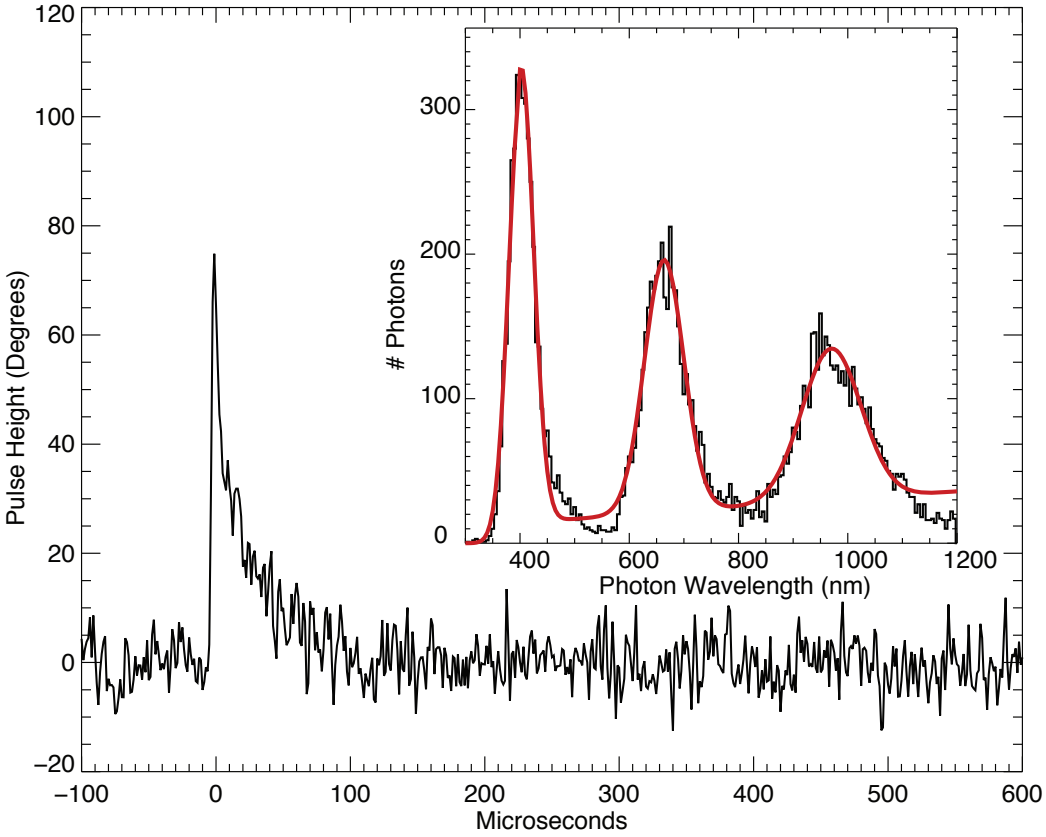

Figure 4.4: A typical single 671.0 nm photon being absorbed by a PtSi MKID with f_0=4.876 GHz, Q_c=15,700, and Q_i=147,300. The fitted quasiparticle recombination time is 36 ± 2 μs. Inset: The spectrum of the same MKID that has been illuminated with 406.6, 671.0, and 982.1 nm lasers. The data is transformed from phase height into wavelength using these known laser wavelengths[51]. The red line is a fit with three Gaussians and a linear background term, yielding a nearly uniform spectral resolution R=$\lambda/\Delta\lambda$=8 across the entire 400–1000 nm range.

Photon testing was done in an adiabatic demagnetization refrigerator with optical access. As explained earlier, when a photon hits a superconducting microresonator, it shifts the resonant frequency of the microresonator. One can determine the energy of the photon by measuring this frequency shift, but in the MKID readout, each resonator is read out using only a single, unique probe tone, making this type of measurement

difficult. The frequency shift will, however, cause a change in the amplitude and phase of the complex transmission at the particular probe tone. Measuring the phase shift tends to result in higher signal-to-noise ratios, and the phase can also be converted to energy in a straightforward way [51]. In order to measure the spectral resolution of the device it was illuminated with three lasers of known wavelength and a histogram was created, as shown in Figure 4.4. The histogram was fit to a model of three Gaussians (one for each laser) and a linear background term. Typical PtSi resonators had spectral resolutions R=$\lambda/\Delta\lambda$=8 at 406.6 nm and quasiparticle recombination times $\tau_{qp} \approx$ 30–40 μs. The spectral resolution in the PtSi device was very similar to the results achieved in TiN resonators of similar geometry.

Noise measurements, shown in Figure 4.5, were made using $\lambda/4$ coplanar waveguide (CPW) resonators with a 3 μm center strip and 2 μm gaps. The data is compared with previous measurements [64] from Al on Sapphire and Nb on Si resonators, and the results match expectations extremely well despite the number of photons in the resonator (a more generic proxy for the resonator readout power) differing by nearly four orders of magnitude. This indicates that the PtSi is adding no extra two-level system (TLS) noise [53] compared to standard MKID materials. The graph also includes some data from similar $\lambda/4$ CPW resonators made from TiN on Si, and these resonators do appear to be systematically slightly less noisy than the Al, Nb, and PtSi.

4.2.3 Discussion

MKIDs for UV, optical, and near-IR photon detection are extremely promising detectors for astronomical observations, but they need improvements in three distinct areas: pixel yield, spectral resolution and quantum efficiency. First, the much more uniform nature of PtSi, shown in Figures 4.1 and 4.2, indicates that it exhibits little frequency

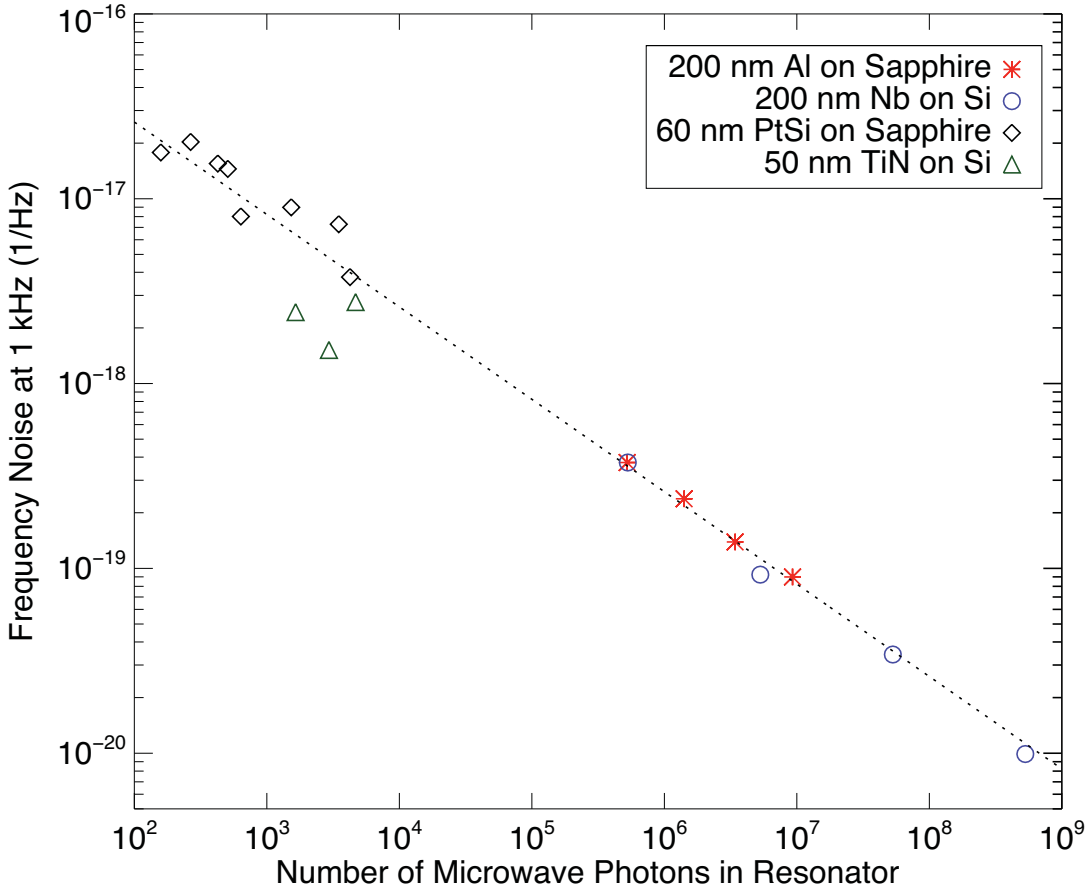

Figure 4.5: Fractional frequency noise (1/Hz) at 1 kHz as a function of the number of photons in a $\lambda/4$ CPW resonator. PtSi and TiN resonator measurements are plotted together with archival data of measurements of Nb on Si and Al on sapphire resonators[64]. The dashed line has a power law slope of -0.5 to guide the eye with the expected change in noise as a function of photon number.

scatter, which should dramatically improve pixel yield. Next, we see a significant discrepancy between the observed R and the R predicted from the formalism of optimal filtering [52] in the best TiN on Si MKIDs. We believe this is due to the non-uniformity of the TiN bandgap extending down to very small spatial scales [65] and the short quasiparticle diffusion lengths causing a different number of quasiparticles to be generated at different locations along the length of the inductor. In PtSi on sapphire we have seen a good match between predicted and observed R. This means as we improve our detector and readout design to reduce TLS and HEMT noise we expect to see improvements

in R beyond the hard limit of R≈10 we see in TiN. Finally, PtSi offers significantly higher quantum efficiency than TiN in the critical near-IR area where MKIDs will be used for exoplanet direct imaging work behind adaptive optics systems [40], as shown in Figure 4.3.

PtSi on sapphire appears to be a significant breakthrough for photon counting MKIDs, and development of 10 kpix PtSi on sapphire MKID arrays is proceeding. There are still paths forward for further raising the Q_i, such as more advanced sapphire substrate cleaning procedures [54]. In addition, going to ultra-high vacuum sputter chambers with lower base pressures will help to reduce impurities in the PtSi films, further improving Q_i.

Acknowledgements

This work was supported by a NASA Space Technology Research Fellowship (NSTRF). Fabrication was done in the UCSB Nanofabrication Facility. The authors would like to thank the Las Cumbres Observatory Global Telescope (LCOGT) network for assisting in broadband quantum efficiency measurements and Omid Noroozian for providing archival noise data.

4.3 PtSi on Sapphire Sputtering and Annealing Parameter Space Exploration

We had produced high internal quality factor PtSi resonators using the sputter tools in the general use clean room facility at UCSB. These sputter tools are not dedicated to deposition of superconducting materials, and many other metals, nitrides, and oxides are deposited using the tool. This often caused deviations in the quality of the deposited

PtSi films due to cross-contamination from prior depositions. In addition, the Pt and Si targets would often be exchanged for other targets depending on the demand for other materials in the tool. Finally, because this was a general use facility, tool time was often limited, making it difficult to perform an in-depth investigation of the PtSi material system.

For the above reasons, we made the decision to purchase our own private sputtering system. This tool was optimized for superconductor deposition. On top of the regular turbo pump used to get the tool to $\sim 10^{-8}$ Torr base pressure, a cryo pump was added which brought the pressure further down into the $\sim 10^{-10}$ Torr levels. On top of this, no oxygen or nitrogen gases were used as reaction gases (nitrogen was still used for chamber purging during maintenance), further reducing the non-superconducting impurities in the tool. The tool contained 3" targets instead of the smaller 2" targets used in the general use facility, improving the thickness uniformity of sputtered films. In addition, it had a substrate heater installed that could be ramped up to 1000°C, allowing us to perform the PtSi annealing process in-situ after the deposition.

The PtSi deposition process had to be re-optimized for this new sputter system. Also, having a private sputter system allowed us to perform a parameter space exploration of the PtSi material system. A number of parameters were explored to try to optimize the PtSi deposition process, including platinum to silicon ratio, annealing temperature and time, and temperature ramp rates. The fabrication conditions and results of this study are shown in Tables 4.1 and 4.2 and are discussed in more detail in the subsections below.

4.3.1 Platinum to Silicon Ratio

The ratio of platinum to silicon atoms was perhaps one of the most important parameters for the determination of internal quality factor. Theoretically, a 1:1 Pt to Si ratio

Table 4.1: PtSi Sputtering and Annealing Parameters

Wafer ID	Pt:Si # Ratio	Annealing T (°C)	Annealing Time (min)	Cooldown Speed	Holder Type
20160917	1 : 0.99	500	25	Slow	Plate
20160919a	1 : 0.99	200	25	Slow	Plate
20160919b	1 : 0.99	800	25	Slow	Plate
20160922a	1 : 0.99	350	25	Slow	Plate
20160922b	1 : 0.99	650	25	Slow	Plate
20160924	1 : 0.99	550	25	Slow	Plate
20160925	1 : 0.99	600	25	Slow	Plate
20160928a	1 : 0.99	550	25	Slow	Plate
20160928b	1 : 1.19	550	25	Slow	Plate
20160928c	1 : 1.04	550	25	Slow	Plate
20160930	1 : 0.99	500	25	Slow	Plate
20161002	1 : 0.99	500	25	Fast	Sputter 3
20161004a	1 : 0.89	550	25	Slow	Plate
20161004b	1 : 0.79	550	25	Slow	Plate
20161006a	1 : 0.94	550	25	Slow	Plate
20161006b	1 : 0.99	300	25	Fast	Ring
20161008	1 : 1.14	300	25	Fast	Ring
20161008	1 : 1.14	300 + 500	25 + 25	Fast + Fast	Ring + Plate
20161011	1 : 1.09	550	25	Fast	Plate
20161012	1 : 1.09	450	25	Fast	Plate
20161014	1 : 1.09	550	50	Fast	Plate
20161016	1 : 1.09	550	100	Fast	Plate
20161018	1 : 1.09	450	100	Fast	Plate
20161018	1 : 1.09	450 + 500	100 + 25	Fast + Fast	Plate + Plate
20161019	1 : 1.09	350	100	Fast	Plate
20161019	1 : 1.09	350 + 500	100 + 25	Fast + Fast	Plate + Plate
20161024	1 : 1.09	300	100	Fast	Ring
20161025	1 : 1.09	300	100	Fast w/ Ar	Ring
20161029	1 : 1.09	300	100	Fast	Ring
20161029	1 : 1.09	300 + 500	100 + 25	Fast + Fast	Ring + Plate

Table of parameters probed in order to optimize the PtSi growth process. Wafers with multiple annealing temperatures, times, cooldown speeds, and holder types are those that were re-annealed to test the effects on Q_i. Slow cooldown speeds are those that were ramped down at rates of roughly $0.1°C/s$. The holder type refers to a heavy and thick inconel plate with slow thermalization and a thin inconel ring with fast thermalization.

Table 4.2: PtSi Microresonator Results

Wafer ID	Sheet Resistance ($\Omega/\square$)	T_C (mK)	Q_i ($\times 10^3$)	Notes
20160917	6	935	20	
20160919a	6.75	820	Low	
20160919b	5	960	70	Only CPW resonators present
20160922a	—	865	5	
20160922b	—	935	25	
20160924	5.75	950	20	
20160925	5.5	950	27	
20160928a	6	935	30	
20160928b	6.5	925	15	
20160928c	6	945	27	
20160930	7.5	915	15	20% thinner
20161002	7	—	Low	
20161004a	8.2	<140	Low	
20161004b	8	<140	Low	
20161006a	9	<140	Low	Nonuniform resistance
20161006b	9	160	Low	Nonuniform resistance
20161008	6.25	775	Low	
20161008	—	990	90	Re-annealed
20161011	6	730	Low	
20161012	6.6	720	Low	
20161014	6.1	958	20	Only CPW resonators present
20161016	6	946	50	
20161018	6.4	949	—	
20161018	—	—	200	Re-annealed
20161019	7.3	922	50	
20161019	—	—	100	Re-annealed
20161024	7.8	927	100	20% thinner
20161025	8	945	30	20% thinner
20161029	12	923	40	54% thinner
20161029	—	—	400	Re-annealed

Measured microresonator results for the parameters explored in Table4.1. The wafer IDs in this table coincide with the ones in the previous table. Some values are omitted due to the difficulty of the measurement, especially when it came to re-annealed samples which were often already diced into small test chips.

is necessary for a 1 K T_C PtSi films, but we found that around a 10% silicon excess was ideal for high Q_i in PtSi. As is shown in the tables, a PtSi film with a low fraction of silicon has reduced T_C. On the other hand, a film with excess silicon has a T_C near 1 K, but the quality factor of the resonators is reduced. This was attributed to additional TLS noise due to the excess Si, which would act as an extra interface where TLSs could exist.

4.3.2 Annealing Temperature

In terms of PtSi annealing temperature, a number of values between 200 and 800°C were probed. Generally, the higher the annealing temperature ended up being, the lower the sheet resistance of the film turned out to be. For annealing temperatures near 800°C, the Q_i of the films was significantly reduced. This was attributed to being too close to the euctectic point of PtSi and was evidenced by relatively large spots of discoloration across the wafer. Films annealed at too high temperature also caused the Si to bunch up into islands rather than be distributed uniformly across the wafer. PtSi films annealed at the other extreme (∼200°C) had low T_C. This was due to an insufficient energy for the full diffusion of Pt and Si atoms, leaving inhomogeneous PtSi film. These films also tended to have unmeasurably low values of Q_i.

4.3.3 Annealing Time

The annealing time was also studied. Here, the longer the annealing time, the lower the sheet resistance of the film. Generally, the annealing time had very little impact on T_C and Q_i for wafers annealed for at least ∼20 minutes. The diffusion process seemed very quick when the wafer is under vacuum and the annealing temperature is high enough.

We also studied the effects of re-annealing chips after the conclusion of the fabrication

process. This seemed to increase the Q_i of the resonators significantly, but the homogeneity of the films was greatly reduced. The cause of this was attributed to selectively etching the Si on the sidewalls of the resonators faster than the Pt, causing excess Pt on the sidewalls. The re-anneal would redistribute the Pt atoms away from the sidewalls and into the bulk of the PtSi films in an uncontrolled way.

4.3.4 Temperature Ramp Rates

The temperature ramp rates for both heating up and cooling down a sample were also studied. The temperature ramp up rate directly after deposition had little effect on the final internal quality factor of the MKID resonators. The cooldown rate had a bigger impact on the T_C and Q_i. A slow cooldown rate increases the effective annealing time of the wafer. In addition, various temperature dependent crystal states can form during a slow cooldown and be frozen into the film when it reaches room temperature. Generally, the highest quality wafers were allowed to be cooled down on their own with no temperature ramp while still under vacuum.

4.4 The Importance of Sapphire Substrate Cleaning

The PtSi parameter space exploration led to many important discoveries regarding the PtSi material system, but many of these findings were insignificant compared to the importance of sapphire substrate cleaning techniques. The single most influential parameter for Q_i in PtSi films turned out to be an O_2 plasma descum of the wafer prior to deposition. For this process, an aggressive plasma with temperature >350°C is used. The wafer cleaning has raised the Q_i of PtSi resonators by about an order of magnitude, from about 10^5 for wafers without plasma treatment to about 10^6 to those with O_2 treatment.

There are other wafer cleaning techniques known to increase the quality factor of superconducting resonators, but often these techniques take a considerable amount of time to develop. One possible way to more thoroughly clean the wafer prior to deposition would be to do a more aggressive wet cleaning, such as through the use of piranha solution. Other methods involve an in-situ cleaning of the wafer inside the sputter chamber. This could be done through an ion milling of the substrate surface. Also, the wafer could be baked out inside the chamber to remove any residual water from the wafer surface after the cleaning process. Finally, this bakeout could be done in an O_2 atmosphere, allowing for a reconstruction of the Al_2O_3 wafer surface. This final method has been shown to raise the Q_i of superconducting resonators in the past [54], and it will be the most likely path forward for significant improvements in Q_i in PtSi resonators.

Chapter 5

Large-Format PtSi MKID Arrays

5.1 Background

After optimizing the PtSi deposition process with the new private-use sputter tool, the material was chosen for the superconducting resonator layer in large-format MKID arrays. This was done primarily to replace the TiN resonators, which suffered from local and large-scale inhomogeneity in T_C, severely reducing usable detector yield. As was discussed in Chapter 4, PtSi resonators showed improved homogeneity over the TiN films. In addition, the PtSi test mask resonators shared some of the more desirable TiN qualities, such as a T_C of $\sim$1 K, Q_i of $>10^6$, and R$\sim$8 at 808 nm.

In the following section, I will be presenting a paper in preparation detailing the fabrication and early characterization of large-format MKID arrays for the DARKNESS and MEC instruments. The work is on-going, and the fabrication process continues to be optimized for improved array performance. Also, more detailed measurements of the arrays from the most recent fabrication run are currently underway. The paper is likely to receive significant changes before final publication.

5.2 Large-Format Platinum Silicide Microwave Kinetic Inductance Detectors for Optical to Near-IR Astronomy

Abstract

We have fabricated and characterized 10,000 and 20,440 pixel MKID arrays for the Dark-speckle Near-IR Energy-resolved Superconducting Spectrophotometer (DARKNESS) and the MKID Exoplanet Camera (MEC). These instruments are designed to sit behind an adaptive optics system with the goal of directly imaging exoplanets in a 700–1400 nm band. These MKIDs are designed with a readout band of 4–8 GHz, with 2 MHz spacing between resonators. Previous large optical and near-IR MKID arrays were fabricated using titanium nitride (TiN) on a silicon substrate. These arrays, however, suffered from severe non-uniformities in the TiN critical temperature. This caused resonances to shift away from their designed values, lowering usable detector yield. We have begun fabricating DARKNESS and MEC arrays using platinum silicide (PtSi) on sapphire. Not only do these arrays have much higher uniformity than the TiN arrays, resulting in higher pixel yields, they also display improved sensitivity to photons within the 700-1400 nm band of operation. PtSi MKIDs do not display the hot pixel effects seen when illuminating TiN on silicon MKIDs with photons shorter than 1 micron. PtSi MKIDs have also demonstrated better energy resolution than we see in TiN MKIDs of similar design.

5.2.1 Introduction

Over the past three decades, Low Temperature Detectors (LTDs) have found a breadth of new applications in a number of fields, such as Astronomy and beamline science. These detectors operate by exploiting various superconducting phenomena, and they can be separated roughly into two groups. The first group consists of thermal detectors, which operate by measuring temperature changes in an absorbing material due to incident photon power. Transition-edge sensors (TESs [3, 1]) are the most common detectors in this group. Their principle of operation involves biasing the detectors at the superconducting transition temperature, an area with a high temperature coefficient of resistance, resulting in high sensitivity to photon energy and therefore resolving power. Alternatively, there are more exotic thermal detectors such as metallic magnetic calorimeters (MMCs [11, 12]), which use magnetism to do this temperature measurement.

Athermal, or non-equilibrium, detectors make up the second of these groups of LTDs. These detectors work by measuring the number of quasiparticles that are generated when a photon strikes a superconductor and breaks Cooper Pairs. The energy of the incident photon is proportional to the number of quasiparticles generated, giving these detectors energy resolution. Examples of athermal LTDs include Superconducting Tunnel Junctions (STJs [13]) and Microwave Kinetic Inductance Detectors (MKIDs [20, 21]). MKIDs are described in considerable detail below.

LTDs have a few chief advantages over more conventional charge-coupled devices (CCDs). The superconducting bandgap is roughly 10^4 times smaller than that of silicon, the material used in CCDs. This allows for the detection of radiation at lower energies than would be possible with CCDs, making these detectors extremely useful for submillimeter astronomy and the cosmic microwave background (CMB). For photon energies well above the bandgap, a large number of quasiparticles are created for single photon

hit events. This allows for high energy resolving power for each incident photon. In addition, LTD readout schemes can often be designed to bypass read noise, making these detectors ideal for observing faint sources.

One of the low temperature detector technologies listed above that has been proven to be particularly useful for ultraviolet, optical, and near-IR (UVOIR) astronomy is the MKID. MKIDs exploit a superconducting thin film's large kinetic inductance [22] to enable highly sensitive photon detection. When a photon hits the superconducting inductor in a MKID it breaks up a number of Cooper pairs proportional to the energy of the incident photon. The broken Cooper pairs temporarily generate a number of quasiparticles, and because there are now less charge carriers in the superconductor, the inductance is proportionally increased. By devising a scheme to quickly measure this inductance shift, one can extract the energy of the photon that caused the shift and the time of arrival of the photon.

MKIDs utilize superconducting LC resonators to measure these temporary increases in inductance. When a photon strikes the inductor portion of a resonator it raises its inductance. The resonant frequency of the resonator is analogously decreased, as the LC resonator frequency goes as $1/\sqrt{LC}$. In order to read out the resonator it is coupled capacitively to a microwave transmission line and probe tones are sent through the line to continuously drive the resonator and monitor any frequency shifts due to photon absorption events. MKIDs are naturally multiplexed by coupling many resonators to the same microwave transmission line and using a digital readout system [23]. This readout sends a comb of probe tones through the transmission line at the resonant frequencies of all the resonators on that line. The same digital readout system can be used to simultaneously monitor any photon events on these resonators. We currently read out two thousand resonators with a single microwave transmission line [24]. The architecture of the readout electronics make it easier to monitor the phase shift response at the probe

tone frequencies rather than to track the shifting resonator frequencies. The energy of the photon is linearly proportional to the change in phase, but begins to become nonlinear when the phase shift signal approaches half a resonator line width, causing a degradation of energy resolution for these high photon energies. The sensitivity of the detectors, defined as the phase shift for a given photon energy, needs to be carefully designed so that photon energies detected by the instrument stay mainly within the linear regime.

MKIDs have found broad use as power detectors in submillimeter astronomy. Some examples of submillimeter MKID instruments include the Multicolor Submillimeter Inductance Camera (MUSIC [26]) and more recently the New IRAM KID Array 2 (NIKA2 [29]).

The first astronomical UVOIR MKID instrument, initially fielded at the Palomar 200" telescope in 2011, was the Array Camera for Optical to Near-IR Spectrophotometry (ARCONS [35]). ARCONS contained a 2024 resonator MKID array with substoichiometric titanium nitride as the resonator material [36]. The resonators were split between two coplanar waveguide (CPW) transmission lines, and the arrays were read out using eight Reconfigurable Open Architecture Computing Hardware (ROACH [27]) digital electronic boards. Resonators were spaced roughly 2 MHz with gaps every 253 resonators to distinguish between resonator groups read out by different ROACH boards. The resonators were designed to fit in a microwave readout range of 3–6 GHz. The array was optimized for detection of photons between 380–1150 nm, with a maximum quantum efficiency of $\sim$17%. The spectral resolution, $\lambda/\Delta\lambda$, was 8 at 400 nm.

Although ARCONS was a technological breakthrough for UVOIR MKIDs, there were a number of detector issues that needed to be addressed before the technology could be used for the next generation of astronomical instrumentation. The main issue was the non-uniformity in composition in the substoichiometric TiN, which led to resonators appearing away from their designed resonant frequencies. This caused resonator collisions in frequency space, rendering many resonators unusable by the read out and lowering the

overall usable detector yield to ∼70%.

Another significant issue was related to the stability of pixels in the array. When ARCONS was illuminated with photons below the bandgap of silicon (∼1 μm) pixels were occasionally observed to exhibit a temporary (timescale of seconds to minutes) telegraph noise in the phase direction that mimicked incident photons at a very high count rate [51]. We believe that this was due to free electrons in the silicon substrate interacting with the electromagnetic field of the resonator. Using a non-semiconducting substrate like sapphire has been shown to eliminate this effect.

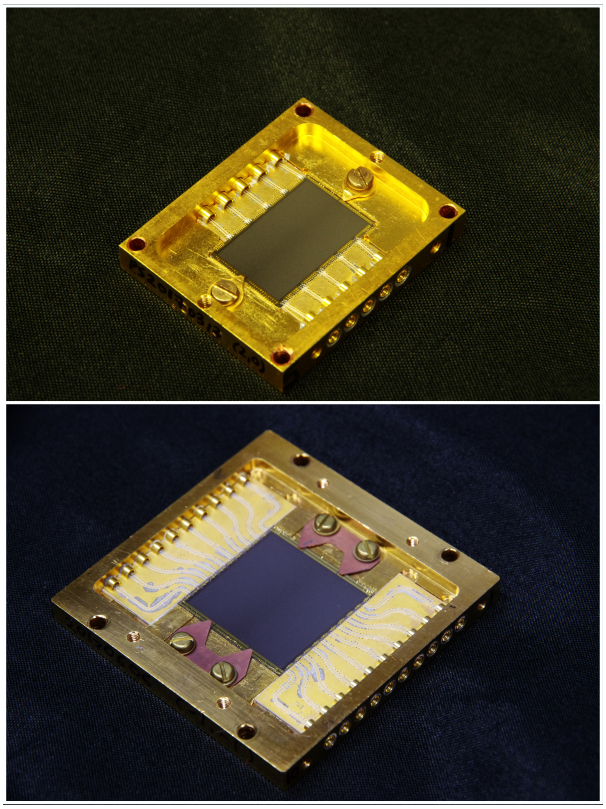

Figure 5.1: DARKNESS (top) and MEC (bottom) arrays after they have been mounted in their sample boxes and wire bond connections have been made.

Here we present our work in addressing these issues and developing large-format arrays for two upcoming MKID instruments designed for the direct imaging of exoplanets [40]. The first is the Dark-speckle Near-IR Energy-resolved Superconducting Spectrophotome-

ter (DARKNESS). This instrument has already been commissioned at Palomar Observatory, but detector improvements continue to be made and arrays can easily be swapped between observing runs. The second of these instruments is the MKID Exoplanet Camera (MEC), which is planned to be commissioned by the end of 2017 on the Subaru Telescope. Images of MKID arrays used in the DARKNESS and MEC instruments are shown in Figure 5.1.

5.2.2 Design

Large-format MKID arrays designed for various instruments share many common structures. These structures include superconducting LC resonators, transmission lines, a ground plane, and bond pads. The superconducting resonators act as the photon detectors. The transmission lines, which are usually made with coplanar waveguides (CPW) or microstrips, are used to drive and read out resonators and a single ground plane provides a common ground potential for the array. Superconducting bond pads are used to connect the transmission lines to the device, and gold bond pads are used to remove excess heat from the chip to the device box. We typically make our device boxes out of gold-plated oxygen-free copper.

Superconducting Resonators

The most critical structures in the MKID array design are the superconducting resonators. A superconducting resonator consists of a meandered inductor that acts as the photosensor and an interdigitated capacitor with legs of variable lengths to adjust the frequency. There are a number of design constraints that limit the choice of material and geometry of the resonators, and a summary of important resonator parameters is shown in Table 5.1. The critical temperature (T_C) should be kept as low as possible in

Table 5.1: DARKNESS and MEC Resonator Design Parameters

Common Material Properties		
Resonator Material	PtSi	
Superconducting Critical Temperature	900 mK	
Film Thickness	50 nm	
Surface Inductance	10.5 pH/□	
Other Design Parameters	**DARKNESS**	**MEC**
Inductor Width × Height	47 μm × 32 μm	47 μm × 35 μm
Average Inductor Leg Width	1.7 μm	1.7 μm
Inductor Slot Width	0.3 μm	0.5 μm
Interdigitated Capacitor Width × Height	121 μm × 92 μm	125 μm × 92 μm
Interdigitated Capacitor Leg Width	1 μm	1 μm
Interdigitated Capacitor Slot Width	1 μm	1 μm
Frequency Band	4.0 – 8.2 GHz	3.8 – 8.0 GHz
Average Coupling Quality Factor	30,000	30,000

order to maximize the sensitivity of the detectors and reduce background noise level. The operating temperature of the refrigerator, however, also provides a lower limit on the T_C. Our current adiabatic demagnetization refrigerators (ADRs) are required to hold their temperature for an entire night of astronomical observations, limiting the operating temperature to ∼100 mK. We have found that the resonator performance saturates around operating temperatures of $T_C/8$, requiring us to choose materials with a T_C at or above 800 mK. Superconducting films with a T_C between 0.8–1 K are ideal for astronomical UVOIR MKID instruments based on ADRs.

Another important resonator parameter is the internal quality factor (Q_i). This is essentially a measure of the any losses in the superconducting resonator. Q_i values of good resonators are typically $> 10^5$, but values of over 10^6 have been produced in TiN [36]. High values of Q_i appear to be correlated with better resonator performance due to higher maximum readout power and lower noise levels, which yield improved energy resolution. Another source of power loss in the resonator is due to the coupling of the resonator to

the CPW transmission. This is measured through the coupling quality factor (Q_c), which is typically engineered to have a value of ∼30,000. The total resonator quality factor (Q_r) goes as $(1/Q_i + 1/Q_c)^{-1}$, so when Q_i is very high, $Q_r \approx Q_c$. The detector sensitivity is tuned assuming this condition, so having high Q_i on the majority of resonators is also important for sensitivity uniformity across the array.

The surface inductance of the superconducting film and inductor geometry also play an important role in designing the resonators. The fractional change in broken Cooper Pairs for a given photon energy scales with the total inductor volume, so this quantity needs to be carefully engineered to provide the optimal sensitivity for detecting photons within the energy band of interest. For a given resonator design this quantity can only be changed in fabrication through the thickness of the superconducting film, which is roughly inversely proportional to the surface inductance for thin films. We generally design the inductor volume and sheet impedance first, which sets the total amount of inductance within the resonator. The capacitance can then be designed to place the resonator at a desired frequency. The DARKNESS and MEC arrays are optimized to detect photons within the 700–1400 nm wavelength band. The inductor volume is tuned so that the most energetic photons in this wavelength span produce roughly 120° phase pulses, which is near the onset of nonlinearity.

For the DARKNESS and MEC arrays in this work we have decided to replace the TiN films that were used in the ARCONS arrays with platinum silicide. This material has many of the desired quantities listed above, such as a T_C of 900 mK and quality factors of up to 10^6, as was seen with single layer test devices [47]. This material also shows roughly an order of magnitude better uniformity than TiN, allowing for much more precise resonator frequency placement (designed for 2 MHz spacing) and therefore a higher usable detector yield. PtSi also has a higher quantum efficiency than TiN at the wavelengths of observation of DARKNESS and MEC. In making the switch from

PtSi to TiN, we also switched from using a silicon substrate to one made of sapphire. Although this was mainly done to get around a film growth issue that was lowering the Q_i of the PtSi films, the change was also expected to reduce hot pixel behavior due to the decreased number of long-lived free electrons in the semiconducting silicon substrate. It should also be noted that submillimeter MKID arrays could get around the uniformity issue by using aluminum [62], but this material is too reflective at UVOIR wavelengths and would severely lower quantum efficiency. Al also has a relatively low kinetic inductance fraction, which would reduce detector sensitivity.

Transmission Lines, Ground Plane, and Coupling Bars

The next set of structures that that are important for driving the resonators are the transmission lines, the ground plane, and the coupling bars. In our current large-format array design, these structures are all made out of superconducting niobium with a T_C of $\sim$9 K and surface inductance of $\sim$0.1 pH/$\square$. The transmission lines take a fairly standard CPW design, with a width of 7.5 μm and slot size of 1.5 μm. This is done to ensure that the CPW lines are closely impedance matched to 50 Ω across the microwave bandwidth used by the readout. These transmission lines wind across the array multiple times in order to couple power to each individual resonator. This causes the neighboring ground planes to become electrically disconnected at RF frequencies. In order to combine these various sections and form one cohesive ground plane, crossovers need to be incorporated into the fabrication process, as is discussed in Sections 5.2.3.B–D.

The coupling bars (capacitors) are used to couple power between the transmission lines and the resonators. These appear beneath the capacitor portion of each resonator and also require crossovers to go over the ground plane and reach the resonator from the transmission line. The lengths of these coupling bars are adjusted to the frequencies of the resonators to which they are coupling power. This is done to adjust the coupling strength

to the individual resonators and keep the Q_C at 30,000. This keeps the sensitivity and power handling more constant across the array.

Bond Pads

The final relevant structures in the large-format MKID array design are the bond pads. First, there are Nb bond pads at the ends of the Nb CPW transmission lines. These are a few hundred microns in length and width, and the slot size between the bond pads and the ground plane is increased to match the width to slot size ratio elsewhere in the transmission line. This allows for straightforward aluminum wire bonding to these bond pads while keeping the transmission line matched as closely to 50 Ω as possible. Wire bonds lengths are kept to a minimum to reduce reflections. There is also a set of gold bond pads covering the perimeter of the array. These are used to make gold bond wire connections from the box to the chip to remove heat from the array. Gold wire bonds only adhere to other gold surfaces, which is why gold necessary for these particular bond pads.

DARKNESS and MEC Design Variations

The DARKNESS and MEC arrays have very similar designs with the major difference being that the MEC array contain roughly twice the number of pixels of the DARKNESS array. The DARKNESS array has a total of 10,000 (125×80) pixels across 5 CPW transmission lines. Each transmission line drives a subarray of 2,000 (25×80) pixels that is read out using 2 ROACH2 digital electronics boards. These boards are the second version of the boards used for the ARCONS array and have improved bandwidth and resources [24]. A total of 10 ROACH2 boards are required to read out the entire DARKNESS array. The MEC array is designed for a total of 20,440 (140×146) pixels. These pixels are separated into 10 transmission lines and a total of 20 ROACH2 boards

are required to read out the entirety of the array. Each transmission line drives 2,044 (14×146) resonators in this case.

The MEC array also has some additional design improvements over the DARKNESS array. One particular improvement is increasing the spacing and varying the distance of the crossovers connecting various segments of the ground plane by arbitrary amounts. This was done to reduce the impact of standing waves in the CPW line and improve the transmission through the line. The inductors of the MEC array also have gaps of 500 nm rather than the 300 nm that were used in the DARKNESS design. The larger gaps ensured that the inductors would be etched completely during the final fabrication step without over-etching into other areas of the resonator. This was expected to reduce variations in frequency in the resonators and potentially raise Q_i. Additionally, the MEC fabrication mask included gaps around the coupling bars. This was done to re-etch the coupling bars in one of the final fabrication steps and ensure exact spacing between the coupling bar and the resonator and ground plane, giving better control of the Q_C. It also was done to eliminate any possible shorts between the coupling bars and the ground plane to increase feedline yield.

Finally, the MEC array resonator frequency simulations were redone to improve the precision of the 2 MHz resonator spacing across the 4 GHz bandwidth of the array. For the DARKNESS array, 15 resonators with different capacitor leg lengths were simulated, and the resulting resonant frequency versus leg length curve was fit to a 6th order polynomial. This fit was used to map resonant frequency to capacitor leg length for the final array design. During the MEC array design process, it became clear that 15 simulations did not adequately sample the leg shrink versus frequency curve, especially with the increased placement accuracy offered by the more uniform PtSi. To remedy this, a new set of simulations with 185 different capacitor leg lengths was used. A finer meshing setting was also used to improve simulation accuracy. Mapping leg length to resonant frequency

was done by linearly interpolating between these simulations. All simulations were done using Sonnet. The results of the new simulations are shown in Figure 5.2.

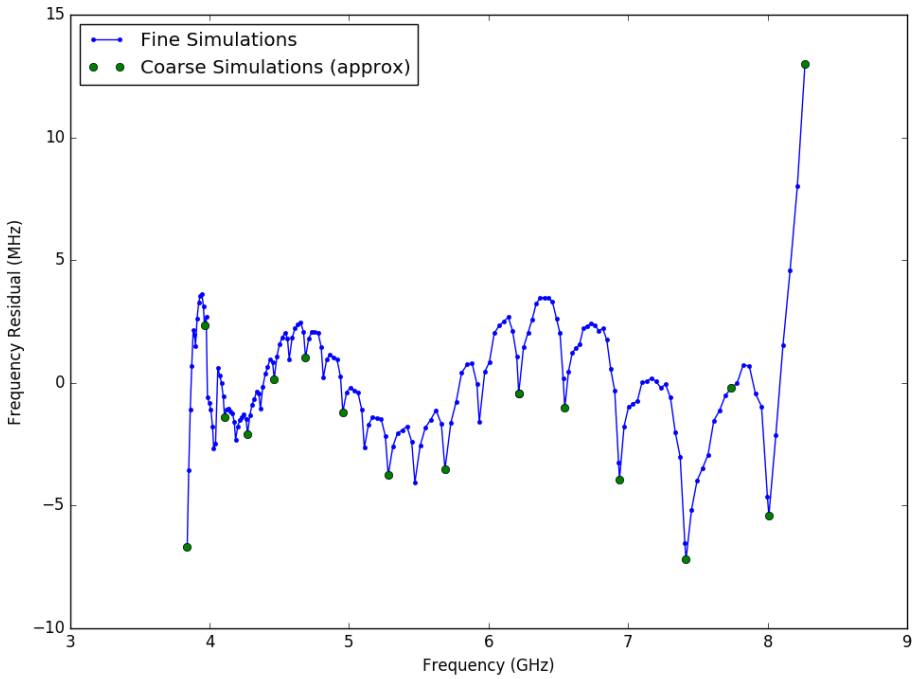

Figure 5.2: Resonators were simulated at 185 different capacitor leg lengths. The resulting frequency versus leg length curve was fit to a sixth order polynomial; the residuals of this fit as a function of frequency are shown in the plot above. A similar fit (with 15 simulations, shown approximately by the green points) was used to place frequencies on the DARKNESS array, resulting in errors of up to 15 MHz. In addition to the large scale sinusoidal feature not captured by the fit, most of the old simulations were done for total capacitor leg lengths where each leg was either fully extended or fully contracted (legs are varied one at a time to achieve a desired total leg length). The variation in the frequency versus leg length curve as an individual leg is grown/shrunk was not accounted for - these are the humps between the green points. For the MEC array design, capacitor leg length was mapped to frequency by interpolating between fine simulations (blue points).

5.2.3 Fabrication

The fabrication of the large-format PtSi MKID arrays in this work can be divided into six steps corresponding to the six lithographic layers in the design. MKID arrays of various sizes can be fabricated using identical processing steps, with the main difference being the photolithographic mask used to define the structures on the array. The fabrication of individual layers is described in detail below. Fabrication cross-sections are shown in Figure 5.3. Microscope images taken at each layer of the fabrication of a 10,000 pixel DARKNESS array are shown in Figure 5.4.

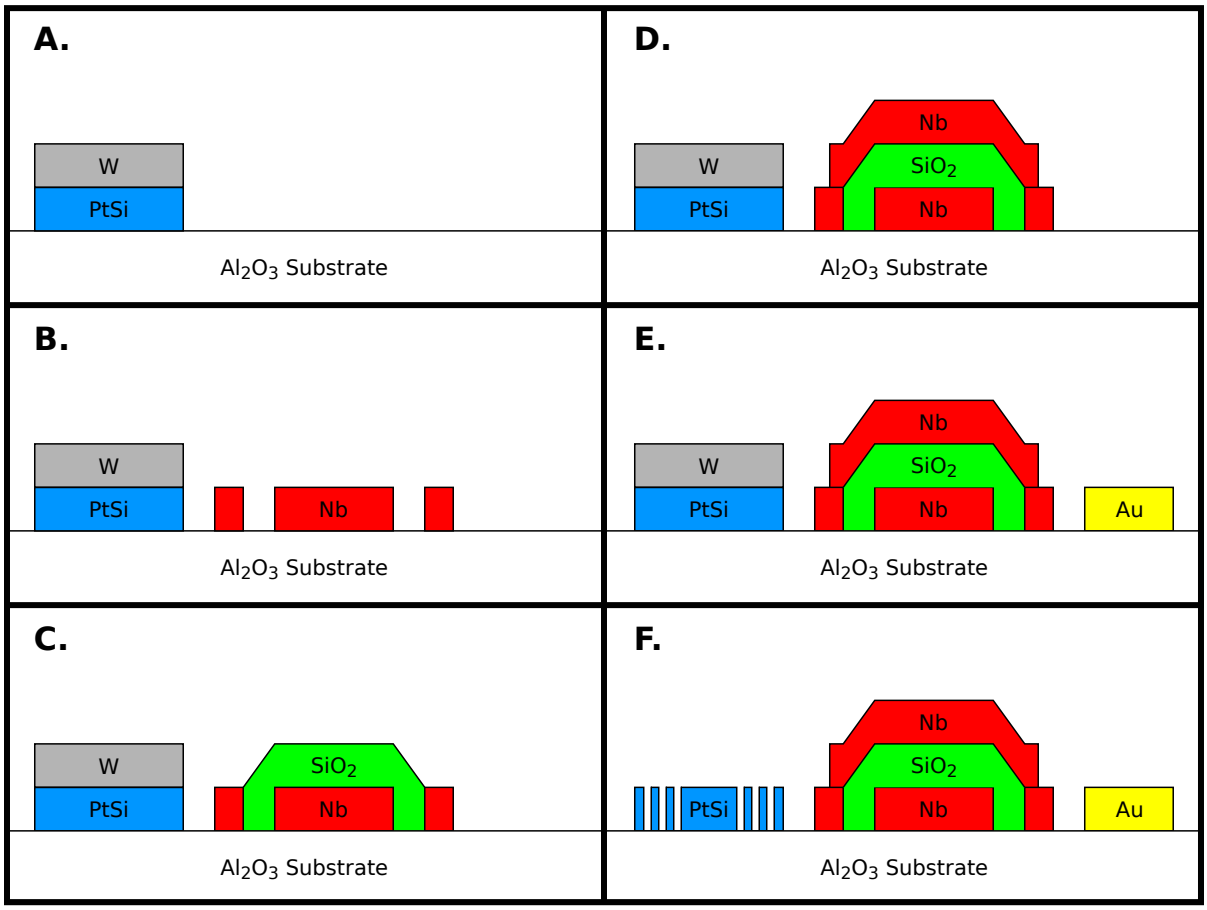

Figure 5.3: Fabrication cross-sections. A. Box outlines etch. B. Transmission lines and ground plane lift-off. C. Dielectric pads lift-off. D. Crossovers lift-off. E. Gold bond pads lift-off. F. Resonators etch.

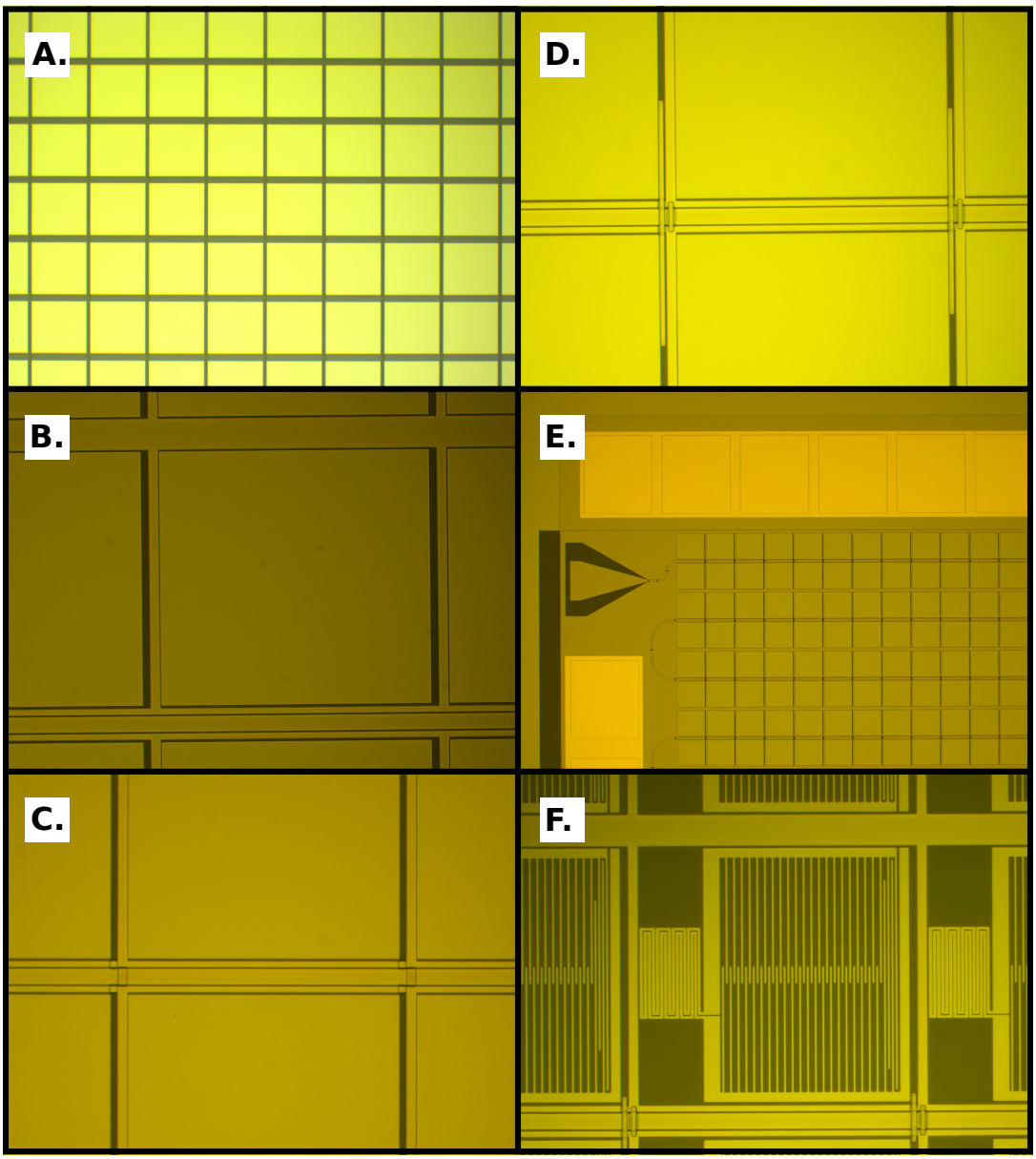

Figure 5.4: D3 microscope images at the end of each step. A. Box outlines etch. B. Transmission lines and ground plane lift-off. C. Dielectric pads lift-off. D. Crossovers lift-off. E. Gold bond pads lift-off. F. Resonators etch.

Box Outlines Etch

The first step in the large-format MKID array fabrication process is the deposition of the superconducting material that will be used for the sensor layer. To begin, a c-plane single crystal sapphire wafer is solvent cleaned and aggressively oxygen plasma cleaned using a Gasonics Aura 2000 plasma asher. In the current design, a ∼50 nm PtSi film is deposited on the sapphire substrate. The deposition is done in an AJA sputter system with a cryogenic pump, enabling the main chamber to reach a base pressures in the upper 10^{-10} Torr. A detailed description of the sputtered PtSi films used to make high internal quality factor MKIDs is given by Szypryt et al. 2016 [47]. In the case of large-format arrays a 100 nm tungsten film is deposited directly on top of the PtSi film in the same sputter system without breaking vacuum between the two depositions. This W film is used to protect the sensitive PtSi film from contamination and other fabrication issues until the final step.

After deposition, a dual layer of anti-reflective (AR) coating and positive deep UV photoresist is spun onto the PtSi film. A box outline layer is defined in the photoresist using an ASML 5500 deep UV stepper capable of performing 150 nm lithography. This deep UV stepper is used in all subsequent photolithography steps. AZ 300 MIF is used for development. After lithography and development, the PtSi+W film is etched using a Panasonic E640 inductively coupled plasma (ICP) etcher. First, the W is etched using SF6. Next, the PtSi is etched using a chemistry of 60% Ar, 20% CF_4, and 20% Cl_2. The remaining photoresist is removed with solvents and a moderate oxygen plasma.

The end result of this layer is shown in the microscope image in Figure 5.4.A. This step leaves boxes of PtSi in the areas that will ultimately contain the resonators. The areas that gets etched away will be used for the transmission line, ground plane, coupling bars, and bond pads, as described below.

Transmission Lines and Ground Plane Lift-off

The second layer in the fabrication process involves defining the coplanar waveguide transmission lines and ground plane segments in the areas where the PtSi got etched away in the previous step. To begin this step, a dual liftoff layer and positive photoresist are spun onto the wafer. The resist is exposed with the stepper and developed. To prevent liftoff artifacts, the wafer is run through a gentle oxygen plasma cleaning directly before the deposition.

Next, 90 nm of niobium is deposited using the same sputter system that was used for the PtSi deposition. The Nb is lifted off using n-methylpyrrolidone (NMP) and the wafer is cleaned for the next layer using solvents and a moderate oxygen plasma. At the completion of this layer, the Nb transmission lines and segments of ground plane will be defined on the wafer between boxes of PtSi, as shown in Figure 5.4.B. The next two layers are done to connect the various segments of these ground planes without shorting the transmission lines and to define capacitor structures that couple power from the transmission line to the detectors.

Dielectric Pads Lift-off

In the third fabrication layer, dielectric material is deposited and patterned to form insulating pads to facilitate superconducting crossovers. Figure 5.4.C shows how these dielectric pads look on a DARKNESS device before the deposition of the crossovers. In this step, photoresist is spun onto the wafer and once again patterned using the stepper. A 180 nm SiO_2 film is deposited onto the wafer by reactively sputtering from a Si target in an O_2 atmosphere. To do this, a different AJA sputter system with oxygen access, but higher base pressure, is used. The SiO2 is lifted off using NMP and the wafer is once again cleaned to prepare it for the crossover layer.

More recently, amorphous silicon (a-Si) has been used in place of SiO_2 for this dielectric layer due to its low expected loss tangent [66, 67]. Here, a 180 nm thick a-Si film is deposited onto the wafer with plasma-enhanced chemical vapor deposition (PECVD) in a SiH_4 and Ar atmosphere. This is done with a UNAXIS VLR system, which performs the PECVD at higher gas densities than traditional PECVD systems. This results in a dense, high quality film with especially low dielectric loss tangent.

Crossovers Lift-off

The next layer in the fabrication process is the deposition and patterning of niobium strips over the dielectric pads deposited in the previous layer. This is done to connect various segments of the ground plane over the transmission lines in order to create a single, contiguous ground plane. In addition, niobium bars are patterned below the capacitors of each resonator and are connected to the transmission line with a different set of crossovers. These bars are used to couple power from the transmission line to the resonators.

This layer is once again started with spinning and patterning of photoresist using the DUV stepper. Niobium is sputtered onto the wafer with the same conditions as were used for the ground plane deposition in the second layer, but the deposition is done longer to produce a 300 nm film. The increased thickness of this film is necessary to avoid step coverage issues at locations where the niobium slopes over the dielectric pads. After deposition, the niobium is lifted off in NMP and cleaned, defining the structures shown in Figure 5.4.D.

Gold Bond Pads Lift-off

In the final lift-off layer, gold is deposited and patterned into bond pads around the perimeter of the MKID array. Gold bond pads are necessary for thermally connecting

the array to the box via gold wire bonds, allowing heat to escape the chip. The gold bond pads from the corner of a DARKNESS array are shown in Figure 5.4.E.

A Temescal VES-2550 e-beam evaporator is used for the deposition. First, a 5 nm Ti layer is deposited as an adhesion promoter. Next, 200 nm of gold is deposited on top of the thin Ti layer. The Ti/Au stack is lifted off using NMP, and the wafer is cleaned in solvents and a moderate oxygen plasma in preparation for the next layer.

Resonators Etch

The last step involves patterning and etching the PtSi outlines into LC resonators. It also includes the removal of the sacrificial W layer that was deposited over the PtSi film at the start of the process. To begin, the wafer is once again patterned using the DUV stepper. The PtSi and W films are etched into resonators with the same etch chemistries that were used in the first layer. The PtSi in this layer is slightly over-etched in order to ensure complete etching in the small inductor gaps (300 nm gaps in the DARKNESS design). After etching, solvents and a moderate oxygen descum are used to remove the remaining photoresist.

Next, the wafer is prepared for dicing by spinning on a resist layer that protects the structures from impacts and contaminants. The wafer is diced using ADT 7100 dicing saw. After dicing, individual devices are solvent cleaned to remove the protective resist. Finally, the W is removed using H_2O_2 heated at 50°C. H_2O_2 was used because it selectively etches the W and has little to no affect on the other materials used in the process. Figure 5.4.F shows the result of this final etch and W removal process. This completes the fabrication process and at this point the devices can be mounted into boxes and wire bonded. A section of a completed DARKNESS array is shown in Figure 5.5.

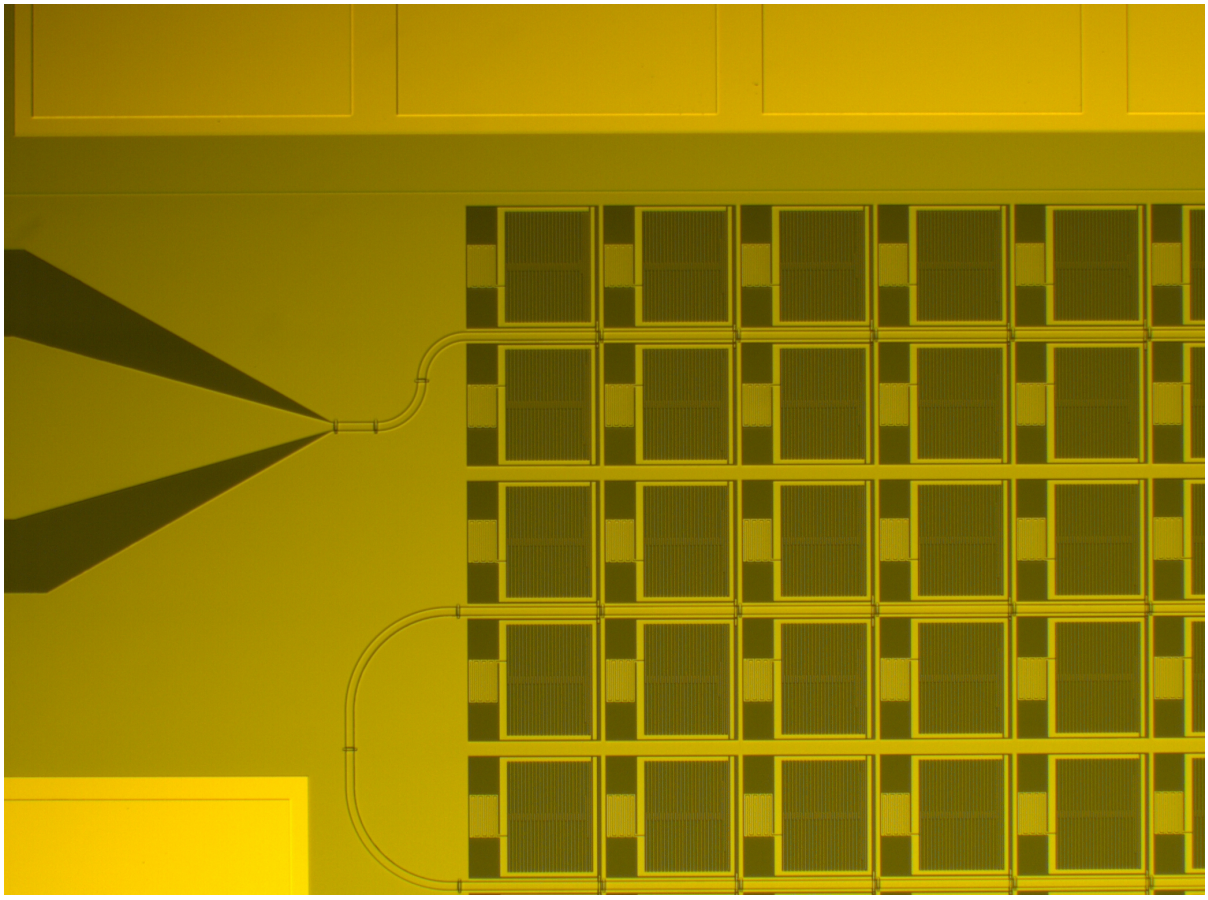

Figure 5.5: Microscope image of DARKNESS array at the end of fabrication.

5.2.4 Characterization

Upon completion of the fabrication process, a diced array is mounted in a gold-coated copper box using a set of clamps. At the base of this box, dark black Aktar tape is used to prevent reflections of photons that pass through the sensor layer and substrate. Superconducting aluminum wire bonds are used to connect the microwave transmission lines on the chip to those on the box. Gold wire bonds are added to thermally anchor the chip to the box and low temperature device stage. In order to cool the MKID arrays, a Bluefors dilution refrigerator with a base temperature of around 10 mK was used. For the majority of the measurements in this study, the temperature of the device stage was

controlled at 100 mK. The results of these measurements are described below.

Material Parameters

The T_C of the PtSi sensor layer was found by performing a DC resistance measuring during a fridge cooldown. Because the etched resonators are too small to wire up for a T_C test, an unused area of PtSi at the side of the wafer is used. The average T_C of the PtSi films was 930 mK, with slight variations from wafer to wafer. Overall, the spatial homogeneity in T_C was very good and similar to that seen in the single layer test devices [47].

The sheet inductance, L_S, of the PtSi films was determined by measuring the average shift in frequency and backing it out from the simulated frequency and L_S values. This was done using the proportionality relation, $L_{S,m} = L_{S,s} \times f_{0,m}/f_{0,s}$, where the m and s denote the measured and simulated values. Resonant frequencies are found by looking at complex transmission magnitude peaks with a vector network analyzer (VNA). The measured values of L_S in more recent wafers were fairly close to the design value of 10.5 pH/$\square$, with little to no average shift in frequency. This is due to the iterative manner in which the wafer L_S is tuned toward the correct value, with small changes in film thickness applied between successive wafers until the inductance is matched.

The W protect layer added an additional variable in tuning the T_C. We found that the addition of the protect layer tended to increase the sheet inductance of the final PtSi layer, even after the W was removed with H_2O_2. This may be attributed to a roughening of the PtSi surface caused by the W removal process. The PtSi film thickness was increased to make up for this effect.

Resonator Quality Factors

The next set of parameters, Q_i and Q_c, are calculated by sweeping the frequency space near a resonance and taking in-phase (I) and quadrature (Q) data with a VNA. Each resonator shows up as a loop on the I-Q plane, and this loop can be fit to a resonator model via the procedure given in Jiansong Gao's PhD thesis [46]. The Q_i and Q_c can be extracted from the fitted parameters.

The median Q_i of the best DARKNESS arrays was about 81,000. Figure 5.6 shows a histogram of Q_i values and a plot of the Q_i values versus frequency for this DARKNESS device. The best MEC arrays had improved Q_i, with median values of about 107,000. Figure 5.7 shows an analogous plot for the MEC array.

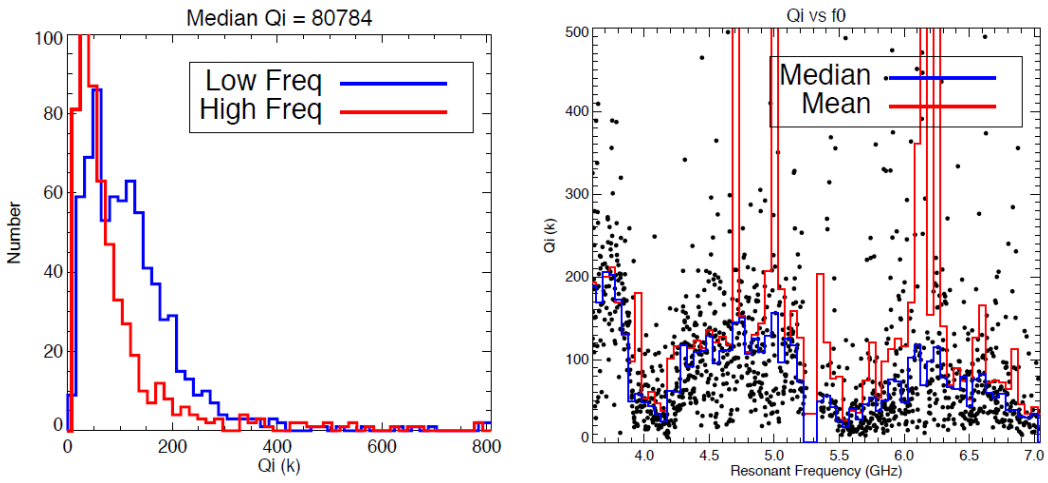

Figure 5.6: (Left) Histogram of Q_i values for the best performing DARKNESS device, split between the lower and upper halves of the total frequency space. (Right) Plot of Q_i versus frequency for the same device.

In terms of Q_c, the average value was 28,000 in the above DARKNESS array and 33,000 in the MEC array. These are both in fairly good agreement with the simulated Q_c of 30,000. Small deviations in Q_c such as these are typically not an issue as the readout can vary the amount of power supplied to individual resonators, making detector response more uniform.

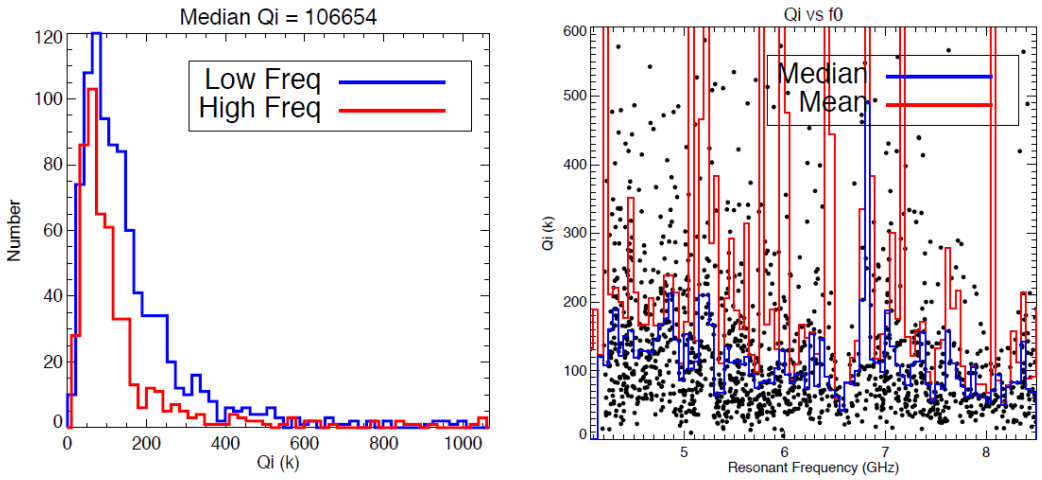

Figure 5.7: (Left) Histogram of Q_i values for the most recent MEC device, split between the lower and upper halves of the total frequency space. (Right) Plot of Q_i versus frequency for the same device.

Energy Resolution

The energy resolution is measured using an analog readout system. Here, three sharp laser lines of known wavelength are shined on the array. A histogram of phase shifts is measured, allowing us to correlate phase shifts to energy (or wavelength) across the wavelength band of the instrument. The histogram is fit to a model of Gaussian peaks, and the widths of the Gaussian peaks are extracted from the model fits. With proper normalization, the width of this Gaussian is proportional to the spread in detected energy. The spectral resolution, $R = \lambda/\Delta\lambda$, can then be calculated using this spread.

DARKNESS and MEC had fairly similar performance in terms of energy resolution. Both had an energy resolution of about 8 at 808 nm, with a declining energy resolution toward higher wavelengths. Figure 5.8 shows a histogram of photon wavelengths (already calibrated from phase shift) for a typical resonator in a large-format PtSi MKID array. The energy resolution at each laser peak is also included in the figure.

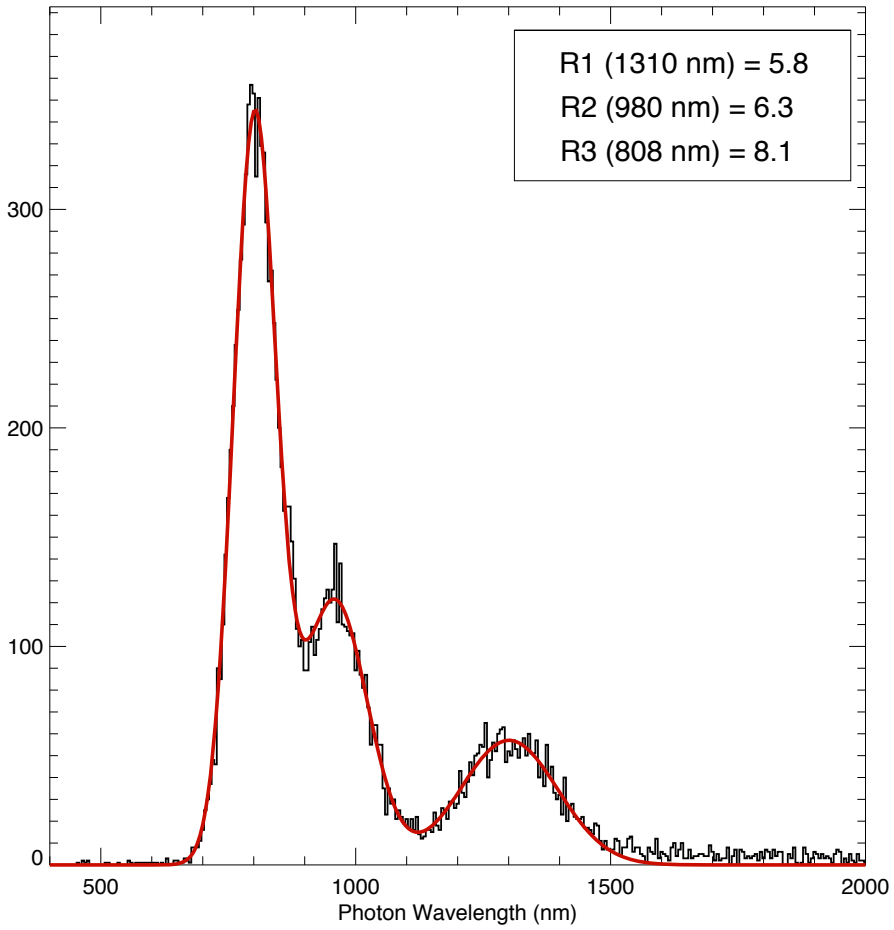

Figure 5.8: Histogram of photon wavelengths measured using three laser peaks at 1310, 980, and 808 nm. The energy resolution in the area of these three peaks was 5.8, 6.3, and 8.1, respectively.

Yield

The yield is measured as the number of unique resonances that can be read out using the room temperature electronics. Resonators are considered overlapping if they are within 500 kHz of another resonator, and these are subtracted from the usable pixel count. The pixel yield is measured on a feedline by feedline basis and is taken as the fraction of good pixels out of the number of total pixels designed on the feedline.

The first DARKNESS arrays had pixel yields of only about 50%. This was attributed to the rolloff of Q_i at higher frequencies, making those resonators difficult to detect in

the readout. This number also reflects pixels that were removed due having low levels of photosensitivity. In the more recent MEC arrays with overall higher values of Q_i, the pixel yield is approaching 90%, after subtracting overlapping resonators. It should be noted that precise photosensitivity measurements for resonators on these arrays still need to be done, and this pixel count may be reduced.

5.2.5 Discussion

One of the most striking factors in these large-format PtSi arrays is the relatively low values of Q_i. The best values of Q_i in these arrays were measured in the recent MEC arrays and had values of around 10^5. In single layer PtSi test resonators, however, the measured Q_i values were on order 10^6. The difference was attributed to the added complexity of the large-format array process, but it was difficult to pinpoint the fabrication step(s) that was degrading Q_i.

One of the first methods used to improve Q_i was to add a layer over the PtSi film to protect it through the subsequent fabrication steps and then remove the protect layer as the very last step. For this method, tungsten was chosen as the protect layer because it could be deposited in-situ after the PtSi, preventing any possible oxidation or contamination of the PtSi surface. The W could also be selectively removed using heated H_2O_2 with minimal etching of the other materials used in the process. The addition of the W layer raised the Q_i of the resonators by a factor of about two, but this was still too low, causing losses in energy resolution and pixel yield, especially at high frequencies.

The final resonator etching was also examined as a possible source of Q_i degradation. In the DARKNESS design, the inductor slots were only 300 nm wide, causing them to be etched more slowly than other areas of the resonator. To ensure a complete etching, the total etching time was increased, but this also caused a slight over-etch into the sapphire

in the area of the capacitor legs. The outcome was an increase in Q_i to the levels seen in the best DARKNESS array (∼80,000). To further ensure a complete etching in the MEC design, the inductor slot widths were increased to 500 nm. As was mentioned earlier, the Q_i in the most recent MEC arrays was ∼110,000, a considerable improvement from the best DARKNESS arrays. The Q_i is still far lower than the values observed in the single layer test mask and other sources of degradation are being explored.

The performance of the feedline and crossovers was also investigated. As can be seen in Figure 5.6, there were significant dips in Q_i near 4 and 5.5 GHz. This was attributed to possible transmission line or box standing wave modes not necessarily related to the quality of the resonators. For this reason, high loss microwave absorbers were added to the perimeter of the box to prevent any possible box modes. This did not have any significant effect on the Q_i of the resonators. In the MEC design, the feedline crossovers connecting the ground plane segments were spaced apart by an arbitrary amount rather than the fixed 150 μm spacing used in the DARKNESS design. This seemed to significantly reduce standing waves in the transmission line, and the MEC devices did not have these frequency dependent dips in Q_i, as can be seen in Figure 5.7. Different dielectric materials with varying loss tangents underneath the crossovers were also tested. There were no significant variations in the overall transmission between using SiO_2 and amorphous silicon. Amorphous silicon was kept as the dielectric material for more recent wafers due to ease of fabrication.

In the most recent devices with $Q_i > 100,000$, the energy resolution seems to saturate at R∼8 at 808 nm. At this level, the Q_i does not seem to be the limiting factor for R, indicating the Q_i is getting near the level needed for saturated array performance. Currently, the main factors limiting the energy resolution are amplifier noise and two-level system noise [53]. These factors require a more significant development effort that is beyond the scope of this work.

5.2.6 Conclusion

We have fabricated large-format PtSi MKID arrays for the 10,000 pixel DARKNESS instrument and the 20,440 pixel MEC instrument. These resonators on these arrays have measured internal quality factors of up to around 10^5 and energy resolutions of 8 at 808 nm. The most recent arrays have pixel yields of up to around 90%, but additional testing needs to be done to confirm these numbers. Future work will go toward further increasing the internal quality factors of resonators through a more systematic, layer-by-layer testing procedure. Increases in the internal quality factor will lead to much improved pixel yield and slight improvements in energy resolution. These arrays have already been proven on the sky with the DARKNESS array at Palomar Observatory, and future observations with the improved MEC array at the Subaru Telescope will demonstrate the strengths of optical MKIDs for the direct imaging of exoplanets.

Acknowledgements

This work was supported by a NASA Space Technology Research Fellowship (NSTRF) and NASA grant NNX16AE98G. Fabrication of large-format PtSi MKID arrays was done in the UCSB Nanofabrication Facility. Some fabrication was also done at NASA JPL's Microdevices Laboratory (MDL).

Chapter 6

Applications in Astronomy

6.1 Background

Optical MKIDs have a variety of applications, most of which are in the field of astronomy. ARCONS was one of the first MKID instruments, and it was the first at any wavelength to produce scientific results from astronomical observations. Although ARCONS was a general purpose, seeing limited, low resolution instrument, it excelled at observing faint targets in which precise timing information and low-to-medium resolution spectroscopy are important. In particular, ARCONS was scientifically most productive at the observations of faint pulsars with rotation periods as low as a few milliseconds [37, 38] and compact objects with orbital periods as low as 10s of minutes [39]. ARCONS also observed a number of other types of objects, including supernovae and exoplanet transits.

MKIDs have a few chief advantages over the more traditional CCDs used in optical astronomy. As mentioned earlier, because MKIDs absorb photons directly in a superconductor with a much lower bandgap energy that that of silicon, MKIDs can detect lower energy photons. Also, CCDs typically cannot deal with ultraviolet photon energies

or higher due to multiple electrons being promoted to the conduction band. Combined, these two effects give optical MKID cameras a far superior dynamic range as compared to CCDs, as shown by ARCONS's 380–1150 nm wavelength range. In addition, the way MKIDs are read out prevents the sort of read noise and dark current behavior seen in CCDs. Finally, MKIDs are single photon counting detectors, reducing the amount of observing time needed to get to a certain SNR compared with integrated detectors such as CCDs. This also removes the requirement of CCDs to set an exposure time prior to observation.

6.2 MKID Data Reduction Pipeline

Because optical MKID data is very different than that produced from a CCD, an entirely new MKID data reduction pipeline had to be written from scratch [51]. The pipeline included modules for cosmic ray cleaning, bad pixel detection, wavelength calibration, flatfield calibration and other routines. Cosmic ray cleaning would essentially mask out photon events that occurred at multiple pixels simultaneously. The bad pixel detection module would check the array for dead pixels or those that were mostly not-photosensitive and eliminate them from the analysis. In addition, it would correct pixels that would temporarily display hot pixel behavior by comparing them to neighboring pixels. The wavelength calibration would calculate the phase shift response for individual resonators based off of a laser calibration system with precisely known energies. Finally, the flatfield correction would normalize the photometric response of the resonators based on observations of a background source expected to be flat in count rate.

As an example of the capabilities of ARCONS and the MKID data reduction pipeline, I will be presenting a paper detailing observations and analysis of AM CVn object SDSS J0926+3624 in the following section. This was based off of observations done at the Hale

200" Telescope at Palomar Observatory in December 2012. The object was analyzed using an early version of the data reduction pipeline, and many of the pipeline's more sophisticated features were still under development at the time.

6.3 Direct Detection of SDSS J0926+3624 Orbital Expansion with ARCONS

Abstract

AM Canum Venaticorum (AM CVn) stars belong to a class of ultra-compact, short period binaries with spectra dominated largely by helium. SDSS J0926+3624 is of particular interest as it is the first observed eclipsing AM CVn system. We observed SDSS J0926+3624 with the **Ar**ray **C**amera for **O**ptical to **N**ear-IR **S**pectrophotometry (ARCONS) at the Palomar 200" telescope. ARCONS uses a relatively new type of energy-resolved photon counters called Microwave Kinetic Inductance Detectors (MKIDs). ARCONS, sensitive to radiation from 380 to 1150 nm, has a time resolution of several microseconds and can measure the energy of a photon to ∼10%. We present the light curves for these observations and examine changes in orbital period from prior observations. Using a quadratic ephemeris model, we measure a period rate of change $\dot{P} = (3.07 \pm 0.56) \times 10^{-13}$. In addition, we use the high timing resolution of ARCONS to examine the system's high frequency variations and search for possible quasi-periodic oscillations (QPOs). Finally, we use the instrument's spectral resolution to examine the light curves in various wavelength bands. We do not find any high frequency QPOs or significant spectral variability throughout an eclipse.

6.3.1 Introduction

The AM Canum Venaticorum (AM CVn) stars define a class of short-period binary stars with spectra dominated largely by helium. They consist of a white dwarf primary accreting helium-rich matter from a less massive secondary, typically through an accretion disk. They appear as variable, faint blue stars. The earliest review of AM CVn systems is given by Ref. [68]. More recent reviews are given by Ref. [69], [70], and [71].

AM CVn systems are believed to start as detached binaries. After one or more common envelope events, they are brought closer together due to gravitational wave driven angular momentum loss[72]. At this point, Roche-lobe overflow (RLOF) may lead to the formation of an AM CVn star. If gravitational wave radiation is the dominant phenomenon in the AM CVn evolution, the orbital period of the binary will decrease. On the other hand, if mass transfer due to RLOF dominates the evolution, the period will hit a minimum before beginning to increase [71]. Due to their short periods, AM CVn stars are predicted to be some of the strongest sources of gravitational wave radiation. For this reason, AM CVn stars will be among the first objects studied by proposed gravitational wave missions such as LISA [73].

There are three possible scenarios for the formation of an AM CVn system, each of which contains an accreting white dwarf primary and a helium-rich donor. The first scenario involves a double white dwarf system which loses angular momentum due to gravitational wave radiation, decreasing the orbital period. When the orbit becomes close enough, the lower mass, helium-rich donor white dwarf begins to transfer mass through stable RLOF, causing the period to increase. The mass transfer rate drops at this stage [74]. In the second case, the donor star is a low-mass non-degenerate helium star. Much like in the white dwarf donor channel, after the period passes through a minimum, it begins to increase while the mass transfer rate decreases [75]. In the third

and least likely case, the system forms as a regular cataclysmic variable (CV) with a highly evolved secondary star. After the secondary star transfers away much of its hydrogen to reveal its helium core, it follows a path similar to the non-degenerate helium star channel [76].

The prototype AM CVn star was initially discovered as a blue star by Ref. [77]. AM CVn was later found to be variable on very low levels by Ref. [78]. Soon after, Ref. [74] explained this system as a binary whose evolutionary physics is determined by gravitational wave radiation and saw this as a testing ground for general relativity. Since then, 36 new AM CVn systems have been found. The Sloan Digital Sky Survey (SDSS) and the Palomar Transient Factor (PTF) found the majority of these systems (see Table 6.1 in Ref. [79]).

A particularly interesting system, SDSS J0926+3624, was discovered by Ref. [80]. It was the first eclipsing AM CVn system discovered, and only recently has a second partially eclipsing AM CVn system (PTF1 J1919+4815) been found [79]. SDSS J0926+3624 has an orbital period of 28.3 minutes, deep eclipses lasting $\sim$1.3 minutes, and a mean g'-band magnitude of $\sim$19. The magnitude is quite variable throughout the orbit due to superhumping, a phenomenon that is observed in the majority of AM CVn stars [71]. Superhumping is due to the large mass ratios causing tidal stress asymmetries. These asymmetries deform the originally circular disk into a precessing elliptical disk [81, 68].

The eclipsing nature of SDSS J0926+3624 is especially important in that it provides precise timing information. The eclipse timing information from observations spanning just a few years can be used to determine a period change caused by mass transfer and gravitational wave radiation. This can be used as a probe to study the physics of gravitational waves and check predictions of general relativity [71].

In 2012 we observed SDSS J0926+3624 with the **Ar**ray **C**amera for **O**ptical to **N**ear-IR **S**pectrophotometry (ARCONS; see Ref. [82, 35]). The goal of these observations was

to add to the 2006 and 2009 observations performed by Ref. [83, 84] and to use this large timespan of data to measure the orbital period change, $\dot{P}$. The use of ARCONS to make these observations also allowed us to probe new regions of parameter space. Using the microsecond time resolution of ARCONS, we searched for quasi-periodic oscillations (QPOs) in much higher frequency space than had previously been possible. QPOs have been observed in other variable sources such as CVs and X-ray binaries [85]. Finally, we used the instrument's photon energy resolution to examine the light curves of SDSS J0926+3624 in multiple bands from blue to infrared.

6.3.2 Instrument

ARCONS uses a new superconducting technology called Microwave Kinetic Inductance Detectors (MKIDs; see Ref. [20, 48]). MKIDS are nearly ideal photon sensors, capable of measuring the energy of a photon to within a few percent and the arrival time to a microsecond. There is no read noise or dark current. The array used during this particular observing run contains a total of 2024 (44x46) pixels. The plate scale is 0.45 arcseconds/pixel, making the field of view roughly 20x20 arcseconds. ARCONS is sensitive to photons in the 380-1150 nm range and has an energy resolution $E/\delta E = 8$ at 400 nm.

6.3.3 Data

SDSS J0926+3624 was observed at the Palomar 200" telescope over the course of three nights in December, 2012. Observations took place on the nights of December 8, 10, and 11. Seeing stayed between 1 –1.5" throughout the three nights of observation. The count rates began to rise toward the end of each night of observations due to the onset of twilight. A summarized log of the observations is shown in Table 6.1.

Table 6.1: Observation Log

Night	UTC Start	UTC End	Eclipses observed	Comments
Dec. 8, 2012	12:11	13:28	3	Seeing ∼1.5", short break for calibration
Dec. 10, 2012	07:44	09:01	2	Seeing 1 – 1.5", poor focus, data omitted
	12:02	13:23	3	Seeing ∼1.5", poor conditions
Dec. 11, 2012	11:27	13:33	5	Seeing 1 – 1.5", thin high clouds

Guiding was done using an SBIG STF-8300M CCD Camera, which has a field of view of ∼1.5 arcminutes. A guide star was tracked by using the camera in 3x3 binning mode with exposure times of 10-15 seconds, depending on observing conditions. Due to technical constraints on the cryogenic system, the instrument was mounted at Coudé focus. The resulting field rotation was taken into account in the guiding software.

After the observational data was read out, it was stored in HDF[1] files. From there, it was pushed through the ARCONS data reduction pipeline, as detailed in Ref. [35]. The pipeline steps used included dead pixel masking, cosmic ray cleaning, wavelength calibration and flatfield calibration.

Once the data went through these reduction steps, the photons were binned by wavelength and summed over a desired integration time. ARCONS continuously detects individual photons, eliminating the need for a traditional exposure time as in a CCD and allowing us to choose integration times during data processing that best fit the application. After the initial reduction, a circular two-dimensional Gaussian point spread function (PSF) was fit to each image, and the baseline of the fit was subtracted off, corresponding to removing the background sky level. The amplitude and width were used to find the flux from the object. The light curves from all three nights of observation using a 10s integration time are shown in Figure 6.1. In order to maximize the signal-to-noise ratio (SNR), only photons with wavelengths between 4000-5500 Å were used.

[1] http://www.hdfgroup.org/

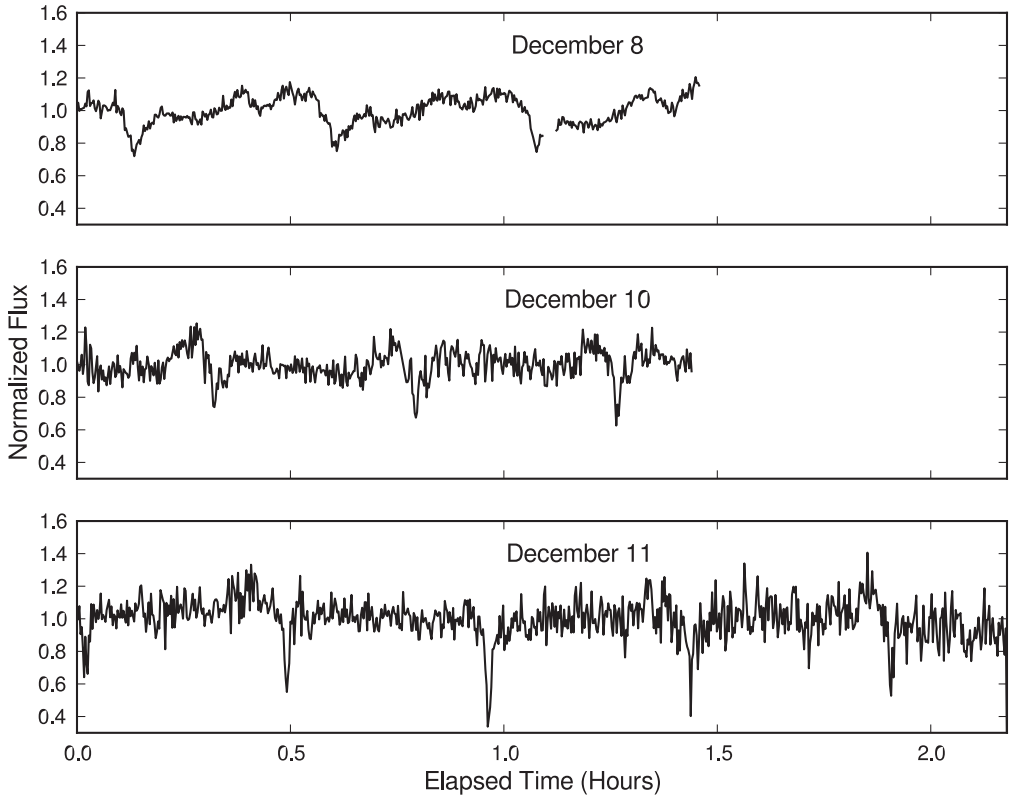

Figure 6.1: The light curves of SDSS J0926+3624 from December 8, 10, and 11. The integration time is set to 10s and only photons within the 4000-5500 Å range are used. The zero point in time marks the beginning of an observation during a particular night.

After the image stacks were created, we used the timing and PSF fit flux information from the light curves to perform phase dispersion minimization (PDM; see Ref. [86]). The results are shown in Figure 6.2. PDM was used over standard fast fourier transform (FFT) techniques due to the nonsinusoidal nature of our light curves on the observed timescale. Again, an integration time of 10s was used, and the selected photons were in the 4000-5500 Å range. In each night, the dip corresponding to the eclipse frequency of ∼50.9 cycles per day was clearly visible. The superhump frequency, which is expected to be slightly lower than the eclipse frequency [68], could not be distinguished from the eclipse frequency. The fact that our data did not reveal clear superhumping behavior could be due to a vertical extension of the bright spot [84]. Observing conditions were substantially worse on December 10 and 11, and this data was not used in our higher frequency analysis.

6.3.4 Results

Light Curve Analysis

The primary focus of our light curve analysis was to precisely determine the timings of eclipses. With this we could use data from prior observations made by Ref. [84] to better constrain the ephemeris. We started with the light curves shown in Figure 6.1, except we used an integration time of 3 seconds for the better quality December 8 data in order to calculate the eclipse timing more precisely. As the observing conditions were worse on December 10 and 11, it was more difficult to perform PSF fitting photometry and a 10 second integration time was required.

We fit the light curves to a model containing only the white dwarf eclipse using Levenberg-Marquardt minimization. This is a reasonable model as the bright spot component is completely distinct in time from the white dwarf component, and it varies from

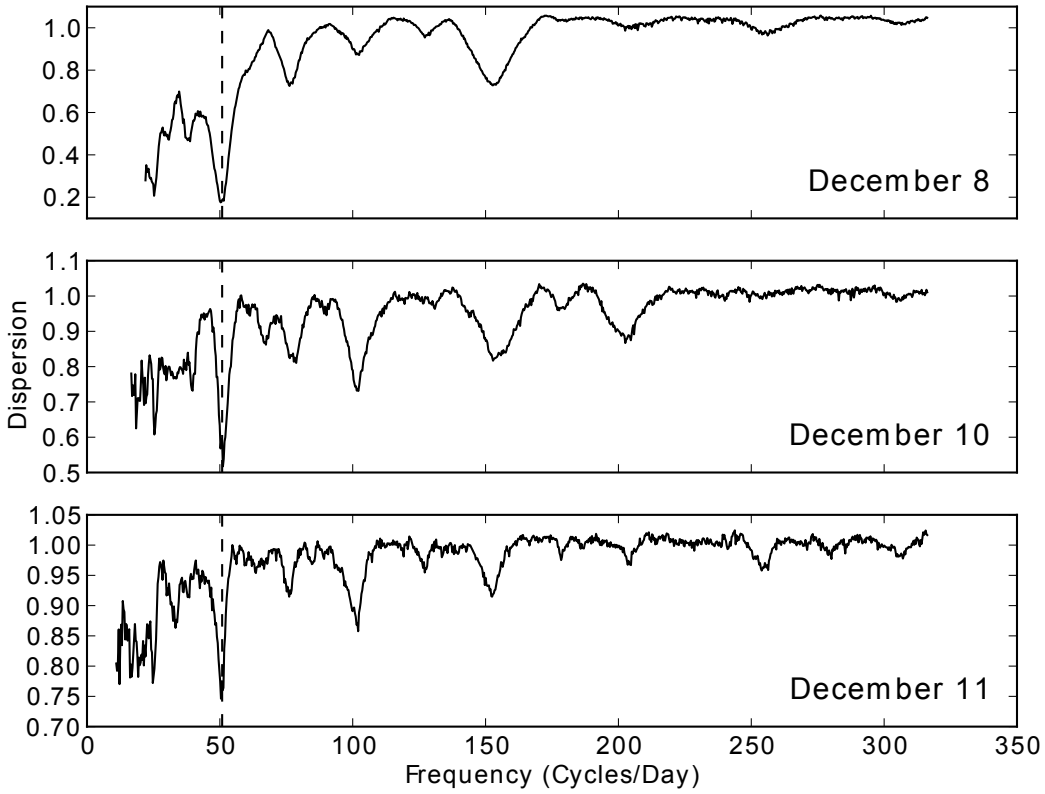

Figure 6.2: Phase dispersion minimization results for the December 8, 10, and 11 data. The dashed line marks the measured eclipse frequency of ∼50.9 cycles/day. There are clear dips in dispersion at the eclipse frequency and its harmonics for each night of observation. The first subharmonic at half the fundamental frequency is also visible, as well as multiples of this subharmonic. Lower frequency subharmonics and their multiples are seen in the December 10 and 11 data, which had longer time baselines than the December 8 data.

eclipse to eclipse. We modeled the white dwarf eclipse as a limb-darkened sphere, using a square root limb-darkening law [87]. This law has the form

$$\frac{I(\mu)}{I(1)} = 1 - a_1(1 - \sqrt{\mu}) - a_2(1 - \mu), \tag{6.1}$$

where $\mu = \cos\gamma$, and γ is the angle between the line of sight and the emergent radiation. The constants a_1 and a_2 were determined by fitting individual eclipses. We used this model to fit a time to the center of each observed eclipse. An example of the model fit for the first eclipse observed in the December 8 data is shown in Figure 6.3.

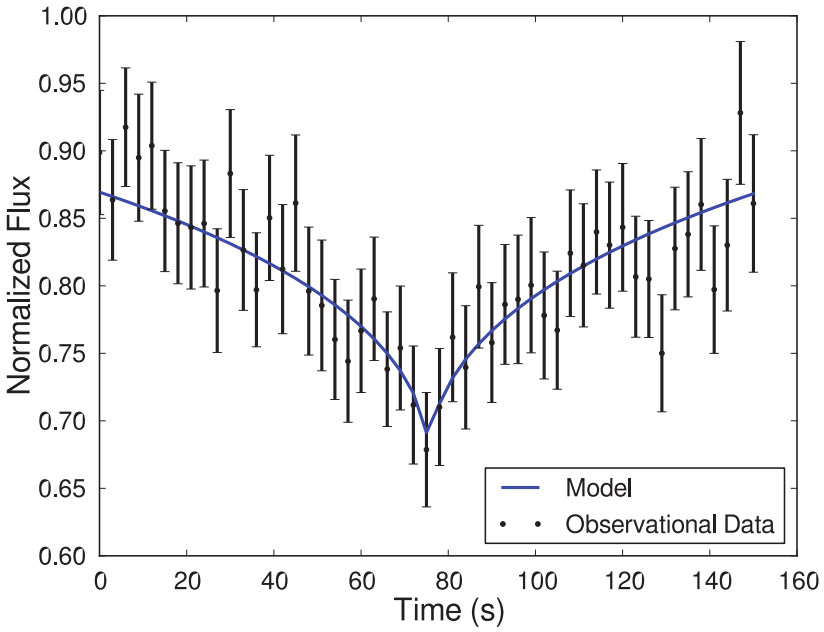

Figure 6.3: Example of the model and fit used to determine the eclipse centers. Error bars in flux are calculated using the PSF fitting errors. This particular fit shows the first eclipse from the December 8 data.

Timing errors for the eclipse fits for each epoch (2006, 2009, 2012) are determined by taking all the data points from that epoch, fitting and subtracting a locally determined linear ephemeris, and then taking the standard deviation of these residuals. This

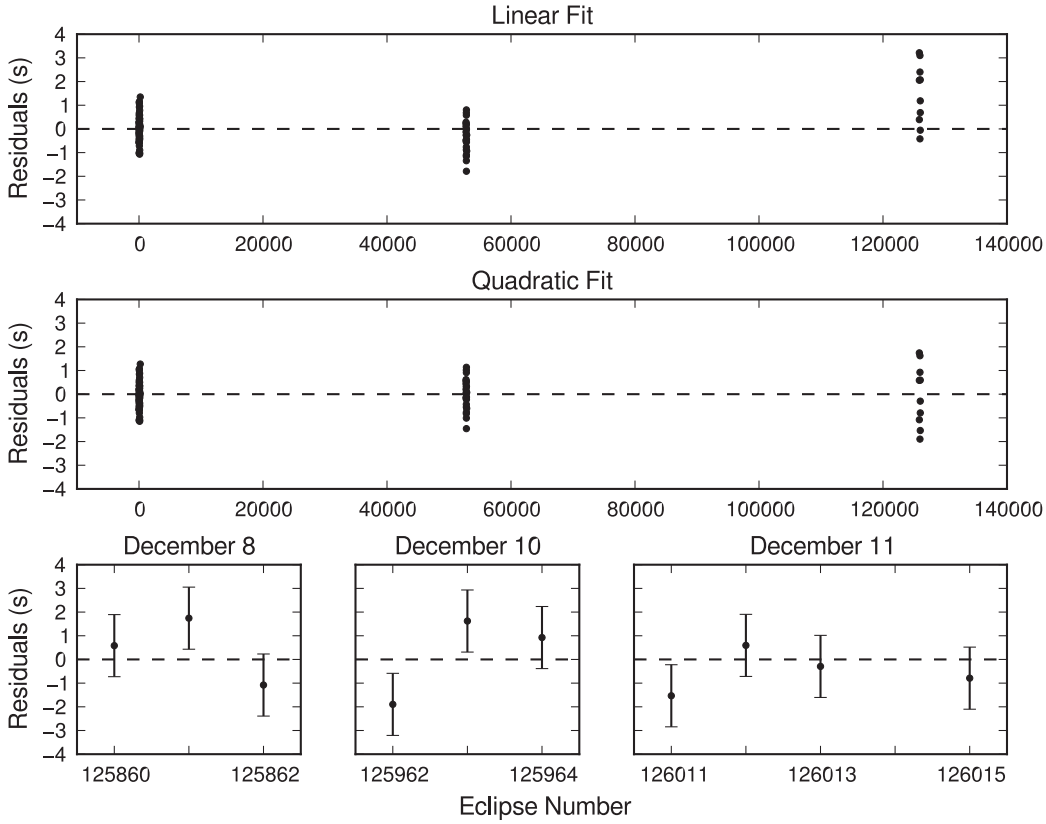

Figure 6.4: (Top) Residuals of the linear fit ephemeris for 2006 and 2009 data published in Ref. [84] and the 2012 ARCONS observations. (Middle) Residuals of the quadratic fit ephemeris, for the same data sets. (Bottom) Plot of the residuals of the quadratic fit ephemeris for the ARCONS data only.

approach appears to be more robust than propagating the photometric errors through the eclipse fitting model as there is some intrinsic variation in the eclipse timing due to flickering in the accretion disk [84].

We then combined the eclipse timings calculated from our simple model fit with previous results from Ref. [84] to fit a new ephemeris. Again, we used the Levenberg-Marquardt method to determine the fits. There were two models that we used to fit the ephemeris: a linear model with a constant period and a quadratic model with a $\dot{P}$ component. We Taylor expanded the eclipse number in terms of the eclipse time in the form $N = N_0 + \nu(t - t_0)$, where N is the eclipse number, t is the Barycentric Dynamical Time (TDB), in Modified Julian Days (MJD), and ν is the eclipse frequency. N_0 is the fit eclipse number of our first eclipse measured at $t_0 = 56270.513365$ days. We found that the linear ephemeris followed the relation

$$N = 125860.0012 + \frac{50.86140661}{days}(t - t_0). \tag{6.2}$$

The measured period with this model is $0.01966127299 \pm 3.0\times10^{-11}$ days.

In the qudratic ephemeris model, we added the second order term $\frac{1}{2}\dot{\nu}(t - t_0)^2$, where $\dot{\nu}$ is the frequency time derivative. The quadratic ephemeris followed the relation

$$N = 125860.0003 + \frac{50.86140529}{days}(t - t_0) - \frac{1}{2} \times \frac{7.95 \times 10^{-10}}{days^2}(t - t_0)^2. \tag{6.3}$$

With this model, the measured period at the time of our first eclipse is 0.01966127350 $\pm$ 9.7$\times10^{-11}$ days. The measured period derivative term, $\dot{P}$, is $(3.07 \pm 0.56) \times 10^{-13}$. This is in range of the anticipated period change of $\dot{P} \sim 3 \times 10^{-13}$ given by Ref. [80]. From our measured $\dot{P}$ and the primary and donor mass values given by Ref. [84], we predict a conservative mass transfer rate, accounting for angular momentum loss from

gravitational wave radiation, of $\sim 1.8 \times 10^{-10} M_{\odot}$/yr. This transfer rate is reasonable for AM CVn systems along either the white dwarf or helium star donor formation paths, as shown in Figure 1 of Ref. [69].

Plots showing the residuals of the linear and quadratic fits for all of the data as well as more detailed plots of the residuals for only the recently taken data are shown in Figure 6.4. In the December 11 data, eclipse number 126014 was omitted. Data quality was poor during this time (as can be seen in the bottom panel of Figure 6.1, 4th eclipse), and the eclipse time could not be measured accurately.

We tested the likelihood of a quadratic ephemeris as opposed to a linear ephemeris. To do this, we measured the goodness of fits by calculating the reduced χ^2 values for both models. The linear fit had a χ^2 value of 1.24, whereas the quadratic fit had a χ^2 value of 1.01. This shows that the quadratic model fits the observational data much better than the linear model. With this we claim a detection of $\dot{P}$ at 5.4 σ.

Quasi-periodic Oscillation Search

We used the microsecond timing resolution of ARCONS to look for quasi-periodic oscillations (QPOs) in a large frequency range. We first looked at a low-intermediate frequency range ($10^{2.5}$ – $10^{3.5}$ cycles/day). To do this, we used a method similar to the one used to create the low frequency phase dispersion plots seen in Figure 6.2. This involved PSF fitting images that have been integrated for 1s. We then performed PDM using the image times and the flux calculated from the fit parameters. A $10^{2.5}$ – $10^{3.5}$ cycles/day phase dispersion plot of the December 8 data is shown in Figure 6.5. This method was used for frequencies of up to ∼1 Hz, as higher sampling rates made fitting a PSF increasingly more difficult. No evidence of a QPO was found in this range, including the possible QPO seen at ∼1700 cycles/day in the 2006 data of Ref. [84]. It is worth noting that this QPO signal was not seen in their 2009 data.

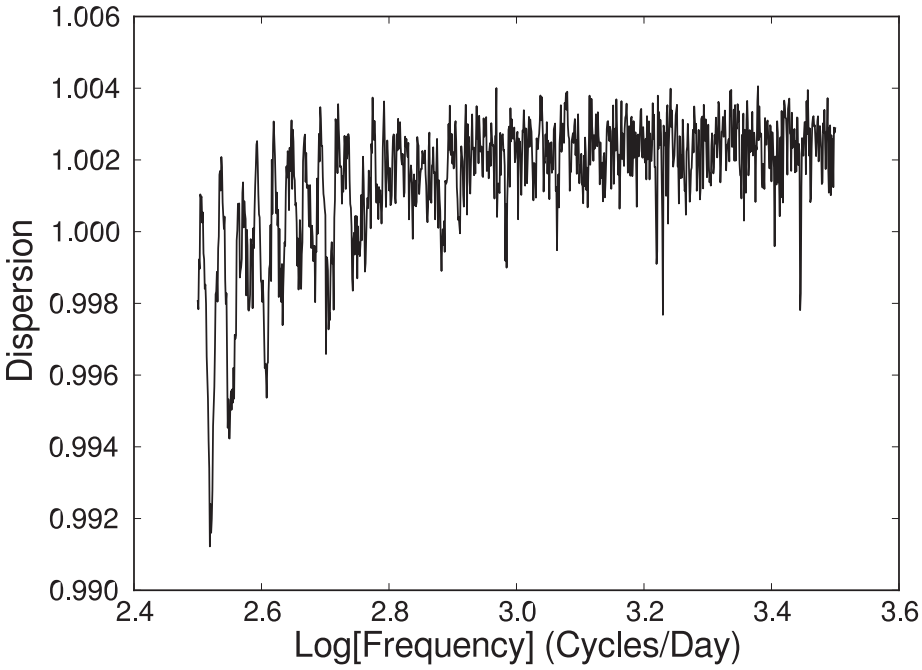

Figure 6.5: Phase dispersion measures of the December 8 data in an intermediate frequency range. The possible QPO observed in the 2006 data by Ref. [84] was not seen in our data.

We also performed PDM in the $\geq$1 Hz range. For these higher frequency calculations, we used standard aperture photometry to retrieve photon timestamps to a precision of $\sim$10μs. PSF fitting fails at such small timescales. The photons were binned together to form count per 500μs intervals. These count rates were then used to perform PDM in blocks of 1s, and the dispersion measures were averaged together to obtain a single dispersion plot. The high frequency ($1 - 10^3$ Hz) phase dispersion plot for the December 8 data is shown in Figure 6.6. There was also no evidence of a QPO signal at these high frequencies.

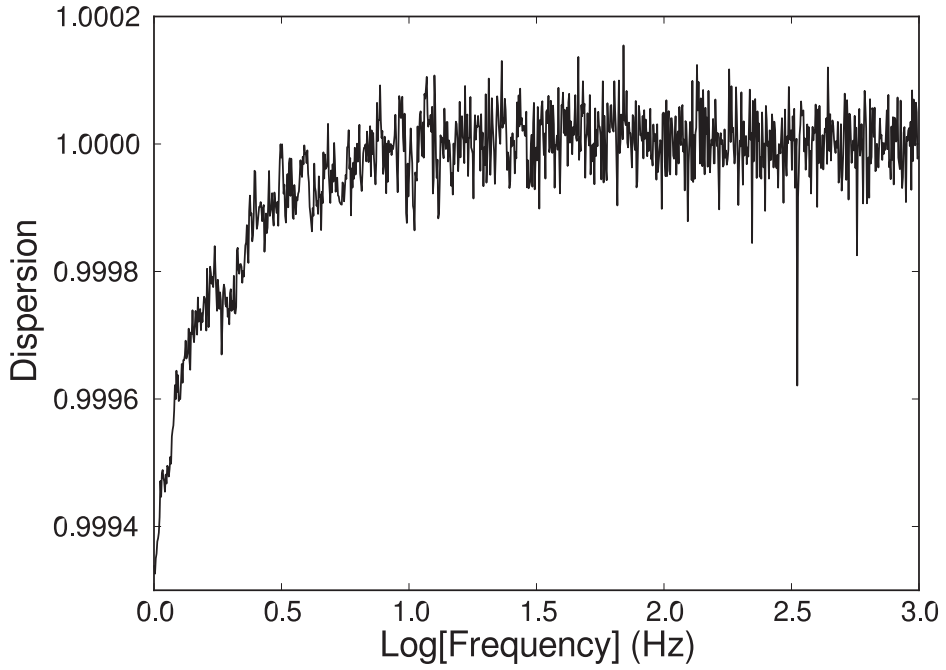

Figure 6.6: Average of many high frequency ($\geq$1 Hz) phase dispersion measures taken of December 8 data. No high frequency QPOs were visible.

Spectral Variability

We examine the variability of SDSS J0926+3624 during various phases of the orbit between four wavelength bands: 4000-5500 Å, 5500-7000 Å, 7000-8500 Å, and 8500-10000 Å. To do this, we determine the wavelength of an individual photon and place the photon into a corresponding wavelength bin. Finding a PSF fit for the lower energy photons was difficult because the brightness of SDSS J0926+3624 is comparable to the sky background at these energies. Therefore, we used standard aperture photometry in each of the four wavelength bins.

In Figure 6.7, we plot the resulting light curves for the December 8 data. As expected, the blue (4000-5500 Å) and green (5500-7000 Å) bands received much higher count rates

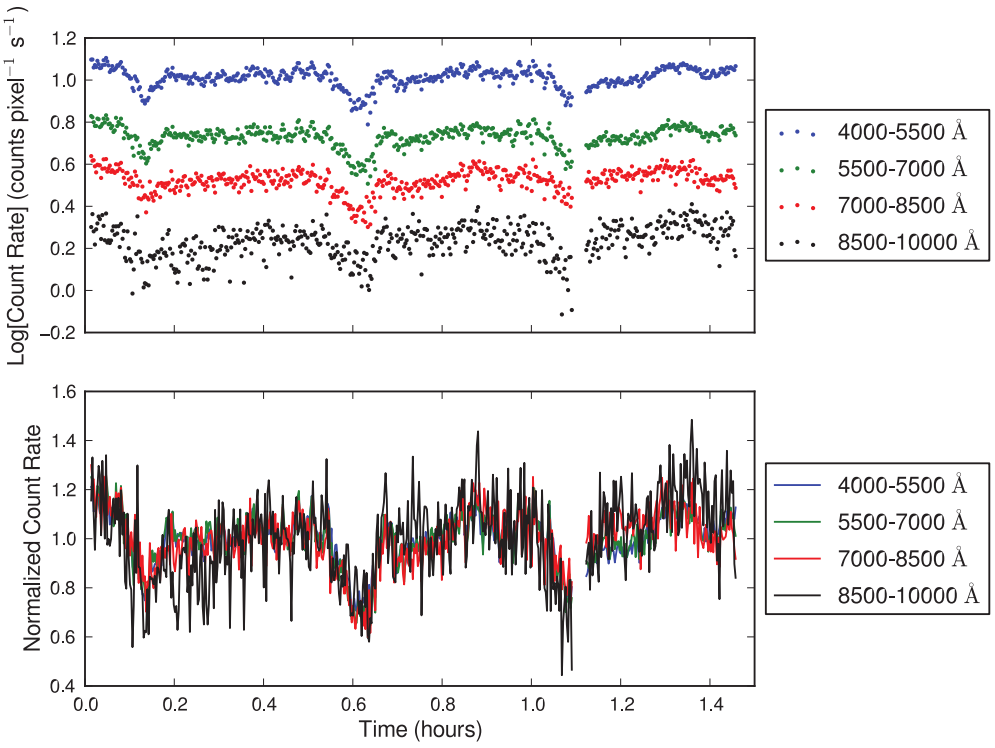

Figure 6.7: (Top) December 8 light curves in the blue (4000-5500 Å), green (5500-7000 Å), red (7000-8500 Å), and infrared (8500-10000 Å) bands, on a log scale. (Bottom) Light curves are scaled by the mean count rate in each band, in order to show the similarity in the four bands.

than the red (7000-8500 Å) and the infrared (8500-10000 Å) bands. Scaling by the mean in each band shows that the light curves were fairly consistent between different bands. There was little spectral variability observed during an eclipse.

6.3.5 Conclusions

The energy and timing information for individual photons obtainable with current MKIDs allowed us to explore the parameter space of SDSS J0926+3624 in exciting new ways. We were able to study the time variability of SDSS J0926+3624 at higher frequencies (up to 1,000 Hz) than had previously been done, and we showed that no QPOs

existed at these frequencies. With the energy information, we showed that there is little spectral variability throughout an orbit. Most importantly, we were able to use the eclipse timing information of our observations to further constrain the orbital period of the system, and we found a $\dot{P}$ of 3.07×10^{-13} at a 5.4 σ level, consistent with predictions for this system. Observations of SDSS J0926+3624 are planned with updated generations of MKID arrays over the next few years that will improve the SNR of both the aperture photometry and PSF fitting and improve the spectral variability analysis.

Acknowledgments

The MKID detectors used in this work were developed under NASA grant NNX11AD55G, and the readout was partially developed under NASA grant NNX10AF58G. S.R. Meeker was supported by a NASA Office of the Chief Technologist's Space Technology Research Fellowship, NASA grant NNX11AN29H. This work was partially supported by the Keck Institute for Space Studies. Fermilab is operated by Fermi Research Alliance, LLC under Contract No. De-AC02-07CH11359 with the United States Department of Energy. The authors would like to thank Shri Kulkarni, Director of the Caltech Optical Observatories for facilitating this project, as well as the excellent staff of the Palomar Observatory. This project also greatly benefitted from the support of Mike Werner, Paul Goldsmith, and Jonas Zmuidzinas at JPL.

6.4 Next Generation MKID Instrument Applications

The newest generation of optical MKID instrumentation focuses on a very different application in astronomy: the direct imaging of exoplanets. These instruments are the 10,000 pixel DARKNESS instrument at Palomar Observatory and the upcoming 20,440 pixel MEC instrument at the Subaru Telescope. Here, the MKID instrument is de-

signed to be put behind an adaptive optics (AO) system where it will integrate with a coronograph and be used as the imaging camera. The major limiting factor in directly imaging earth-like exoplanets is the contrast ratio between the reflected light of the planet and that of its host star. Currently, this is set by atmospheric speckles which vary on timescales of roughly a second.

The intermediate timescale of these speckles makes them difficult to deal with using traditional CCDs. They are too fast to subtract out in real time, but at the same time, they are too bright to simply integrate over. The single photon counting power of MKIDs presents a unique advantage here, allowing us to differentiate between these atmospheric speckles and a faint exoplanet. This would push the contrast ratio, making it easier to detect a faint companion should there be one.

There are also a couple of planned optical MKID instruments further down the line. The first of these is the Planetary Imaging Concept Testbed Using a Recoverable ExperimentCoronagraph (PICTURE-C [88]). The main science goals here are detecting protoplanetary disks. This already funded balloon instrument is scheduled to launch with MKIDs on-board in 2019. Even further down the line is the proposed Keck Radiometer Array using KID Energy Sensors (KRAKENS). This is expected to be more a general purpose MKID instrument with science goals similar to that of ARCONS, but with a much larger MKID array and telescope [89].

Chapter 7

Conclusions

MKIDs are a competitive low temperature detector technology capable of measuring photon energies from the far-infrared to the X-ray with high time resolution and moderate spectral resolution. These detectors have been advanced for over a decade, but there is still considerable room for improvement, potentially opening up entirely new science applications. Here, I briefly summarize my PhD work in advancing MKID technology and draw my conclusions on what I believe are the important matters for the future of this technology.

I opened my thesis with an introduction to the low temperature detector field and detailed the operation principles of MKIDs. Next, I described some fabrication techniques and new superconducting materials I used to attempt to improve MKIDs in a few key areas: detector yield, energy resolution, and quantum efficiency. The most important process to come out of this study was the development of the PtSi material system, which greatly exceeded the uniformity of the previously used TiN system while maintaining some of the more desirable qualities. This PtSi material system was adapted to the large-format MKID array fabrication process, and is being used in the next generation of DARKNESS and MEC arrays. Finally, I described some of the early astronomy projects

using MKID observations and what sorts of projects are envisioned in the future.

Below, I list what I consider are some of the most important points for MKID performance and future advances.

Energy Resolution - MKIDs generally have high enough Q_i that the energy resolution is now limited primarily by a combination of amplifier and TLS noise and positional dependance of the photon hit on the inductor. Replacing HEMT amplifiers with paramps seems to be the most likely path forward for reducing amplifier noise, but this work is still in its early stages. In order to reduce the other noise sources, a significant overhaul of the MKID geometry would most likely be required. One particular geometry that is being investigated and shows considerable promise for improving energy resolution is one in which a single square of inductance is connected to a pair large parallel plate capacitors, resembling a bow tie in appearance [67]. Another option would be to go to lower T_C superconductors, which would raise the theoretical energy resolution limit of MKIDs, assuming the cryogenics can operate at levels below 100 mK. The ongoing work on low T_C hafnium resonators is an important first step in this direction.

Pixel Yield - Compared to other low temperature detector technologies, MKIDs are the most natural to multiplex, and large arrays of over 20,000 pixels have been fabricated. Unfortunately, achieving high pixel yield is still one of the most critical challenges in optical MKID development. The PtSi material system, though a big improvement in uniformity over TiN, is likely not enough to get rid of frequency collisions. Most likely, an ex-post facto correction of the resonators, similar to the FIB milling method described above but much more controlled and efficient, will be required. One possible way of doing this would be using a lithographic writer to re-expose the photoresist in targeted areas of the capacitor and etching them away. Developing a software algorithm for calculating the frequency deviations and finding new locations for all resonators could also present a considerable challenge.

Quantum Efficiency - There has been very little work done toward improving the quantum efficiency of optical MKIDs in the past few years. Currently, the only thing being done to raise quantum efficiency is focus all the photons on the inductor portion of the array through the use of a microlens array. As the array size gets larger, however, these microlens arrays become difficult to align across an entire wafer. A more sophisticated microlens alignment tool will most likely be required to maximize quantum efficiency in future large arrays. Other methods, such as applying anti-reflection coatings to the surface of the inductors, need to be tested to determine whether a possible trade-off in energy resolution would be worth the increased quantum efficiency. More advanced techniques, such as using TKIDs with an absorbing material with close 100% absorption for optical photons (i.e., carbon nanotube forests), should also be developed, but this would require a major effort as TKIDs are still in a very early stage.

MKIDs for Optical Astronomy - Optical MKIDs are currently a bit of a niche detector in astronomy in that there are only a number of types of objects in which MKIDs provide a clear advantage over detectors traditionally used in optical astronomy, such as CCDs. At the moment, the direct imaging of exoplanets is one such application where there are few technologies able to compete with MKIDs. In the next few years, it will be exciting to see just how far MKIDs will be able to push down the contrast ratio limit and observe faint companions that were previously undetectable with other detectors. At the same time, as MKID performance continues to improve and telescopes continue to get larger, it is important to remember the numerous new MKID applications that may open up. For example, an optical counterpart in millisecond pulsars has yet to be observed, and the high time resolution and sensitivity to faint objects that MKIDs possess could make them the ideal detector to make such an observation.

Overall, MKIDs are a great tool for observational astronomy, among other applications. They are still somewhat far from maturity, and the potential for improvement

is still great. Compared to other low temperature detectors, MKIDs are fairly simple, but nonetheless come with an array of advantages such as high time resolution, moderate resolving power, and natural multiplexibility. It will be interesting to see just how far the technology advances and what new potential applications arise over the next few years.

Bibliography

[1] K. Irwin and G. Hilton, *Transition-Edge Sensors*, pp. 63–150. Springer, 2005.

[2] D. H. Andrews, W. F. Brucksch, Jr., W. T. Ziegler, and E. R. Blanchard, *Attenuated Superconductors I. For Measuring Infra-Red Radiation*, *Review of Scientific Instruments* **13** (1942) 281–292.

[3] K. D. Irwin, G. C. Hilton, D. A. Wollman, and J. M. Martinis, *X-ray detection using a superconducting transition-edge sensor microcalorimeter with electrothermal feedback*, *Applied Physics Letters* **69** (1996), no. 13 1945–1947.

[4] R. W. Ogburn IV, P. A. R. Ade, R. W. Aikin, M. Amiri, S. J. Benton, J. J. Bock, J. A. Bonetti, J. A. Brevik, B. Burger, C. D. Dowell, L. Duband, J. P. Filippini, S. R. Golwala, M. Halpern, M. Hasselfield, G. Hilton, V. V. Hristov, K. Irwin, J. P. Kaufman, B. G. Keating, J. M. Kovac, C. L. Kuo, A. E. Lange, E. M. Leitch, C. B. Netterfield, H. T. Nguyen, A. Orlando, C. L. Pryke, C. Reintsema, S. Richter, J. E. Ruhl, M. C. Runyan, C. D. Sheehy, Z. K. Staniszewski, S. A. Stokes, R. V. Sudiwala, G. P. Teply, J. E. Tolan, A. D. Turner, P. Wilson, and C. L. Wong, *The BICEP2 CMB polarization experiment*, *Proceedings of SPIE* **7741** (2010) 77411G–11.

[5] W. S. Holland, D. Bintley, E. L. Chapin, A. Chrysostomou, G. R. Davis, J. T. Dempsey, W. D. Duncan, M. Fich, P. Friberg, M. Halpern, K. D. Irwin, T. Jenness, B. D. Kelly, M. J. MacIntosh, E. I. Robson, D. Scott, P. A. R. Ade, E. Atad-Ettedgui, D. S. Berry, S. C. Craig, X. Gao, A. G. Gibb, G. C. Hilton, M. I. Hollister, J. B. Kycia, D. W. Lunney, H. McGregor, D. Montgomery, W. Parkes, R. P. J. Tilanus, J. N. Ullom, C. A. Walther, A. J. Walton, A. L. Woodcraft, M. Amiri, D. Atkinson, B. Burger, T. Chuter, I. M. Coulson, W. B. Doriese, C. Dunare, F. Economou, M. D. Niemack, H. A. L. Parsons, C. D. Reintsema, B. Sibthorpe, I. Smail, R. Sudiwala, and H. S. Thomas, *SCUBA-2: the 10000 pixel bolometer camera on the James Clerk Maxwell Telescope*, *Monthly Notices of the Royal Astronomical Society* **430** (2013), no. 4 2513.

[6] Z. Staniszewski, R. W. Aikin, M. Amiri, S. J. Benton, C. Bischoff, J. J. Bock, J. A. Bonetti, J. A. Brevik, B. Burger, C. D. Dowell, L. Duband, J. P. Filippini, S. R. Golwala, M. Halpern, M. Hasselfield, G. Hilton, V. V. Hristov, K. Irwin, J. M.

Kovac, C. L. Kuo, M. Lueker, T. Montroy, H. T. Nguyen, R. W. Ogburn, R. O'Brient, A. Orlando, C. Pryke, C. Reintsema, J. E. Ruhl, R. Schwarz, C. Sheehy, S. Stokes, K. L. Thompson, G. Teply, J. E. Tolan, A. D. Turner, A. G. Vieregg, P. Wilson, D. Wiebe, and C. L. Wong, *The Keck Array: A Multi Camera CMB Polarimeter at the South Pole*, *Journal of Low Temperature Physics* **167** (2012) 827–833.

[7] D. Barret, T. Lam Trong, J.-W. den Herder, L. Piro, X. Barcons, J. Huovelin, R. Kelley, J. M. Mas-Hesse, K. Mitsuda, S. Paltani, G. Rauw, A. Roanska, J. Wilms, M. Barbera, E. Bozzo, M. T. Ceballos, I. Charles, A. Decourchelle, R. den Hartog, J.-M. Duval, F. Fiore, F. Gatti, A. Goldwurm, B. Jackson, P. Jonker, C. Kilbourne, C. Macculi, M. Mendez, S. Molendi, P. Orleanski, F. Pajot, E. Pointecouteau, F. Porter, G. W. Pratt, D. Prle, L. Ravera, E. Renotte, J. Schaye, K. Shinozaki, L. Valenziano, J. Vink, N. Webb, N. Yamasaki, F. Delcelier-Douchin, M. Le Du, J.-M. Mesnager, A. Pradines, G. Branduardi-Raymont, M. Dadina, A. Finoguenov, Y. Fukazawa, A. Janiuk, J. Miller, Y. Naz, F. Nicastro, S. Sciortino, J. M. Torrejon, H. Geoffray, I. Hernandez, L. Luno, P. Peille, J. Andr, C. Daniel, C. Etcheverry, E. Gloaguen, J. Hassin, G. Hervet, I. Maussang, J. Moueza, A. Paillet, B. Vella, G. Campos Garrido, J.-C. Damery, C. Panem, J. Panh, S. Bandler, J.-M. Biffi, K. Boyce, A. Clnet, M. DiPirro, P. Jamotton, S. Lotti, D. Schwander, S. Smith, B.-J. van Leeuwen, H. van Weers, T. Brand, B. Cobo, T. Dauser, J. de Plaa, and E. Cucchetti, *The Athena X-ray Integral Field Unit (X-IFU)*, *Proceedings of SPIE* **9905** (2016) 99052F–41.

[8] J. Clarke and A. Braginski, *The SQUID Handbook: Fundamentals and Technology of SQUIDs and SQUID Systems*. Wiley, 2006.

[9] M. Kiviranta, H. Sepp, J. van der Kuur, and P. de Korte, *Squid-based readout schemes for microcalorimeter arrays*, *AIP Conference Proceedings* **605** (2002), no. 1 295–300.

[10] D. A. Bennett, R. D. Horansky, D. R. Schmidt, A. S. Hoover, R. Winkler, B. K. Alpert, J. A. Beall, W. B. Doriese, J. W. Fowler, C. P. Fitzgerald, G. C. Hilton, K. D. Irwin, V. Kotsubo, J. A. B. Mates, G. C. ONeil, M. W. Rabin, C. D. Reintsema, F. J. Schima, D. S. Swetz, L. R. Vale, and J. N. Ullom, *A high resolution gamma-ray spectrometer based on superconducting microcalorimeters*, *Review of Scientific Instruments* **83** (2012), no. 9 093113.

[11] A. Fleischmann, C. Enss, and G. Seidel, *Metallic Magnetic Calorimeters*, pp. 151–216. Springer, 2005.

[12] L. Fleischmann, M. Linck, A. Burck, C. Domesle, S. Kempf, M. Rodrigues, A. Pabinger, C. Pies, J.-P. Porst, H. Rotzinger, S. Schfer, R. Weldle,

A. Fleischmann, C. Enss, and G. M. Seidel, *Physics and applications of metallic magnetic calorimeters for particle detection*, *Journal of Physics: Conference Series* **150** (2009), no. 1 012013.

[13] A. Peacock, P. Verhoeve, N. Rando, A. Van Dordrecht, *et. al.*, *Single optical photon detection with a superconducting tunnel junction*, *Nature* **381** (1996), no. 6578 135.

[14] B. Josephson, *Possible new effects in superconductive tunnelling*, *Physics Letters* **1** (1962), no. 7 251 – 253.

[15] J. F. Schneiderman, P. Delsing, M. D. Shaw, H. M. Bozler, and P. M. Echternach, *Characterization of a differential radio-frequency single-electron transistor*, *Applied Physics Letters* **88** (2006), no. 8 083506.

[16] M. D. Shaw, J. Bueno, P. Day, C. M. Bradford, and P. M. Echternach, *Quantum capacitance detector: A pair-breaking radiation detector based on the single cooper-pair box*, *Physical Review B* **79** (2009) 144511.

[17] V. Bouchiat, D. Vion, P. Joyez, D. Esteve, and M. H. Devoret, *Quantum coherence with a single cooper pair*, *Physica Scripta* **1998** (1998), no. T76 165.

[18] P. M. Echternach, J. F. Schneiderman, M. D. Shaw, and P. Delsing, *Progress in the development of a single Cooper-pair box qubit*, *Quantum Information Processing* **8** (2009), no. 2 183–198.

[19] Y. Makhlin, G. Schön, and A. Shnirman, *Quantum-state engineering with josephson-junction devices*, *Review of Modern Physics* **73** (2001) 357–400.

[20] P. K. Day, H. G. Leduc, B. A. Mazin, A. Vayonakis, and J. Zmuidzinas, *A broadband superconducting detector suitable for use in large arrays*, *Nature* **425** (2003) 817–821.

[21] J. Zmuidzinas, *Superconducting microresonators: Physics and applications*, *Annual Review of Condensed Matter Physics* **3** (2012), no. 1 169–214.

[22] D. C. Mattis and J. Bardeen, *Theory of the anomalous skin effect in normal and superconducting metals*, *Phys. Rev.* **111** (Jul, 1958) 412–417.

[23] S. McHugh, B. A. Mazin, B. Serfass, S. Meeker, K. OBrien, R. Duan, R. Raffanti, and D. Werthimer, *A readout for large arrays of microwave kinetic inductance detectors*, *Review of Scientific Instruments* **83** (2012), no. 4.

[24] M. J. Strader, *Digital Readout for Microwave Kinetic Inductance Detectors and Applications in High Time Resolution Astronomy.* PhD thesis, University of California, Santa Barbara, 2016.

[25] J. Schlaerth, A. Vayonakis, P. Day, J. Glenn, J. Gao, S. Golwala, S. Kumar, H. LeDuc, B. Mazin, J. Vaillancourt, and J. Zmuidzinas, *A millimeter and submillimeter kinetic inductance detector camera*, *Journal of Low Temperature Physics* **151** (2008), no. 3 684–689.

[26] J. A. Schlaerth, N. G. Czakon, P. K. Day, T. P. Downes, R. Duan, J. Glenn, S. R. Golwala, M. I. Hollister, H. G. LeDuc, P. R. Maloney, B. A. Mazin, H. T. Nguyen, O. Noroozian, J. Sayers, S. Siegel, and J. Zmuidzinas, *The Status of Music: A Multicolor Sub/millimeter MKID Instrument*, *Journal of Low Temperature Physics* **167** (2012), no. 3 347–353.

[27] A. Parsons, D. Backer, C. Chang, D. Chapman, H. Chen, P. Crescini, C. de Jes us, C. Dick, P. Droz, D. MacMahon, K. Meder, J. Mock, V. Nagpal, B. Nikolic, A. Parsa, B. Richards, A. Siemion, J. Wawrzynek, D. Werthimer, and M. Wright, *Petaop/second fpga signal processing for SETI and radio astronomy*, *Asilomar Conference on Signals, Systems, and Computers* (2006).

[28] A. Monfardini, A. Benoit, A. Bideaud, L. Swenson, A. Cruciani, P. Camus, C. Hoffmann, F. X. Dsert, S. Doyle, P. Ade, P. Mauskopf, C. Tucker, M. Roesch, S. Leclercq, K. F. Schuster, A. Endo, A. Baryshev, J. J. A. Baselmans, L. Ferrari, S. J. C. Yates, O. Bourrion, J. Macias-Perez, C. Vescovi, M. Calvo, and C. Giordano, *A dual-band millimeter-wave kinetic inductance camera for the iram 30 m telescope*, *The Astrophysical Journal Supplement Series* **194** (2011), no. 2 24.

[29] M. Calvo, A. Benoît, A. Catalano, J. Goupy, A. Monfardini, N. Ponthieu, E. Barria, G. Bres, M. Grollier, G. Garde, J.-P. Leggeri, G. Pont, S. Triqueneaux, R. Adam, O. Bourrion, J.-F. Macías-Pérez, M. Rebolo, A. Ritacco, J.-P. Scordilis, D. Tourres, A. Adane, G. Coiffard, S. Leclercq, F.-X. Désert, S. Doyle, P. Mauskopf, C. Tucker, P. Ade, P. André, A. Beelen, B. Belier, A. Bideaud, N. Billot, B. Comis, A. D'Addabbo, C. Kramer, J. Martino, F. Mayet, F. Pajot, E. Pascale, L. Perotto, V. Revéret, L. Rodriguez, G. Savini, K. Schuster, A. Sievers, and R. Zylka, *The NIKA2 Instrument, A Dual-Band Kilopixel KID Array for Millimetric Astronomy*, *Journal of Low Temperature Physics* **184** (2016) 816–823.

[30] A. Endo, J. J. A. Baselmans, P. P. van der Werf, B. Knoors, S. M. H. Javadzadeh, S. J. C. Yates, D. J. Thoen, L. Ferrari, A. M. Baryshev, Y. J. Y. Lankwarden, P. J. de Visser, R. M. J. Janssen, and T. M. Klapwijk, *Development of DESHIMA: a redshift machine based on a superconducting on-chip filterbank*, *Proceedings of SPIE* **8452** (2012) 84520X–15.

[31] S. Hailey-Dunsheath, E. Shirokoff, P. S. Barry, C. M. Bradford, G. Chattopadhyay, P. Day, S. Doyle, M. Hollister, A. Kovacs, H. G. LeDuc, P. Mauskopf, C. M. McKenney, R. Monroe, R. O'Brient, S. Padin, T. Reck, L. Swenson, C. E. Tucker, and J. Zmuidzinas, *Status of SuperSpec: a broadband, on-chip millimeter-wave spectrometer*, *Proceedings of SPIE* **9153** (2014) 91530M–16.

[32] G. Cataldo, W.-T. Hseih, W.-C. Huang, S. H. Moseley, T. R. Stevenson, and E. J. Wollack, *Micro-Spec: an integrated direct-detection spectrometer for far-infrared space telescopes*, *Proceedings of SPIE* **9143** (2014) 91432C–9.

[33] C. M. Bradford, M. Kenyon, W. Holmes, J. Bock, and T. Koch, *Sensitive far-IR survey spectroscopy: BLISS for SPICA*, *Proceedings of SPIE* **7020** (2008) 70201O–12.

[34] T. Matsumoto, *Large aperture cool telescope mission: SPICA*, *Proceedings of SPIE* **4850** (2003) 1091–1096.

[35] B. A. Mazin, S. R. Meeker, M. J. Strader, P. Szypryt, D. Marsden, J. C. v. Eyken, G. E. Duggan, A. B. Walter, G. Ulbricht, M. Johnson, B. Bumble, K. OBrien, and C. Stoughton, *ARCONS: A 2024 pixel optical through near-IR cryogenic imaging spectrophotometer*, *Publications of the Astronomical Society of the Pacific* **125** (2013), no. 933 pp. 1348–1361.

[36] H. G. Leduc, B. Bumble, P. K. Day, B. H. Eom, J. Gao, S. Golwala, B. A. Mazin, S. McHugh, A. Merrill, D. C. Moore, O. Noroozian, A. D. Turner, and J. Zmuidzinas, *Titanium nitride films for ultrasensitive microresonator detectors*, *Applied Physics Letters* **97** (2010), no. 10.

[37] M. J. Strader, M. D. Johnson, B. A. Mazin, G. V. S. Jaeger, C. R. Gwinn, S. R. Meeker, P. Szypryt, J. C. van Eyken, D. Marsden, K. O'Brien, A. B. Walter, G. Ulbricht, C. Stoughton, and B. Bumble, *Excess optical enhancement observed with ARCONS for early Crab giant pulses*, *The Astrophysical Journal Letters* **779** (2013) L12.

[38] M. J. Strader, A. M. Archibald, S. R. Meeker, P. Szypryt, A. B. Walter, J. C. van Eyken, G. Ulbricht, C. Stoughton, B. Bumble, D. L. Kaplan, and B. A. Mazin, *Search for optical pulsations in PSR J0337+1715*, *Monthly Notices of the Royal Astronomical Society* **459** (June, 2016) 427–430.

[39] P. Szypryt, G. E. Duggan, B. A. Mazin, S. R. Meeker, M. J. Strader, J. C. van Eyken, D. Marsden, K. O'Brien, A. B. Walter, G. Ulbricht, T. A. Prince, C. Stoughton, and B. Bumble, *Direct detection of SDSS J0926+3624 orbital expansion with ARCONS*, *Monthly Notices of the Royal Astronomical Society* **439** (2014), no. 3 pp. 2765–2770.

[40] S. R. Meeker, B. A. Mazin, R. Jensen-Clem, A. B. Walter, P. Szypryt, M. J. Strader, and C. Bockstiegel, *Design and development status of mkid integral field spectrographs for high contrast imaging*, *Adaptive Optics for Extremely Large Telescopes 4 - Conference Proceedings* (2015).

[41] G. Ulbricht, B. Mazin, P. Szypryt, A. Walter, C. Bockstiegel, and B. Bumble, *Highly multiplexible thermal kinetic inductance detectors for x-ray imaging spectroscopy*, *Applied Physics Letters* **106** (2015), no. 25.

[42] P. Drude, *Zur Elektronentheorie der Metalle*, *Annalen der Physik* **306** (1900), no. 3 566–613.

[43] P. Drude, *Zur Elektronentheorie der Metalle; II. Teil. Galvanomagnetische und thermomagnetische Effecte*, *Annalen der Physik* **308** (1900), no. 11 369–402.

[44] B. A. Mazin, *Microwave Kinetic Inductance Detectors*. PhD thesis, California Institute of Technology, 2004.

[45] A. G. Kozorezov, A. F. Volkov, J. K. Wigmore, A. Peacock, A. Poelaert, and R. den Hartog, *Quasiparticle-phonon downconversion in nonequilibrium superconductors*, *Physical Review B* **61** (2000) 11807–11819.

[46] J. Gao, *The Physics of Superconducting Microwave Resonators*. PhD thesis, California Institute of Technology, 2008.

[47] P. Szypryt, B. A. Mazin, G. Ulbricht, B. Bumble, S. R. Meeker, C. Bockstiegel, and A. B. Walter, *High quality factor platinum silicide microwave kinetic inductance detectors*, *Applied Physics Letters* **109** (2016) 151102.

[48] B. A. Mazin, B. Bumble, S. R. Meeker, K. O'Brien, S. McHugh, and E. Langman, *A superconducting focal plane array for ultraviolet, optical, and near-infrared astrophysics*, *Optics Express* **20** (2012) 1503.

[49] M. R. Vissers, J. Gao, M. Sandberg, S. M. Duff, D. S. Wisbey, K. D. Irwin, and D. P. Pappas, *Proximity-coupled Ti/TiN multilayers for use in kinetic inductance detectors*, *Applied Physics Letters* **102** (2013), no. 23 232603.

[50] H. Meissner, *Superconductivity of contacts with interposed barriers*, *Physical Review* **117** (1960) 672–680.

[51] J. van Eyken, M. Strader, A. Walter, S. Meeker, P. Szypryt, C. Stoughton, K. OBrien, D. Marsden, N. Rice, Y. Lin, and B. Mazin, *The ARCONS pipeline: Data reduction for MKID arrays*, *The Astrophysical Journal Supplement Series* **219** (2015) pp. 14.

[52] S. R. Golwala, *Exclusion Limits on the WIMP-Nucleon Elastic-Scattering Cross Section from the Cryogenic Dark Matter Search*. PhD thesis, University of California, Berkeley, 2000.

[53] J. Gao, M. Daal, A. Vayonakis, S. Kumar, J. Zmuidzinas, B. Sadoulet, B. A. Mazin, P. K. Day, and H. G. Leduc, *Experimental evidence for a surface distribution of two-level systems in superconducting lithographed microwave resonators*, *Applied Physics Letters* **92** (2008), no. 15 152505.

[54] A. Megrant, C. Neill, R. Barends, B. Chiaro, Y. Chen, L. Feigl, J. Kelly, E. Lucero, M. Mariantoni, P. J. J. O'Malley, D. Sank, A. Vainsencher, J. Wenner, T. C. White, Y. Yin, J. Zhao, C. J. Palmstrøm, J. M. Martinis, and A. N. Cleland, *Planar superconducting resonators with internal quality factors above one million*, *Appl. Phys. Lett.* **100** (2012), no. 11 113510.

[55] Low Noise Factory, *4-8 GHz Cryogenic Low Noise Amplifier, LNF-LNC4_8C datasheet*, 2017.

[56] B. H. Eom, P. K. Day, H. G. Leduc, and J. Zmuidzinas, *A Wideband, Low-Noise Superconducting Amplifier with High Dynamic Range*, *Nature Physics* **8** (2012) 623–627.

[57] A. E. Lita, B. Calkins, L. A. Pellochoud, A. J. Miller, and S. Nam, *High-efficiency photon-number-resolving detectors based on hafnium transition-edge sensors*, *AIP Conference Proceedings* **1185** (2009), no. 1 351–354.

[58] P. Coumou, M. Zuiddam, E. Driessen, P. de Visser, J. Baselmans, and T. Klapwijk, *Microwave properties of superconducting atomic-layer deposited tin films*, *IEEE Transactions on Applied Superconductivity* **23** (2013), no. 3 7500404.

[59] K. Oto, S. Takaoka, K. Murase, and S. Ishida, *Superconductivity in PtSi ultrathin films*, *Journal of Applied Physics* **76** (1994) pp. 5339–5342.

[60] H. Bentmann, A. A. Demkov, R. Gregory, and S. Zollner, *Electronic, optical, and surface properties of PtSi thin films*, *Physical Review B* **78** (Nov, 2008) 205302.

[61] Y. Takahashi, H. Ishii, and J. Murota, *New platinum silicide formation method using reaction between platinum and silane*, *Journal of Applied Physics* **58** (1985), no. 8 3190–3194.

[62] J. Goupy, A. Adane, A. Benoit, O. Bourrion, M. Calvo, A. Catalano, G. Coiffard, C. Hoarau, S. Leclercq, H. Le Sueur, J. Macias-Perez, A. Monfardini, I. Peck, and K. Schuster, *Microfabrication technology for large lekid arrays: From nika2 to future applications*, *Journal of Low Temperature Physics* **184** (2016) 661–667.

[63] P. Szypryt, B. Mazin, B. Bumble, H. Leduc, and L. Baker, *Ultraviolet, optical, and near-IR microwave kinetic inductance detector materials developments*, *IEEE Transactions on Applied Superconductivity* **25** (2015), no. 3 pp. 1–4.

[64] O. Noroozian, *Superconducting Microwave Resonator Arrays for Submillimeter/Far-Infrared Imaging*. PhD thesis, California Institute of Technology, 2012.

[65] B. Sacépé, C. Chapelier, T. I. Baturina, V. M. Vinokur, M. R. Baklanov, and M. Sanquer, *Disorder-induced inhomogeneities of the superconducting state close to the superconductor-insulator transition*, *Physical Review Letters* **101** (2008) 157006.

[66] A. D. O'Connell, M. Ansmann, R. C. Bialczak, M. Hofheinz, N. Katz, E. Lucero, C. McKenney, M. Neeley, H. Wang, E. M. Weig, A. N. Cleland, and J. M. Martinis, *Microwave dielectric loss at single photon energies and millikelvin temperatures*, *Applied Physics Letters* **92** (2008), no. 11 112903.

[67] G. Coiffard, B. A. Mazin, M. Daal, P. Szypryt, G. Ulbricht, and N. Zobrist, *Parallel plate microwave kinetic inductance detectors*, *Applied Physics Letters, submitted* (2017). Submitted.

[68] B. Warner, *The AM Canum Venaticorum Stars*, *Astrophysics and Space Science* **225** (1995) 249–270.

[69] G. Nelemans, *AM CVn stars*, in *The Astrophysics of Cataclysmic Variables and Related Objects* (J.-M. Hameury and J.-P. Lasota, eds.), vol. 330 of *Astronomical Society of the Pacific Conference Series*, p. 27, 2005.

[70] G. Ramsay, C. Brocksopp, P. J. Groot, P. Hakala, H. Lehto, T. R. Marsh, R. Napiwotzki, G. Nelemans, S. Potter, B. Slee, D. Steeghs, and K. Wu, *Recent Observational Progress in AM CVn Binaries*, in *15th European Workshop on White Dwarfs* (R. Napiwotzki and M. R. Burleigh, eds.), vol. 372 of *Astronomical Society of the Pacific Conference Series*, p. 425, 2007.

[71] J. E. Solheim, *AM CVn Stars: Status and Challenges*, *Publications of the Astronomical Society of the Pacific* **122** (2010) 1133–1163.

[72] R. P. Kraft, J. Mathews, and J. L. Greenstein, *Binary Stars among Cataclysmic Variables. II. Nova WZ Sagittae: a Possible Radiator of Gravitational Waves.*, *The Astrophysical Journal* **136** (1962) 312–315.

[73] G. Nelemans, L. R. Yungelson, and S. F. Portegies Zwart, *Short-period am cvn systems as optical, x-ray and gravitational-wave sources*, *Monthly Notices of the Royal Astronomical Socieity* **349** (2004), no. 1 181–192.

[74] B. Paczyński, *Gravitational Waves and the Evolution of Close Binaries*, *Acta Astronomica* **17** (1967) 287.

[75] I. Iben, Jr. and A. V. Tutukov, *Helium star cataclysmics*, *The Astrophysical Journal* **370** (Apr., 1991) 615–629.

[76] P. Podsiadlowski, Z. Han, and S. Rappaport, *Cataclysmic variables with evolved secondaries and the progenitors of am cvn stars*, *Monthly Notices of the Royal Astronomical Society* **340** (2003), no. 4 1214–1228.

[77] K. G. Malmquist, *Investigations on the stars in high galactic latitudes II. Photographic magnitudes and colour indices of about 4500 stars near the north galactic pole.*, *Stockholms Observatoriums Annaler* **12** (1936) 7.

[78] J. Smak, *Light variability of HZ 29*, *Acta Astronomica* **17** (1967) 255.

[79] D. B. Levitan, *Finding needles in the haystack : a search for AM CVn systems using the Palomar Transient Factory.* PhD thesis, California Institute of Technology, May, 2013.

[80] S. F. Anderson, D. Haggard, L. Homer, N. R. Joshi, B. Margon, N. M. Silvestri, P. Szkody, M. A. Wolfe, E. Agol, A. C. Becker, A. Henden, P. B. Hall, G. R. Knapp, M. W. Richmond, D. P. Schneider, G. Stinson, J. C. Barentine, H. J. Brewington, J. Brinkmann, M. Harvanek, S. J. Kleinman, J. Krzesinski, D. Long, E. H. Neilsen, Jr., A. Nitta, and S. A. Snedden, *Ultracompact AM Canum Venaticorum Binaries from the Sloan Digital Sky Survey: Three Candidates Plus the First Confirmed Eclipsing System*, *The Astronomical Journal* **130** (2005) 2230–2236.

[81] R. Whitehurst, *Numerical simulations of accretion disks. I - Superhumps - A tidal phenomenon of accretion disks*, *Monthly Notices of the Royal Astronomical Society* **232** (1988) 35–51.

[82] B. A. Mazin, K. O'Brien, S. McHugh, B. Bumble, D. Moore, S. Golwala, and J. Zmuidzinas, *ARCONS: a highly multiplexed superconducting optical to near-IR camera*, in *Proceedings of SPIE*, vol. 7735, 2010.

[83] T. R. Marsh, V. S. Dhillon, S. P. Littlefair, P. J. Groot, P. Hakala, G. Nelemans, G. Ramsay, G. H. A. Roelofs, and D. Steeghs, *SDSS J0926+3624, the First Eclipsing AM CVn Star, as Seen with ULTRACAM*, in *15th European Workshop on White Dwarfs* (R. Napiwotzki and M. R. Burleigh, eds.), vol. 372 of *Astronomical Society of the Pacific Conference Series*, p. 431, 2007.

[84] C. M. Copperwheat, T. R. Marsh, S. P. Littlefair, V. S. Dhillon, G. Ramsay, A. J. Drake, B. T. Gänsicke, P. J. Groot, P. Hakala, D. Koester, G. Nelemans, G. Roelofs, J. Southworth, D. Steeghs, and S. Tulloch, *SDSS J0926+3624: the shortest period eclipsing binary star*, *Monthly Notices of the Royal Astronomical Society* **410** (2011) 1113–1129.

[85] B. Warner and P. A. Woudt, *QPOs in CVs: An executive summary*, in *American Institute of Physics Conference Series*, vol. 1054, pp. 101–110, 2008.

[86] R. F. Stellingwerf, *Period determination using phase dispersion minimization*, *The Astrophysical Journal* **224** (1978) 953–960.

[87] J. Diaz-Cordoves and A. Gimenez, *A new nonlinear approximation to the limb-darkening of hot stars*, *Astronomy and Astrophysics* **259** (1992) 227–231.

[88] T. Cook, K. Cahoy, S. Chakrabarti, E. Douglas, S. C. Finn, M. Kuchner, N. Lewis, A. Marinan, J. Martel, D. Mawet, B. Mazin, S. R. Meeker, C. Mendillo, G. Serabyn, D. Stuchlik, and M. Swain, *Planetary imaging concept testbed using a recoverable experimentcoronagraph (picture c)*, *Journal of Astronomical Telescopes, Instruments, and Systems* **1** (2015), no. 4 044001.

[89] B. A. Mazin, G. Becker, K. France, W. Fraser, D. A. Howell, T. Jones, S. Meeker, K. O'Brien, J. X. Prochaska, B. Siana, M. Strader, P. Szypryt, S. P. Tendulkar, T. Treu, and G. Vasisht, *Science with KRAKENS*, *ArXiv e-prints* (2015) [arXiv:1506.0345].